

# **A study of complex magnetic configurations using Magnetic Force Microscopy**

by

**Eider Berganza Eguiarte**

**Doctoral thesis**

submitted to **Universidad Autónoma de Madrid** in partial fulfillment of the requirements for the degree of

**Doctor in Philosophy**

**Supervised by:**

**Dr. Agustina Asenjo Barahona**

**Dr. Miriam Jaafar Ruiz-Castellanos**

**Tutored by:**

**Prof. Julio Gómez Herrero**



## ABSTRACT

The irruption of nanomagnetism in industry has brought remarkable advances in data storage technologies. In addition, further development in this field is expected to revolutionize traditional medicine by addressing diagnosis and disease treatment from a localized approach. Applications require a deep fundamental knowledge on the magnetic behavior of nanostructures. This thesis is framed on the study of non-trivial magnetic configurations and magnetization reversal processes of different nano-objects.

The magnetic configuration and magnetization reversal process of cylindrical shaped magnets (nanowires and nanodots) have been studied using Magnetic Force Microscopy. Different mechanisms have been studied to obtain well-defined pinning sites in nanowires with axial magnetization. The magnetization reversal process of nanowires of complex magnetic configuration, due to strong magnetocrystalline anisotropy, has been studied. Finally, results obtained in cylindrical nanodots are presented, where topologically protected spin textures have been unveiled.

## CONTENTS

Description of the thesis.....	v
Descripción de la tesis.....	vii
<b>CHAPTER 1: Introduction to nanomagnetism.....</b>	<b>1</b>
<b>1. Nanoscience.....</b>	<b>3</b>
<b>2. Nanomagnetism.....</b>	<b>4</b>
2.1 Micromagnetic theory.....	5
2.2 Energy balance.....	6
2.3 Magnetic domains and domain walls.....	9
2.4 Magnetization reversal.....	17
2.5 Domain imaging techniques.....	20
<b>3. References.....</b>	<b>25</b>
<b>CHAPTER 2: Magnetic Force Microscopy.....</b>	<b>31</b>
<b>1. Scanning Probe Microscopy.....</b>	<b>32</b>
1.1. Fundamentals.....	33
1.2. Dynamic mode.....	35
<b>2. Magnetic Force Microscopy.....</b>	<b>39</b>
2.1. Variable Field MFM.....	41
2.2. 3D modes.....	42
2.3. Combination of MFM with Kelvin Probe Force Microscopy.....	43
<b>3. Tip engineering.....</b>	<b>44</b>
3.1. Low moment tips coated by sputtering.....	46
3.2. Tips for liquid environments.....	48
3.3. Enhanced sensitivity tips.....	53
3.4. Alternatives to sputtering: Using magnetic nanowires as probes.....	54
<b>4. Conclusions.....</b>	<b>60</b>
<b>5. References.....</b>	<b>62</b>
<b>APPENDIX A: Micromagnetic simulations, a complementary tool for the interpretation of MFM images.....</b>	<b>67</b>

**CHAPTER 3: Domain wall pinning in magnetic nanowires.....73**

- 1. Sample preparation.....76**
  - 1.1. Fabrication of nanowires through electrodeposition.....76
  - 1.2. Approaches to control the Domain Wall pinning.....77
- 2. Bamboo-like nanowires.....78**
  - 2.1. Effect of the modulation on the spin configuration.....79
  - 2.2. Vortex mediated magnetization reversal.....81
  - 2.3. Domain Wall pinning.....86
- 3. Diameter modulated nanowires.....89**
- 4. FeCo nanowires with non-magnetic defects spacers.....92**
  - 4.1. Correlation between topography and magnetization.....93
  - 4.2. Magnetization reversal.....94
- 5. Conclusion.....99**
- 6. References.....101**

**CHAPTER 4: Complex domain configuration in magnetic nanowires.....105**

- 1. Geometrically modulated Co NWs.....108**
- 2. CoNi NWs: Choosing the magnetization axis.....113**
- 3. Multisegmented nanowires: CoNi-Ni.....114**
  - 3.1. Crystallographic structure of CoNi segments.....115
  - 3.2. Single and multivortex domain configurations. ....116
  - 3.3. Micromagnetic simulations.....120
  - 3.4. Study of domain configuration and coupling between segments under in-situ applied field.....126
- 4. Conclusions.....131**
- 5. References.....133**

**APPENDIX B: Protocol for nanowire deposition onto substrates for their individual study.....139**

<b>APPENDIX C: Preparation of nanowires for magnetoresistance measurements .....</b>	<b>145</b>
--	------------

<b>CHAPTER 5: Magnetic soft particles: From vortices to skyrmions.....</b>	<b>151</b>
--	------------

1. Magnetic nanoparticles.....	153
2. Fabrication through Hole-mask Colloidal Lithography and morphological characterization.....	154
3. Study of the magnetic configuration.....	156
4. Response to magnetic in-plane field.....	159
5. Phase diagram of skyrmions.....	163
5.1. Further investigation on the effect of the size.....	167
6. Conclusions.....	174
7. References.....	177

General conclusions.....	181
--------------------------	-----

Conclusiones generales.....	183
-----------------------------	-----

List of publications.....	185
---------------------------	-----

## Description of the thesis

The irruption of nanomagnetism in industry has brought remarkable advances in data storage technologies. In addition, further development in this field is expected to revolutionize traditional medicine by addressing diagnosis and disease treatment from a localized approach.

Applications require a deep fundamental knowledge on the magnetic behavior of the nanostructures. This thesis is framed on the study of non-trivial magnetic configurations and magnetization reversal processes of different nanoobjects. The studied have been carried out using Magnetic Force Microscopy (MFM) to analyze their magnetic configurations in remanence and under in-situ field. The thesis is divided into 5 different chapters.

Chapter 1 is a brief introduction to nanomagnetism; it gives a general background explaining some of the key concepts necessary to understand the contents of this thesis. The basis of the micromagnetic theory is introduced to go on to the domain wall (DW) formation and magnetization reversal process. Finally, a brief explanation of the different available imaging techniques is given, leaving the door open to the second chapter.

Chapter 2 begins with an introduction to the fundamentals of Atomic Force Microscopy (AFM) and MFM. In this chapter, the contributions made to the technique throughout this thesis are addressed. All of them are based on the adjustments made on the tip, which is the most critical element of the microscope, to meet different requirements: minimization of the tip stray field influence over the sample configuration, improvement of the signal-to-noise ratio to obtain better quality images in liquid media and the exploration of alternative methods to the traditional coating by sputtering deposition to improve the stray field control and resolution.

Chapter 3 focuses on the control of the magnetization reversal process of uniaxially magnetized nanowires (NW). The consecution of cylindrical nanowires with well-defined pinning sites is of outermost importance for DW based data storage devices. Three different types of diameter modulation are explored with the aim of studying the effect they produce on the magnetization reversal and determine the most efficient mechanism to pin domain walls.

Chapter 4 deals with cylindrical nanowires with strong magnetocrystalline anisotropy, which results in complex vortex-like magnetic configurations as a result of the interplay of shape and magnetocrystalline anisotropies. The influence of diameter modulation on Co based nanowires is studied. Then, NWs based on CoNi alloy are imaged to understand the influence of the stoichiometry in this commonly used alloy. The final and most extended part describes the magnetization reversal of multisegmented nanowires of two materials with different magnetic properties.

In Chapter 5, the most innovative results are presented. The detection of hedgehog skyrmions in permalloy nanodots (nanowires of short length) represents a major breakthrough due to the absence of perpendicular magnetic anisotropy or Dzyaloshinski-Moriya interaction in the system. The behavior of nanodots of diameter below and beyond 100nm are studied under applied field is studied and modeled. In bigger nanodots vortex configurations are present, while smaller nanodots present skyrmions.

## Descripción de la tesis

La irrupción del nanomagnetismo en la industria ha producido avances significativos en la tecnología de almacenamiento de datos. Se espera, además, que los futuros avances en este campo revolucionen la medicina tradicional, enfocando el diagnóstico y tratamiento de enfermedades desde una forma mucho más localizada.

Llevar a cabo cualquier aplicación requiere profundizar en el conocimiento del comportamiento magnético de las nanoestructuras. Esta tesis está enmarcada en el estudio de configuraciones magnéticas no triviales y los procesos de inversión de la imanación de distintos nanoobjetos. La investigación se ha realizado utilizando la Microscopía de Fuerzas Magnéticas (MFM) bajo la aplicación de campo in-situ. Esta tesis está dividida en 5 capítulos.

El Capítulo 1 consiste en una breve introducción al nanomagnetismo; pone en contexto el tema de estudio de la tesis, exponiendo algunos conceptos clave para la comprensión de sus contenidos. Se introduce la base de la teoría del micromagnetismo, para llegar a la formación de paredes de dominio y procesos de inversión de la imanación. Finalmente, se presenta una breve explicación de las distintas técnicas de imagen disponibles, enlazando así con el segundo capítulo.

El Capítulo 2 comienza con una introducción a los fundamentos de la Microscopía de Fuerzas Atómicas (AFM) y MFM. A continuación, se exponen las contribuciones realizadas a lo largo de la tesis a esta técnica. Todas ellas consisten en adecuaciones de la punta, el elemento más crítico del microscopio, para cumplir requisitos específicos de cada medida: minimizar la influencia del campo de fugas de la punta sobre la configuración magnética de la muestra, mejorar de la relación señal-ruido para la obtención de imágenes de mayor calidad en medio líquido y el estudio de métodos alternativos al sputtering para mejorar el control sobre el campo de fugas de la muestra y la resolución lateral.

El Capítulo 3 está dedicado al estudio de mecanismos de control de procesos de inversión de la imanación en nanohilos con imanación en el eje. La obtención de nanohilos cilíndricos con puntos de anclaje bien definidos es de vital importancia para el desarrollo de dispositivos de almacenamiento de



datos basados en el control de paredes de dominio. Se han explorado tres mecanismos de anclaje y se ha estudiado su efecto real en el proceso de inversión de la imanación para terminar concluyendo cuál de los tres es el más eficiente en el anclaje de paredes.

El Capítulo 4 trata sobre nanohilos cilíndricos con fuerte anisotropía magnetocristalina. Como resultado de la acción conjunta de los términos de energía (relativos a las anisotropías de forma y magnetocristalina), la configuración magnética resultante es un conjunto de vórtices. Se estudia la influencia de la modulación en diámetro sobre hilos basados en cobalto. Posteriormente, se estudian hilos basados en la aleación cobalto-niquel, para determinar la influencia de la estequiometría en la configuración de dominios. En la última parte –y más extensa- se describe el proceso de inversión de la imanación de hilos multisegmentados que combinan materiales con distintas propiedades magnéticas.

En el capítulo 5 se presentan los resultados más innovadores de esta tesis. La detección de skyrmions tipo Néel (erizo) en nanodiscos de permalloy (nanohilos de longitud reducida) constituye un descubrimiento relevante, debido a la ausencia de anisotropía perpendicular o interacción Dzyaloshinski-Moriya en el sistema. Se comparan los comportamientos bajo campo magnético de nanodiscos de diámetro menor de 100nm, con los de nanodiscos de diámetro mayor de 100nm. Se verifica que los más pequeños presentan configuración de skyrmion, mientras los grandes presentan configuración vórtice.

# **CHAPTER 1:**

# **Introduction to nanomagnetism**

This chapter is a brief introduction to the basic concepts of nanomagnetism, necessary to understand the contents and results of this thesis. The importance of nanoscience and of nanomagnetism in particular are highlighted, followed by the account of the most relevant achievements and promising applications in this field. General concepts of the theory of micromagnetism are exposed, paying special attention to the magnetic domain formation and the field driven magnetization reversal, which are central elements in this manuscript. Finally, domain imaging techniques, which are essential tools in nanomagnetism to study the domain formation, are compared amongst them. This topic sets the grounds for the next chapter, which deepens into one of the mentioned techniques: magnetic force microscopy.

## 1. Nanoscience

In 1959, Richard Feynman claimed that there was no physical limitation to explore a world that was invisible to the human eye and inaccessible at that time due to lack of technical development.<sup>1</sup> In his widely popular lecture “*there is plenty of room at the bottom*”, he invited physicist all over the world to address efforts to develop the field of nanoscience. Almost 60 years later, nanotechnology has revolutionized the industry and the general audience possesses basic notions about nanoscience.

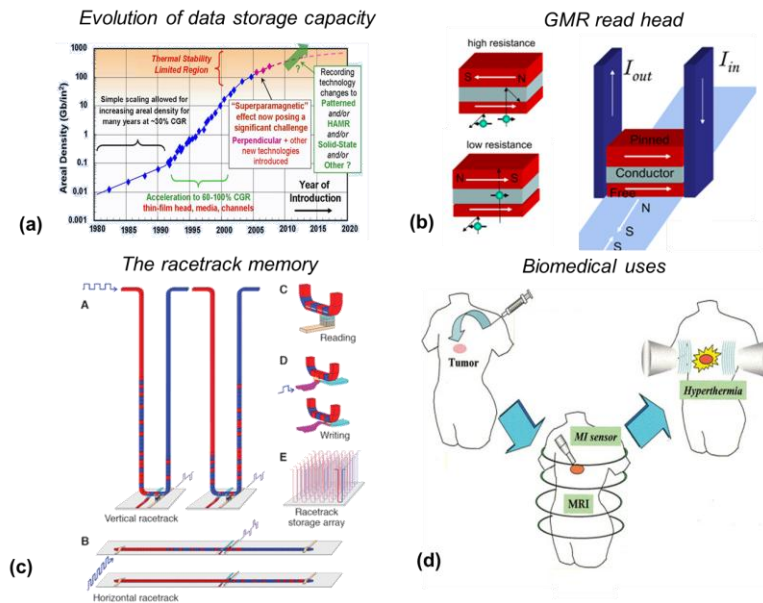
Nanoscience is the discipline that studies different types of phenomena that occur at the nanoscale, a length scale 9 orders of magnitude below the meter. The interest in the development of this science is twofold: from the fundamental viewpoint, matter behaves very differently to bulk when at least one of the dimensions is reduced to the nanoscale. The large amount of surface atoms, compared to bulk counterparts leads to intriguing consequences. Dominant forces acting on this length scale differ significantly from those in bulk. On the other hand, nanostructures possess very attractive features regarding applications. The reduction of the dimensionality for *in-vivo* applications, as in nanomedicine, or the optimization of low energy consumption devices constitute examples of new possibilities offered by nanomaterials. The so-called graphene –whose synthesis was awarded with a novel prize in Physics in 2010 – is a paradigmatic example of the importance of nanoscience from the fundamental and practical perspectives. Rapid progress in this field was made possible due to the development of new fabrications methods together with novel characterization techniques.

Multidisciplinarity is one of the main assets of nanoscience. Nanotechnological advances are pursued in very diverse fields, such as chemistry, biology, medicine, etc. Within physics, nanomagnetism constitutes one of the most relevant fields where specific advances have led to considerable progress in industry, particularly in the field of information technologies.

## 2. Nanomagnetism

Although magnetism was discovered in the ancient world, when people noticed that lodestones –magnetite- had the capability to attract iron, it was not until the development of quantum physics that the origin of ferromagnetism was well understood. One step further, the study of magnetic nanostructures has led to the finding of different behavior than what is observed in bulk. In this context, we consider nanomagnetism to be the area of research in physics, dealing with the magnetic properties of objects that have at least one dimension in the nanoscopic range –between 1 and 100nm-. As in other fields of condensed matter physics, in nanomagnetism, the characteristic lengths of the studied objects as domain size, exchange length, superparamagnetic critical diameter, etc., are comparable with the sample dimensions. This fact, together with the break of translation symmetry, originates behaviors that differ from those in bulk.

Nanomagnetism has many practical applications,<sup>2,3</sup> the most prominent ones being magnetic data storage and Giant Magnetoresistance read-out heads. Currently, the field of spintronics, which deals with the exploitation of spin properties instead of –or in addition to- electric charge, is working to meet the worldwide exponential growth of data storage necessities (Figure 1.1a). So far, the most relevant breakthrough in spintronics came from Albert Fert<sup>4</sup> and Peter Grünberg,<sup>5</sup> who independently found the Giant Magnetoresistance (GMR) effect and were later awarded the Nobel Prize in Physics (2007). This effect observed in alternating ferromagnetic and non-magnetic multilayers where the electrical resistance varies depending on the magnetization alignment, is currently used to read data in hard disk drives and sensors (Figure 1.1b). Another turning point in spintronics was reached when scientists from IBM came up with the concept of the racetrack memory.<sup>6,7</sup> Along the last decades, the data storage density had increased, succeeding to meet the storage demand. However, the superparamagnetic limit<sup>8,9</sup> constitutes a physical constrain to the decreasing bit size, since the magnetization is no longer thermally stable below a critical diameter. Stuart Parkin and coworkers, proposed to store the information in mobile domain walls, which would open the door to 3 dimensional storage and therefore, higher densities (Figure 1.1c).



**Figure 1.1 Benchmarks in nanomagnetism.** (a) Growth of areal densities for conventional recording.[ref10] (b) The racetrack memory.<sup>6</sup> (c) Read heads developed thanks to the discovery of the GMR. (d) Drug delivery, hyperthermia and magnetic resonance imaging as examples of biomedical applications of nanomagnetism.[ref11]

Another relevant topic is the application of nanomagnets to biomedicine, illustrated in Figure 1.1d. Compared to data storage, its implantation level in the current technology is still low. Therapeutic use of nanoparticles or nanowires for cancer treatment, such as magnetic hyperthermia, is an open challenge which holds promise to give medicine a new insight in which diseases will be treated with a more localized therapy, to avoid damage on healthy tissues. The same philosophy applies to drug delivery, where nanomagnets are used to drive therapeutic drugs to specific organ tissues, conducted by an external magnetic field. On another note, magnetic resonance imaging is the most developed application of the three, and it is commonly used in hospitals as a medical diagnosis technique.

## 2.1. Micromagnetic theory

The theory of quantum mechanics provides the most accurate approach to describe ferromagnetic materials. Atomistic calculations describe N-body problem whose complexity grows with the number of atoms and it results computationally too costly unless very few of atoms are considered. To

handle the problems, different models have been developed according to the length scale of the element (table 1.1), each of them considering particular simplifications.

Model	Description	Length scale
Atomic level theory	Ab initio calculations	<1nm
Micromagnetic theory	Continuous description of magnetization	1-1000nm
Domain theory	Domain structure	1-1000 $\mu$ m
Phase theory	Ensembles of domains	>0.1mm

**Table 1.1** Established models for the description of ferromagnetic systems according to different length scales.

Amongst all the approaches, the micromagnetic theory,<sup>12</sup> formulated by William Brown Jr in 1963, has been established as the most convenient approach below one micron. This model ignores the atomic structure of materials and it focuses on the resolution of the domain structure and magnetization dynamics. The basic premise of micromagnetics is to assume the magnetization as a continuously varying function of the position,  $M_s=M(r)$  while its modulus remains constant. In static problems, micromagnetism gives insight into the spatial distribution of the magnetization by looking for configurations that follow the energy minimization criteria.

## 2.2. Energy balance

Several physical effects of diverse origins influence the total energy of a magnetic system. In the micromagnetic theory, the Landau-Lifshitz energy is the sum of five terms, some of them explained in the classical theory and others of quantum mechanical origin.<sup>13</sup>

$$E_{tot} = E_{ex} + E_a + E_d + E_z + E_{strs} + E_{ms} \quad (1)$$

To some extent, the first three terms —namely exchange ( $E_{ex}$ ), anisotropy ( $E_a$ ) and dipolar energies ( $E_d$ )- are always present. Zeeman energy arises when the ferromagnet is subjected to an external magnetic field whereas the last two terms are consequences of stress or magnetostriction.

### 2.2.1. Exchange energy

Exchange energy is a quantum mechanical effect originated due to the tendency of the ferromagnets to align magnetization in one direction, the so-called spontaneous magnetization. Deviations from this case invoke an energy penalty<sup>14</sup>, which is described by expression (2).

$$E_{ex} = \int A(\nabla e_M)^2 d^3r \quad (2)$$

where  $e_M = \mathbf{M}(r)/M_s$  is the unit vector in the local direction of the magnetization and  $A$  is the exchange stiffness. This constant, approximated to  $\approx JS^2Z_c/a_0$ , is proportional to the exchange constant  $J$  and to the number of atoms per unit cell  $Z_c$ ,  $a_0$  is the lattice parameter.

The expression is derived from the classical Heisenberg Hamiltonian for two classical neighboring spins  $S_i$  and  $S_j$ , which describes the exchange interaction between indistinguishable particles. Exchange is, therefore, a short range phenomenon.

$$H_{ij} = -J S_i S_j \quad (3)$$

The so-called exchange integral  $J$  gives rise to ferromagnetism when  $J > 0$  and to antiferromagnetism when  $J < 0$ .

### 2.2.2. Anisotropy energy

Magnetocrystalline anisotropy is a consequence of spin orbit coupling. Depending on the crystal structure of the ferromagnet, it is often energetically favorable to magnetize it in one (or more) axis. The ferromagnet reaches a local energy minimum state when it is magnetized along the easy direction.

$$E(\min) = E(-\min) \quad (4)$$

In the simplest case, when the specimen exhibits uniaxial anisotropy the energy can be simplified to the following expression:

$$E_a = \int K_1 \sin^2(\theta) d^3r + \int K_2 \sin^4(\theta) d^3r \quad (5)$$

where  $\Theta$  is the angle between the easy axis and the actual magnetization direction and  $K_1$  and  $K_2$  are first and second order constants that can be



experimentally determined. These constants are temperature dependent and thus, higher order terms are usually neglected since they are only relevant at low temperatures.

Remark that any other anisotropy are not taken into consideration in this energy term, such as the anisotropy due to shape or surface induced anisotropies.

### 2.2.3. Demagnetizing energy

The demagnetization energy, also called magnetostatic energy or stray-field energy, is the energy of the magnetization in the magnetic field created by itself, favoring configurations that minimize magnetic charges. The corresponding expression can be derived from classical electrodynamics, considering a ferromagnet under no applied magnetic field.

Since  $\mathbf{B} = \mu_0(\mathbf{M} + \mathbf{H})$  and  $\nabla \cdot \mathbf{B} = 0$ , then  $\nabla \cdot \mathbf{H}_d = -\nabla \cdot \mathbf{M}$

The energy connected to the stray field is

$$E_d = -\frac{1}{2} \int \mu_0 \mathbf{H}_d \cdot \mathbf{M} d^3r \quad (6)$$

where the  $\frac{1}{2}$  factor arises due to the reciprocity principle, since the magnetic field emerges from spins within the sample.

Due to the long range nature of this interaction, it gives rise to important effects such as *shape anisotropy*. When a particle is not perfectly spherical, the demagnetizing field will not be equal in all directions, creating one or more easy axes. As an approximation, the demagnetizing energy can be written such as

$$E_d = -\frac{\mu_0}{2} N M_s V \quad (7)$$

where  $N$  is the demagnetizing factor that varies according to the geometry of the system.

Overall anisotropy contributions in ferromagnetic materials, demagnetizing energy is particularly relevant for applications. Magnetocrystalline anisotropy is responsible of the existence of what we call magnetically hard and soft materials. Materials with high magnetocrystalline anisotropy are generally hard to demagnetize and they are commonly referred to as *hard* magnetic materials, this is a necessary feature in application such as

permanent magnets. *Soft* materials conversely –or even superparamagnetic materials with no magnetization in absence of external field- are relevant for biomedical applications. Consequently, we want to stress the importance of magnetocrystalline and shape anisotropy when it comes to create a ferromagnetic material of specific properties. Each of them provides a degree of freedom that can be harnessed to engineer different magnetic configurations.

#### 2.2.4. Other energy terms

Zeeman energy ( $E_z$ ) describes the interaction between the magnetization of a ferromagnet with the externally applied magnetic field. It favors the alignment of the spins in the direction of the external field. It can be expressed through equation (8).

$$E_z = - \int \mu_0 \mathbf{H}_{ext} \cdot \mathbf{M} d^3r \quad (8)$$

External stress  $\sigma$  applied to the sample can give rise to another energy term ( $E_{str}$ ).

$$E_{str} = - \sum_{i,j} \sigma_{ij} \varepsilon_{ij} \quad (9)$$

$\varepsilon_{ij}$  is the magnetoelastic strain tensor. Likewise, local stress can generate magnetostriction in the material. Corresponding energy ( $E_{ms}$ ) acquires the form

$$E_{ms} = \frac{1}{2} \int (p_\varepsilon - \varepsilon) \cdot c \cdot (p_\varepsilon - \varepsilon) d^3r \quad (10)$$

where  $p_\varepsilon$  is the deviation from the nonmagnetostrictive state,  $\varepsilon$  is the strain in the freely deformed state and  $c$  is the elastic tensor.<sup>15</sup>

### 2.3. Magnetic domains and domain walls

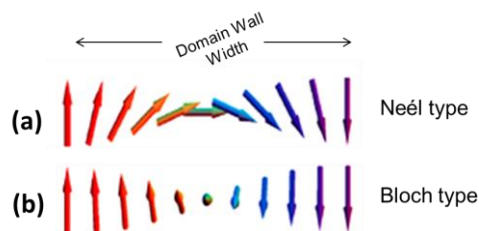
The minimization of the Gibbs free energy in the ferromagnet leads to magnetic domain formation. Magnetic domains are areas of uniform magnetization direction, separated by boundaries commonly called domain walls (DW). Their existence was proposed by Pierre Weiss in 1906 within the frame of the mean field theory.<sup>16</sup> It succeeded to explain why some materials do not exhibit net magnetization despite their ferromagnetic nature. As a matter of fact, a ferromagnet spontaneously breaks into domains when it is

cooled down below its Curie temperature whenever it is energetically favorable. The creation of a domain wall presents an energy cost, although sometimes the interplay between different energy terms leads to the formation of one or several DWs. The previous magnetic history can also be a cause of domain creation. For instance, when a saturating field is applied in a hard axis of magnetization, magnetic moments may reconfigure to form domains.

The first experimental evidence of their existence was not obtained until 1931, when Francis Bitter imaged magnetic domains for the first time through a technique that carries his name;<sup>17</sup> the Bitter colloidal technique, which consists of placing drops of a ferrofluid onto a ferromagnetic surface. The local stray field gradients trap the ferrofluid particles which form a pattern.

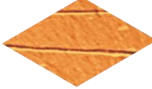

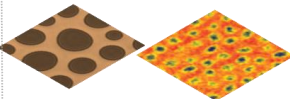
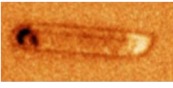
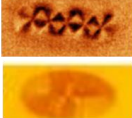
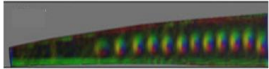

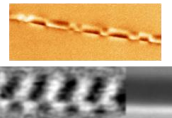
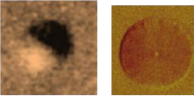
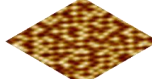
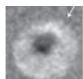
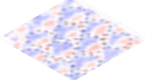
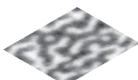
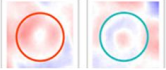
Generally, the existing type of DWs can be divided into two groups: Bloch and Néel type walls. In Néel walls spins flip within the same plane, unlike in Bloch DWs, where spins twist out of the plane which contains the initial and final spin vectors. Both domain wall types are illustrated in Figure 1.2. The type of wall depends on the geometry and magnetic features of the specimen. A relevant parameter related to domain wall formation is the domain wall width  $\delta$ , a direct measurement of the length where the magnetic moments rotate (Figure 1.2). Described as  $\delta = \sqrt{A/K_u}$ , it arises as a consequence to the interplay between the exchange interaction and overall anisotropy. The energy of a domain wall per unit area is  $\sigma_w = 4\sqrt{AK}$ . Another important characteristic length scale is the magnetic hardness parameter. It is a dimensionless ratio of anisotropy to dipolar energy defined

$$\text{as } \kappa = \sqrt{\frac{|K_1|}{\mu_0 M_s^2}}.$$



**Figure 1.2** Illustration of (a) the Néel type domain wall and (b) the Bloch type domain wall, together with their domain wall width.

Since domain structure appears as a result of the interplay between the micromagnetic energy terms explained ahead, different geometries or ferromagnetic materials of diverse features lead to the formation of a variety of domain patterns.<sup>14</sup> Some examples are illustrated in Figure 1.3.

	Soft FM	Hard FM	Other
Thin films	<p><i>Planar domains</i></p> 	<p><i>Maze domains</i></p> 	<p><i>Bubble domains Skyrmion lattices</i></p> 
Planar structures	<p><i>Single domain</i></p> 	<p><i>Multiple vortices &amp; cross tie domains</i></p> 	<p><i>Confined skyrmions</i></p> 
Wires	<p><i>Single domain</i></p> 	<p><i>Multiple vortices &amp; transversal domains</i></p> 	
Dots & Particles	<p><i>Single domain &amp; vortex</i></p> 	<p><i>OOP single domain</i></p> 	<p><i>Confined skyrmions</i></p> 
Hemispherical cups	<p><i>Vortex and onion states</i></p> 	<p><i>Serpentine domains</i></p> 	<p><i>Donuts states</i></p> 

**Figure 1.3** Examples of domains formed in magnetic nanostructures of diverse shapes and ferromagnetic materials features.

In the first place, geometry can be used as a parameter to favor the formation of specific domains. In Figure 1.3, five different morphological specimens are shown: (i) thin films, structures of one single nanoscale dimension, (ii) planar structures, typically a few micron long stripes with nanometer size width and varying shapes, (iii) nanowires (NWs, notice that although in the literature the term is given a broader meaning, we specifically refer to cylindrical shaped nanowires) with micron size length and nanoscale diameter, (iv) nanoparticles, with all dimensions in the nanoscale, (v) nanodots, cylindrical shaped nanometer sized particles and finally (vi)

hemispherical caps, self-assembly of nonmagnetic spherical nanoparticles capped with a magnetic film.

Secondly, the structures are classified according to their magnetocrystalline anisotropy, discriminating hard and soft magnetic materials. A third introduced criteria, labelled as *other*, includes combinations of materials that give rise to complex interactions, such as Moriya-Dzyaloshiinski (DMI), which is explained in more detail in section 3.4. Since materials of different compositions present different magnetic features, by tuning the composition one can favor the formation of a specific domain configuration.

Soft thin films, governed by shape anisotropy, typically display in-plane domains. Thin films with perpendicular anisotropy conversely, display out-of-plane magnetization and exhibit up and down maze domains<sup>14,19</sup> that contribute to the minimization of the overall stray field. Epitaxially grown films combining a ferromagnet with a heavy metal exhibit bubble domains or skyrmion configurations as a result of the interface interaction. Due to the degree of complexity of DMI interaction, they are explained separately in section 3.4.

Planar soft stripes with a long axis display longitudinal magnetization, forming a magnetic dipole as a result of shape anisotropy. Co based structures of similar dimensions, instead, promote a competition of the energy terms, creating complex vortex structures<sup>20</sup> or cross tie walls,<sup>21</sup> with in-plane rotating magnetization avoiding the formation of magnetic poles. The last example is a FeGe stripe with broken inversion symmetry, which displays confined skyrmions imaged by Photo Emission Electron Microscopy.<sup>22</sup>

Cylindrical nanowires are similar to stripes with the particularity of the curvature, which favors the formation of vortices. Soft specimens do also form dipolar configurations by aligning the magnetization in the axis, but in contrast to stripes, vortices are formed in the edges as a result of the circular section to minimize the magnetostatic contribution. Co based — NWs provoke vortex formation along the whole NW as a result of the energy interplay.

Nanodots are equivalent to cylindrical NWs with a nanometer size length. Permalloy nanodots, of magnetic soft nature, form vortices or dipoles

depending on their aspect ratio. Arrays of Co nanodisks<sup>23</sup> can display multidomain structures unless their dimensions are reduced until they display out-of-plane single domain configuration. Some studies have been conducted in ultrathin micron size dots with DMI interaction where skyrmions have been measured through synchrotron based imaging techniques.<sup>24</sup>

The last given example is a curved thin film that can be fabricated either as non-interacting individual caps or as a continuous film with periodical curvature. Studies in individual permalloy specimens unveil vortex or onion state formation.<sup>25</sup> On the other hand, growth of densely packed arrays of Co/Pd nanocaps can lead to the formation of out-of-plane serpentine domains.<sup>26</sup> Epitaxial growth of two materials producing DMI gives rise to individual formation of skyrmions.<sup>27</sup> Theoretical analysis claim that very thin curved geometries possess intrinsic curvature induced DMI interaction that can lead to the formation of skyrmions even in materials without DMI.<sup>28</sup>

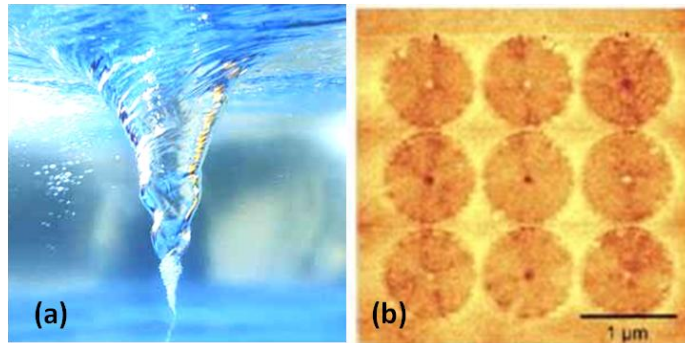
In the following sections, a deeper insight into two mentioned key configurations is given, necessary to understand the results explained in Chapter 5. Magnetic vortices are mentioned in Chapters 3, 4 and 5, in nanostructures of different materials and sizes but sharing to some extent cylindrical shape. Skyrmions, on the other hand are studied in Chapter 5.

### **2.3.1. Spin-vortex configuration**

Soft cylindrical micro and nanostructures<sup>29</sup> have been intensely investigated since the spin-vortex configuration was measured for the first time.<sup>30,31</sup> A spin-vortex is a magnetic configuration with in-plane close flux and a core pointing in the plane normal direction to avoid the creation of magnetic charges. However, vortices constitute a well-known phenomenon which is present in many other fields of physics. As in Figure 1.4a, a vortex or whirlpool is formed in water as a result suction created by the drain. In fluid dynamics, a vortex is a region in a fluid in which the flow revolves around an axis, such as tornadoes or bubble rings formed under water. In ferromagnetic materials, spins reproduce this configuration in order to minimize magnetostatic energy.

Back in the late 90s, the experimental detection of the spin-vortex constituted a breakthrough that opened new possibilities in the field of

spintronics. The first MFM images of magnetic vortices are displayed in Figure 1.4b. Envisaged for magnetic information storage technologies, the vortex spin configuration is expected to be more stable against thermal fluctuations than their single domain counterparts.<sup>33,34</sup> Vortices display four degenerate states, as a result of the combination of positive and negative chiralities and polarities (Figure 1.5a). As for applications in spintronics, vortices can also be used as spin torque nano-oscillators to generate microwaves.<sup>35</sup>



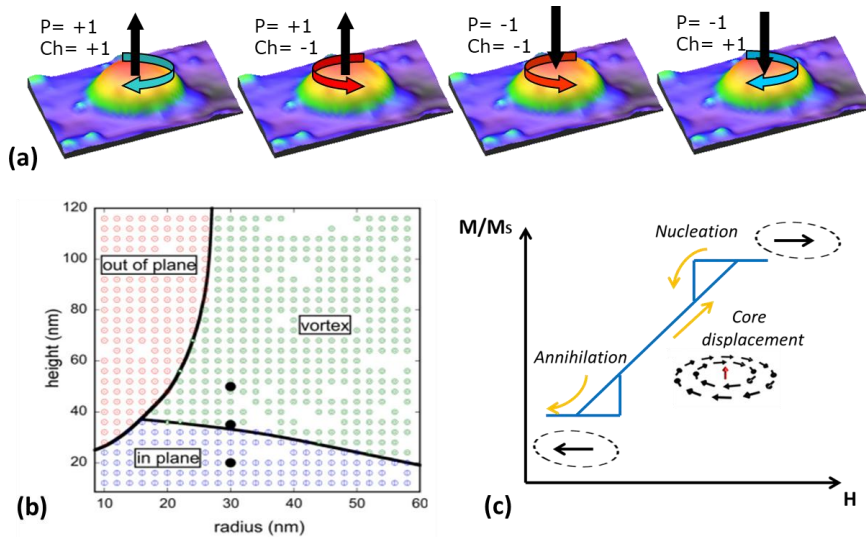
**Figure 1.4** (a) Whirlpool vortex. [ref32] (b) First image of magnetic vortices.[ref31]

Inspired by cancer treatment through magnetic hyperthermia<sup>36</sup> where cells are killed through the heat dissipated by nanoparticles under an ac magnetic field, magnetomechanical actuation<sup>37</sup> has become a trendy subject of study in the alternative cancer treatment field. In contrast to hyperthermia, where very high frequency fields are needed in order to heat the targeted cells – with detrimental effects for the human body–, magnetomechanical actuators, can generate a force capable of damaging the cancer cells even at low ac field amplitudes and frequencies.<sup>38</sup>

Any of the mentioned applications require full understanding of the magnetic behavior of the nanodisks. In this regard, many theoretical works address to predict a magnetic phase diagram -the geometrical parameters where vortex configurations are energetically stable- in soft magnetic materials<sup>39</sup> (Figure 1.5b).

In soft cylindrical nanodisks three different magnetic textures can be found in their ground state, which essentially depend on their aspect ratio ( $t/R$ ): (i) vortices, with in-plane closed flux, (ii) single domain in-plane configuration, with higher remanence, and (iii) single domain out-of-plane. The diagram shows the particular case of permalloy ( $\text{Ni}_{80}\text{Fe}_{20}$ ) nanodots. Vortices are stable in the range of the magnetic phase diagram limited by the left and lower boundaries present in the graph. The left boundary

accounts for the predominance of shape anisotropy at increasing lengths, which favors the spin alignment along the axial direction. The lower boundary applies to thin nanodots, where exchange energy hampers the vortex formation.



**Figure 1.5** (a) Degenerate states of the vortex, combining positive and negative polarities ( $P$ ) and chiralities ( $Ch$ ). (b) Magnetic phase diagram of cylindrical dots of radius  $R$  and thickness  $L$ , showing three stable magnetization states: vortex, in-plane single domain and perpendicular single domain. Adapted from [ref40] (c) Shape of the characteristic hysteresis loop of a vortex configuration.

Another well-known signature of the vortices are their characteristic hysteresis loops<sup>33</sup> (Figure 1.5c), recognizable for their two lobes close to the ends. As deduced from the plot, they lack of remanence with the vortex core centered at zero field. When subjected to an in-plane magnetic field the core displaces perpendicularly to the field, as the area where spins are aligned with the field direction grows, until they reach saturation. Along this thesis, vortex configurations are studied in nanowires (Chapter 4) and nanodisks (Chapter 5).

### 2.3.2. Magnetic Skyrmions

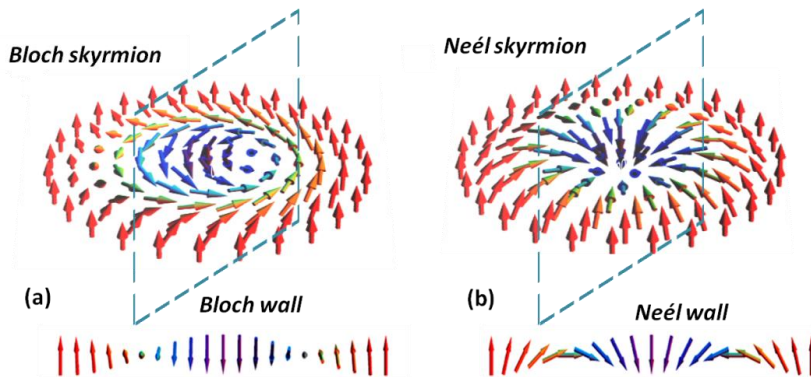
Magnetic skyrmions are local whirls of the spin configuration in a magnetic material, where spins rotate in the out of plane direction, from one edge to the center and again to the opposite edge. (Figure 1.6)



A topological description establishes the winding number  $S$  for complex structures that accounts for the number of whirls. In particular, magnetic skyrmions are characterized by a  $S = \pm 1$ , obtained from expression (11).

$$S = \frac{1}{4\pi} \int \mathbf{m}(\partial_x \mathbf{m} \times \partial_y \mathbf{m}) dx dy \quad (11)$$

The non-trivial topology governs all magnetic properties.<sup>41</sup> Particularly, the strong topological protection makes the configuration very stable. The two types of topologically equivalent magnetic skyrmions differ in the in-plane arrangement of the spins (Figure 1.6). If a vertical plane containing the skyrmion diameter is chosen, the transition from positive  $m_z$  to negative  $m_z$  occurs with spins curling perpendicular to these planes (Figure 1.7a). Skyrmions following this pattern are called Bloch skyrmions. Instead, Hedgehog (or Néel) skyrmions are characterized by a rotating out-of-plane (OOP) magnetization component from the core to the edges by means of radial curling of the spins (Figure 1.6b).



**Figure 1.6** (a) Bloch and (b) Néel or hedgehog skyrmions. Adapted from [ref42].

Their names are given one dimensional Bloch and Néel domain wall types explained ahead.<sup>43</sup> Notice that if a line containing the diameter is selected in any direction, Bloch or Néel walls are obtained.

Skyrmions were predicted by Tony Skyrme as quasiparticles in the frame of quantum field theory.<sup>44</sup> They were detected for the first time in non-centrosymmetric single crystals with broken inversion symmetry, the so-called B20 structures, where Dzyaloshinskii-Moriya interaction<sup>45,46</sup> (DMI) gives rise to topologically protected spin textures. The existence of skyrmions in thin films due to high DMI in the interface between a heavy metal and a ferromagnetic layer was later predicted<sup>47</sup> and observed.<sup>48</sup>

In addition to promising properties for spintronic based devices, skyrmions have attracted the attention of the solid state physics community due to rich physics: (i) the topological protection that ensures stability against thermal fluctuations, (ii) the low currents<sup>49</sup> needed to move them, up to 5 orders of magnitude lower than single domain configurations, and (iii) the small size that can be reduced to 20 nm. Moreover, skyrmions seem to be less prone to be pinned in defects<sup>50</sup>.

However, the implementation of skyrmionic devices requires to reach certain conditions that are still under continuous study; (i) room temperature stabilization<sup>51</sup> is mandatory for a practical device, (ii) smaller magnetic fields are needed to stabilize the skyrmions in thin films and (iii) good control of current induced manipulation of the skyrmions is equally needed.

In chapter 5, skyrmion configurations are investigated and imaged for the first time in confined systems without DMI interaction or perpendicular magnetic anisotropy (PMI).

## 2.4. Magnetization reversal

In chapters 3 to 5, field induced magnetization reversal of different nanostructures is experimentally addressed. The description of the reversal modes, however, is a non-trivial task as in real systems different types of reversal might simultaneously occur. The first analytical description of the magnetization reversal process belongs to Stoner and Wohlfarth, whose pioneer work describes the coherent rotation of spins in a single domain ferromagnet and successfully explain its hysteretic response.<sup>52</sup>

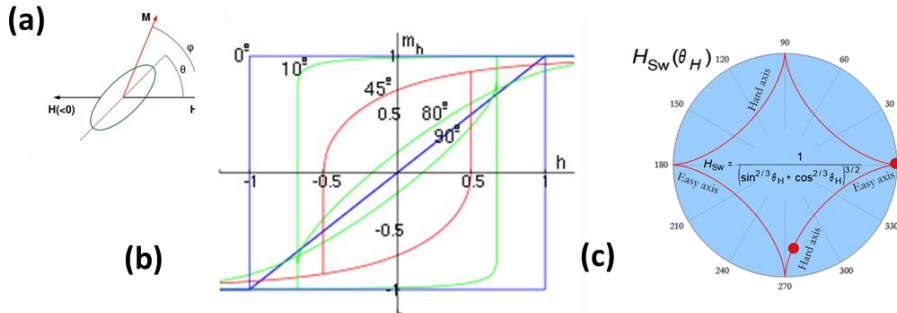
They considered the simplest approximation of the energy density of a ferromagnet described solely by the anisotropy and Zeeman terms.

$$e_{tot} = K_u \sin^2 \theta - \mu_0 M H \cos(\alpha - \theta) \quad (12)$$

where  $K_u$  is the anisotropy energy density,  $H$  is the applied field,  $\alpha$  and  $\theta$  are the angles between easy axis and the applied field, Figure 1.7a. Notice that for each value of the angle  $\theta$  at which the field is applied, there is a different solution of equation (12) that gives rise to a different hysteresis loop (Figure 1.7b). The first order partial derivative  $\frac{\partial e_{tot}}{\partial \theta} = 0$ , yields to equilibrium states, whereas switching occurs when the energy minimum becomes unstable, and condition  $\frac{\partial^2 e_{tot}}{\partial \theta^2} = 0$  is fulfilled. This is solved by two parametric equations of  $\theta$ , which can be eliminated to ultimately obtain the following expression for the switching field, known as the Stoner-Wohlfarth asteroid.

$$h_{\perp}^{2/3} + h_{\parallel}^{2/3} = 1 \quad (13)$$

Figure 1.7c represents a polar plot of the switching field, with well-defined magnetization hard and easy axis.



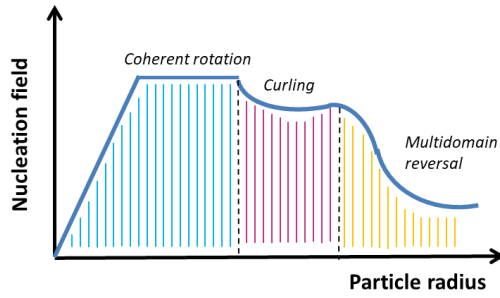
**Figure 1.7** (a) Schematic illustration of ellipsoidal particle with  $M$  magnetization under  $H$  applied field. (b) Different hysteresis loops, depending on the angle ( $\alpha - \theta$ ) between easy axis and applied field. (c) Asteroid curve characteristic of the reversal modes, defining easy and hard directions for the switching. Adapted from [ref53].

Hence, the Stoner-Wohlfarth is based on the assumption of a coherent reversal process. This model, although it predicts higher coercive values (Browns paradox<sup>12</sup>), succeeds to describe the reversal modes of small particles and sheds light into more complex reversal modes. Other models, such as curling describe the magnetization reversal mechanism in single domain particles, which avoids the large stray field caused by coherent rotation at the expense of exchange energy by passing through a vortex state. However, in most cases the studied materials possess larger dimensions than the previously described characteristic lengths –i.e.  $\delta$  domain width–.

#### 2.4.1. Domain wall nucleation, propagation and pinning

In most real systems, simultaneous reversal of all spins can no longer be assumed and more sophisticated models are needed. In fact, since the energy barrier to switch magnetization through other types of reversal modes is lower, they lead to lower nucleation fields, as it is illustrated in Figure 1.8.

In larger specimens, it is energetically less expensive to nucleate a domain with opposite magnetization and propagates it along the whole ferromagnet. Moving a domain wall requires far less energy (or field) than simultaneous reversal of all spins. In extended thin films, for instance, domains with reverse magnetization may nucleate and grow in different spots.



**Figure 1.8** Plot of the tendency of the nucleation field for different particle radius.

In uniaxially magnetized nanowires, it is known that domains nucleate in one of the ends and the domain wall propagates along the NW.<sup>54</sup> The DW velocity can be described as

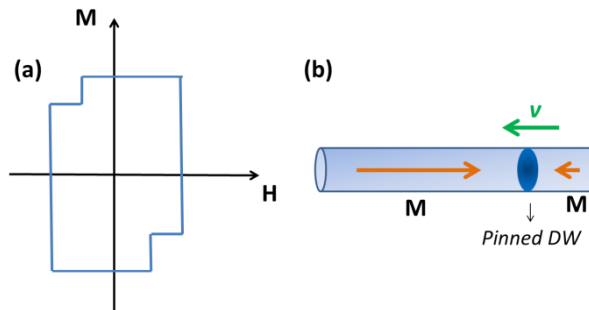
$$v_w = \mu_0 \eta_\omega (H - H_{dp}) \quad (14)$$

where  $H$  is the applied field,  $H_{dp}$  is the field needed to depin the domain wall and  $\eta_\omega$  is the domain wall mobility

$$\eta_\omega \propto \frac{\rho}{\mu_0^2 M_s t} \quad (15)$$

where  $\rho$  is the resistance of the material and  $t$  is the thickness of the section that the DW is passing through.

When during displacement domain walls bump into defects of comparable size to their dimensions, a domain might be pinned. The change in the energy landscape leads to a local energy minima, which yields small jumps (stair-shaped) hysteresis curves, instead of a large Barkhausen jump. The particular case of a NW with an axial easy axis is illustrated in Figure 1.9.



**Figure 1.9** (a) Hysteresis loop of a bistable nanowire with a small jump previous to the big Barkhausen jump due to DW pinning in a defect. (b) Schematic illustration of a NW with a domain pinned in a defect.

It is widely accepted that although the domain velocity is generally proportional to the applied field modulus, at high applied magnetic fields, the domain wall experiences a sort of braking known as *Walker Breakdown*.<sup>55,56</sup>

Domain velocities in ferromagnetic nanowires are in the order of 100m/s. The decrease in the DW propagation speed is a non-desirable effect regarding applications, since they would slow down the operation velocity of spintronic devices. However, conversely to planar structures,<sup>57,58</sup> in cylindrical shaped nanowires this phenomenon does not occur which places them in a better position to be used as bricks in applications.

## 2.5. Domain imaging techniques

Many are the characterization techniques available for the study of the magnetic behavior of nanostructures. If one is dealing with nanoobjects grown in periodically ordered self-assembled arrays, Vibrating Sample Magnetometer (VSM) performs hysteresis loops, allowing, for instance, the angular study of the coercivity, or the investigation of the interactions amongst individual objects through First-Order Reversal Curves (FORC), superconducting quantum interference devices (SQUID) serves for similar studies, but with higher sensitivity, broadening the sample spectrum to very small or low moment nanoparticles. Kerr effect microscope can perform hysteresis loops in the microscale, and it can be an imaging technique depending on the system, as we will see later. Magnetic resonance is a spectroscopy technique used to study the spin dynamics in ferromagnetic materials. All these techniques contribute to the understanding of the collective behavior of the system.

However, though imaging techniques one can directly visualize the domain configuration of nanoobjects, without having to make any assumptions as it does indeed happen when indirect measurements are performed. As explained before, magnetic imaging happened to be a crucial factor for the understanding and confirmation of the domain theory and for this reason; additional techniques have been developed after the Bitter colloidal technique.

Imaging techniques range from expensive equipment only accessible in big facilities, such as synchrotron based techniques (X-ray Magnetic Circular Dichroism-Photo Electron Emission Microscopy (XMCD-PEEM)) or Transmission Electron Microscopy based techniques (Electron Holography or Lorentz Microscopy); to other more commonly used techniques such as Scanning Probe Microscopy based techniques (Spin Polarized –Scanning Tunneling Microscopy (STM), Magnetic Force Microscopy, Magnetic

Exchange Force Microscopy (MExFM)), Kerr effect microscopy (MOKE) or the formerly used bitter colloid techniques.

### 3.7.1. XMCD-PEEM:

X-ray Magnetic circular dichroism<sup>59</sup> is a recently developed synchrotron based technique. Magnetic dichroism describes the property of a ferromagnetic material whose transmittance depends on the orientation of polarized light incident upon it. One of the assets of this technique is its capability to image topography simultaneously with compositional and magnetic contrasts.

X-rays are emitted against the studied sample with a grazing angle of  $16^\circ$ . In 3 dimensional nanoobjects, a shadow is created and two types of contrast can be obtained (See Figure 1.20, where a NW imaging has been taking as an example). The first type of contrast is directly collected from the surface electrons. Since the photoelectrons are released after incident x-rays collide against it, they penetrate no more than 5nm. The second type of contrast has information from the inner part (core) of the three dimensional object, after x-rays penetrate and generate photoemission from the substrate (after interact with the inner part of the NW). This constitutes the biggest advantage of this technique, which can after all give us superficial and inner information of the magnetization of the specimens. XMCD is thus very convenient to study NWs, in particular those displaying core-shell magnetic configurations, which cannot be unveiled by surface techniques. Its lateral resolution lies around 20nm.<sup>60</sup>

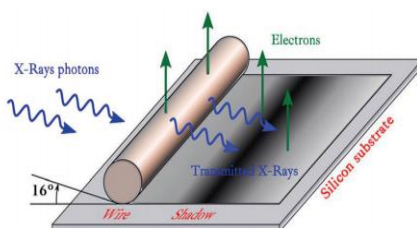


Figure 1.20 Illustration of the working mode of XMCD. Taken from [ref61].

### 3.7.2. Transmission Electron Microscopy based techniques

Lorentz Transmission Electron Microscopy (LTEM)<sup>62</sup> and Electron Holography (EH)<sup>63,64</sup> can be realized with a High Resolution Transmission Electron Microscope. LTEM is a generic name to describe all imaging modes in which contrast is generated as a result of the deflection experienced by electrons

as they pass through a region of magnetic induction. The Lorentz deflection angle  $\beta_L$  is given by

$$\beta_L = e\lambda t(\mathbf{B}\mathbf{x}\mathbf{n})/h, \quad (16)$$

where  $\mathbf{B}$  is the induction averaged along an electron trajectory,  $\mathbf{n}$  is a unit vector parallel to the incident beam,  $t$  is the specimen thickness and  $\lambda$  is the electron wavelength. This means that LTEM is sensitive to *in-plane* magnetization.

The physics beneath EH conversely, are based on the Aharonov-Bohm effect<sup>65</sup>, a quantum mechanical phenomenon that describes how a charged particle can be affected by an electromagnetic field, even when traveling through a region of space in which both electric and magnetic field are zero.

Off-axis Electron Holography relies on the formation of an interference pattern (or hologram) in the transmission electron microscope (TEM). In contrast to LTEM, records the spatial distribution of image intensity, EH also allows the phase shift of the high-energy electron wave that has passed through the studied element to be measured directly. The phase shift is used to provide information about local variations in magnetic induction and electrostatic potential within and around the nanostructure. It can be expressed as

$$\phi(x) = C_E \int V(x, y) dz - \left(\frac{e}{\hbar}\right) \iint B_{\perp}(x, z) dx dz, \quad (17)$$

where  $C_E$  is an electric field dependent constant,  $z$  is the electron beam direction,  $x$  is a direction in the plane of the nanostructure,  $B_{\perp}$  is the perpendicular component in of the magnetic induction and  $V$  is the electrostatic potential.

Both techniques offer the chance to image structural properties of samples with very high resolution (down to 0.2 nm), extract compositional information and carry out magnetic imaging at once.

### 3.7.3. Kerr effect microscopy

Magneto-optical microscopes are based on Kerr (or Faraday) effects. Polarized light reflected (or transmitted) from magnetized materials rotates slightly its plane of polarization. The domain contrast in the image is directly sensitive to the magnitude and direction of magnetization. This technique constitutes a very powerful tool for domain imaging in the microscale, with remarkable time-resolved imaging capability due to its high data acquisition speed. Its resolution is however limited by the size of the incident laser spot,

which is in the best cases close to the wavelength of the light. In several works about magnetic NWs, it has been used as a tool to perform local minor hysteresis loops which allows extracting meaningful information about DW pinning effects or the magnetization easy axis.<sup>61,66</sup>

#### **3.7.4. Other SPM techniques**

Several of the Scanning Probe Microscopy techniques possess magnetic sensitivity. Of particular relevance, the Spin-Polarized Scanning Tunnel Microscope (SP-STM),<sup>67,68</sup> which is a especial operation mode of the STM. Contrary to MFM, which all in all senses the magnetic dipolar interaction between sample and tip, this technique possesses the capability to detect magnetic phenomena on the single-atom scale. A STM sharp tip coated with a ferromagnetic material scans the sample while a voltage is applied between them to have a net tunnel current. In the absence of magnetic phenomena, the strength of this generated current is indicative for local electronic properties. However, the singularity of SP-STM is that it is based on the magnetoresistance tunnel effect, which makes it more likely for electrons with spins matching the tip magnetization to be tunneled.

Magnetic Exchange Force microscopy,<sup>69</sup> on the other hand, also developed by the group of Roland Wiesendanger, unlike STM based techniques, it is not limited to the study of conducting samples. Based on the AFM system setup, it probes short range magnetic exchange force between two closely spaced spins for imaging, at very small tip-sample distances (typically 0.5 nm).

To achieve such high resolution, both techniques require Ultra High vacuum conditions, flat surfaces and very good control over the apex atom spin polarization. They are not suited, anyway, to measure the type of nanostructures studied in this manuscript.

#### **3.7.5. Assets and drawbacks of MFM**

Magnetic Force Microscopy, the technique applied along this thesis, based on the interaction of the sample with a thin magnetic probe scanned over the sample, presents advantages and drawbacks compared to the previously explained imaging techniques. Its operation mode is explained in detail in Chapter 2.

Amongst the drawbacks, MFM does not yet easily provide quantitative output, being this one of the open challenges for the MFM community.<sup>70,71</sup> On the other hand, the presence of a magnetic coating in the tip can alter the magnetic configuration of the studied samples, particularly in those which are magnetically soft. This effect can be skipped by choosing the right coating, although a MFM user should always be careful to avoid wrong



interpretation of images. Having said that, quite remarkably, in certain works the stray field of the tip has been used for the controlled manipulation of the magnetic state of the sample<sup>72</sup> or domain injection.<sup>73</sup>

Unlike XMCD-PEEM, MFM does not provide clear information of the magnetization of the core of the nanowires. Instead, it images a sum of contributions to the out-of-plane component of the magnetization gradient. MFM was conceived as a surface technique, and when it is used to study 3D nanoobjects, complementary micromagnetic simulations are advisable. It should be pointed out that different configurations might lead to similar MFM images.

Nevertheless, the availability and cost of MFM is considerably lower than any of the ahead mentioned techniques. Getting beam time in a synchrotron facility is not accessible for every group and the measurement time is always very restricted. In the case of Electron Holography, the cost of a HR-TEM is far beyond a regular AFM, which is present in many research laboratories. Additionally, EH requires complex analysis of the output data.

Moreover, in terms of resolution MFM provides a better lateral resolution – below 20nm- than XMCD-PEEM, very high sensitivity and well defined images. Images can be recorded at any desired conditions, from vacuum conditions to air and liquid media.<sup>74</sup> Unlike in other techniques, for MFM no special preparation of the sample is required.

Finally, MFM allows studying the samples under in-situ field, opening the chance to explore different magnetic states and their evolution.

## References

1. Feynman, R. P. Plenty of Room at the Bottom. *Am. Phys. Soc.* 1–11 (1959). doi:10.1007/s12045-011-0109-x
2. Stamps, R. L. *et al.* The 2014 Magnetism Roadmap. *Journal of Physics D: Applied Physics* **47**, (2014).
3. Sander, D. *et al.* The 2017 Magnetism Roadmap. *Journal of Physics D: Applied Physics* **50**, (2017).
4. Baibich, M. N. *et al.* Giant magnetoresistance of (001)Fe/(001)Cr magnetic superlattices. *Phys. Rev. Lett.* **61**, 2472–2475 (1988).
5. Grünberg, P. *et al.* Layered magnetic structures: Evidence for antiferromagnetic coupling of Fe layers across Cr interlayers. *J. Appl. Phys.* **61**, 3750–3752 (1987).
6. Parkin, S. S. P., Hayashi, M. & Thomas, L. Magnetic domain-wall racetrack memory. *Science* **320**, 190–194 (2008).
7. Parkin, S. & Yang, S. H. Memory on the racetrack. *Nature Nanotechnology* **10**, 195–198 (2015).
8. White, R. L. Physical boundaries to high-density magnetic recording. *J. Magn. Magn. Mater.* **209**, 1–5 (2000).
9. Weller, D. & Moser, A. Thermal effect limits in ultrahigh-density magnetic recording. *IEEE Trans. Magn.* **35**, 4423–4439 (1999).
10. Wood, R. Future hard disk drive systems. *J. Magn. Magn. Mater.* **321**, 555–561 (2009).
11. No Title. Available at: [www.trialx.com/curetalk](http://www.trialx.com/curetalk).
12. William Fuller Brown. *Micromagnetics*. (Wiley, 1963).
13. Aharoni, A. Introduction to the Theory of Ferromagnetism. *Oxford Sci. Publ.* **I**, 303 (2007).
14. Hubert Alex & Schäfer, R. *Magnetic Domains. Magnetic Domains: The Analysis of Magnetic Microstructures* **40**, (1998).
15. Coey, J. *Magnetism and magnetic materials. Physics* **12**, (2010).
16. Weiss, P. La variation du ferromagnetisme du temperature. *Comptes Rendus* **143**, 1136–1149 (1906).
17. Bitter, F. On inhomogeneities in the magnetization of ferromagnetic materials [1]. *Physical Review* **38**, 1903–1905 (1931).
18. Domain walls. Available at: <https://www.utwente.nl/en/tnw/cms/research/mesaplus-annual-reports/ar2012-dw/>.

19. Dho, J., Kim, Y. N., Hwang, Y. S., Kim, J. C. & Hur, N. H. Strain-induced magnetic stripe domains in La<sub>0.7</sub>Sr<sub>0.3</sub>MnO<sub>3</sub> thin films. *Appl. Phys. Lett.* **82**, 1434–1436 (2003).
20. Ivanov, Y. P., Iglesias-Freire, O., Pustovalov, E. V., Chubykalo-Fesenko, O. & Asenjo, A. Magnetic configurations of Co(111) nanostripes with competing shape and crystalline anisotropies. *Phys. Rev. B - Condens. Matter Mater. Phys.* **87**, (2013).
21. Löhndorf, M., Wadas, A., Van Den Berg, H. A. M. & Wiesendanger, R. Structure of cross-tie wall in thin Co films resolved by magnetic force microscopy. *Appl. Phys. Lett.* **68**, 3635–3637 (1996).
22. Jin, C. *et al.* Control of morphology and formation of highly geometrically confined magnetic skyrmions. *Nat. Commun.* **8**, (2017).
23. Thomson, T., Hu, G. & Terris, B. D. Intrinsic distribution of magnetic anisotropy in thin films probed by patterned nanostructures. *Phys. Rev. Lett.* **96**, 1–4 (2006).
24. Boulle, O. *et al.* Room-temperature chiral magnetic skyrmions in ultrathin magnetic nanostructures. *Nat. Nanotechnol.* **11**, 449–454 (2016).
25. Streubel, R. *et al.* Equilibrium magnetic states in individual hemispherical permalloy caps. *Appl. Phys. Lett.* **101**, (2012).
26. Albrecht, M. *et al.* Magnetic multilayers on nanospheres. *Nat. Mater.* **4**, 203–206 (2005).
27. Streubel, R. *et al.* Manipulating topological states by imprinting non-collinear spin textures. *Sci. Rep.* **5**, (2015).
28. Streubel, R. *et al.* Magnetism in curved geometries. *J. Phys. D. Appl. Phys.* **49**, (2016).
29. Im, M.-Y. *et al.* Symmetry breaking in the formation of magnetic vortex states in a permalloy nanodisk. *Nat. Commun.* **3**, 983 (2012).
30. Cowburn, R. P., Koltsov, D. K., Adeyeye, A. O., Welland, M. E. & Tricker, D. M. Single-domain circular nanomagnets. *Phys. Rev. Lett.* **83**, 1042–1045 (1999).
31. Shinjo, T., Okuno, T., Hassdorf, R., Shigeto, K. & Ono, T. Magnetic vortex core observation in circular dots of permalloy. *Science (80-. )*. **289**, 930–932 (2000).
32. How Tornadoes Work.
33. Guslienko, K. Y. & Novosad, V. Vortex state stability in soft magnetic cylindrical nanodots. *J. Appl. Phys.* **96**, 4451–4455 (2004).
34. Schneider, M., Hoffmann, H., Otto, S., Haug, T. & Zweck, J. Stability of magnetic vortices in flat submicron permalloy cylinders. *J. Appl. Phys.* **92**, 1466–1472 (2002).
35. Dussaux, A. *et al.* Large microwave generation from current-driven magnetic vortex oscillators in magnetic tunnel junctions. *Nat. Commun.* **1**, (2010).
36. Salunkhe, a B., Khot, V. M. & Pawar, S. H. Magnetic hyperthermia with magnetic nanoparticles: a status review. *Curr. Top. Med. Chem.* **14**, 572–94 (2014).

37. Contreras, M. F., Sougrat, R., Zaher, A., Ravasi, T. & Kosel, J. Non-chemotoxic induction of cancer cell death using magnetic nanowires. *Int. J. Nanomedicine* **10**, 2141–2153 (2015).
38. Kim, D. H. *et al.* Biofunctionalized magnetic-vortex microdiscs for targeted cancer-cell destruction. *Nat. Mater.* **9**, 165–171 (2010).
39. K. Yu. Guslienko. Magnetic Vortex State Stability, Reversal and Dynamics in Restricted Geometries. *J. Nanosci. Nanotechnol.* **8**, 2745–2760 (2008).
40. Goiriena-Goikoetxea, M., García-Arribas, A., Rouco, M., Svalov, A. V. & Barandiaran, J. M. High-yield fabrication of 60 nm Permalloy nanodiscs in well-defined magnetic vortex state for biomedical applications. *Nanotechnology* **27**, (2016).
41. Nagaosa, N. & Tokura, Y. Topological properties and dynamics of magnetic skyrmions. *Nature Nanotechnology* **8**, 899–911 (2013).
42. Kezsmarki, I. *et al.* Neel-type skyrmion lattice with confined orientation in the polar magnetic semiconductor GaV4S8. *Nat. Mater.* **14**, 1116–1122 (2015).
43. Lilley, B. A. LXXI. Energies and widths of domain boundaries in ferromagnetics. *London, Edinburgh, Dublin Philos. Mag. J. Sci.* **41**, 792–813 (1950).
44. Skyrme, T. H. R. A unified field theory of mesons and baryons. *Nucl. Phys.* **31**, 556–569 (1962).
45. Yu, X. Z. *et al.* Real-space observation of a two-dimensional skyrmion crystal. *Nature* **465**, 901–904 (2010).
46. Mühlbauer, S. *et al.* Skyrmion lattice in a chiral magnet. *Science (80-. )*. **323**, 915–919 (2009).
47. Bogdanov, A. N. & Röbber, U. K. Chiral Symmetry Breaking in Magnetic Thin Films and Multilayers. *Phys. Rev. Lett.* **87**, 37203 (2001).
48. Heinze, S. *et al.* Spontaneous atomic-scale magnetic skyrmion lattice in two dimensions. *Nat. Phys.* **7**, 713–718 (2011).
49. Jonietz, F. *et al.* Spin transfer torques in MnSi at ultralow current densities. *Science (80-. )*. **330**, 1648–1651 (2010).
50. Iwasaki, J., Mochizuki, M. & Nagaosa, N. Current-induced skyrmion dynamics in constricted geometries. *Nat. Nanotechnol.* **8**, 742–747 (2013).
51. Soumyanarayanan, A. *et al.* Tunable room-temperature magnetic skyrmions in Ir/Fe/Co/Pt multilayers. *Nat. Mater.* **16**, 898–904 (2017).
52. Stoner, E. C. & Wohlfarth, E. P. A mechanism of magnetic hysteresis in heterosis in heterogeneous alloys. *Phil. Trans. Roy.Soc.* **A-240**, 599–642 (1948).
53. Stoner Wohlfarth model. Available at: [https://en.wikipedia.org/wiki/Stoner-Wohlfarth\\_model](https://en.wikipedia.org/wiki/Stoner-Wohlfarth_model).
54. Ferguson, C. A., Maclaren, D. A. & McVitie, S. Metastable magnetic domain walls in

- cylindrical nanowires. *J. Magn. Magn. Mater.* **381**, 457–462 (2015).
55. Glathe, S., Mattheis, R. & Berkov, D. V. Direct observation and control of the Walker breakdown process during a field driven domain wall motion. *Appl. Phys. Lett.* **93**, (2008).
  56. Mougin, A., Cormier, M., Adam, J. P., Metaxas, P. J. & Ferré, J. Domain wall mobility, stability and Walker breakdown in magnetic nanowires. *EPL* **78**, (2007).
  57. Burn, D. M. & Atkinson, D. Suppression of Walker breakdown in magnetic domain wall propagation through structural control of spin wave emission. *Appl. Phys. Lett.* **102**, (2013).
  58. Yan, M., Kákay, A., Gliga, S. & Hertel, R. Beating the Walker limit with massless domain walls in cylindrical nanowires. *Phys. Rev. Lett.* **104**, (2010).
  59. Stöhr, J., Padmore, H. A., Anders, S., Stammler, T. & Scheinfein, M. R. Principles of X-Ray Magnetic Dichroism Spectromicroscopy. *Surf. Rev. Lett.* **5**, 1297–1308 (1998).
  60. Aballe, L., Foerster, M., Pellegrin, E., Nicolas, J. & Ferrer, S. The ALBA spectroscopic LEEM-PEEM experimental station: Layout and performance. *J. Synchrotron Radiat.* **22**, 745–752 (2015).
  61. Bran, C. *et al.* Spin configuration of cylindrical bamboo-like magnetic nanowires. *J. Mater. Chem. C* **4**, 978–984 (2016).
  62. Chapman, J. N. & Scheinfein, M. R. Transmission electron microscopies of magnetic microstructures. *J. Magn. Magn. Mater.* **200**, 729–740 (1999).
  63. Lichte, H. & Lehmann, M. Electron holography—basics and applications. *Reports Prog. Phys.* **71**, 16102 (2008).
  64. Thomas, J. M., Simpson, E. T., Kasama, T. & Dunin-Borkowski, R. E. Electron holography for the study of magnetic nanomaterials. *Acc. Chem. Res.* **41**, 665–674 (2008).
  65. Aharonov, Y. & Bohm, D. Further considerations on electromagnetic potentials in the quantum theory. *Phys. Rev.* **123**, 1511–1524 (1961).
  66. Palmero, E. M., Bran, C., Del Real, R. P. & Vázquez, M. Vortex domain wall propagation in periodically modulated diameter FeCoCu nanowire as determined by the magneto-optical Kerr effect. *Nanotechnology* **26**, (2015).
  67. Wiesendanger, R., Güntherodt, H. J., Güntherodt, G., Gambino, R. J. & Ruf, R. Observation of vacuum tunneling of spin-polarized electrons with the scanning tunneling microscope. *Phys. Rev. Lett.* **65**, 247–250 (1990).
  68. Wiesendanger, R. Spin mapping at the nanoscale and atomic scale. *Rev. Mod. Phys.* **81**, 1495–1550 (2009).
  69. Kaiser, U., Schwarz, A. & Wiesendanger, R. Magnetic exchange force microscopy with atomic resolution. *Nature* **446**, 522–525 (2007).
  70. Panchal, V. *et al.* Calibration of multi-layered probes with low/high magnetic

- moments. *Sci. Rep.* **7**, 1–13 (2017).
71. Hug, H. J. *et al.* Quantitative magnetic force microscopy on perpendicularly magnetized samples. *J. Appl. Phys.* **83**, 5609–5620 (1998).
  72. Wang, Y. L. *et al.* Rewritable artificial magnetic charge ice. *Science (80-. )*. **352**, 962–966 (2016).
  73. Gartside, J. C., Burn, D. M., Cohen, L. F. & Branford, W. R. A novel method for the injection and manipulation of magnetic charge states in nanostructures. *Sci. Rep.* **6**, (2016).
  74. Ares, P., Jaafar, M., Gil, A., Gómez-Herrero, J. & Asenjo, A. Magnetic Force Microscopy in Liquids. *Small* **11**, 4731–4736 (2015).

# **CHAPTER 2:**

# **Magnetic Force**

# **Microscopy**

This chapter is dedicated to the key tool used throughout this thesis: the Magnetic Force Microscope (MFM). The chapter is divided into three sections. First, a short overview of Scanning Force Microscopy (SFM) is presented, stressing its versatile nature to characterize different sort of interactions in the nanoscale and explaining some basic concepts. Secondly, general details of the MFM operation mode are explained together with intrinsic limitations to the state-of-art of the technique. In the third part, the importance of the most critical element in the microscope -the MFM probe- is highlighted. The fabrication of custom MFM tips according to the specific requirements of each experiment is of uttermost importance, in particular, to obtain non-altered images of soft samples that could not be properly measured with commercial tips. The tips have been customized for most of the experiments presented along this thesis. Remarkably, tips to measure in liquid conditions have been developed. These new kind of probes open the path to future research on magnetic specimens with applicability in nanomedicine, as the samples presented in the following chapters of this manuscript. Finally, an Appendix (A) has been added to discuss the convenience of carrying out micromagnetic modelling to complement experimental MFM data. Based on the micromagnetic theory formulated by W. Brown, micromagnetic simulation packages assume many simplifications. The applicability as well as the limitations of the micromagnetic modelling is discussed.

## **1. Scanning Probe Microscopy**

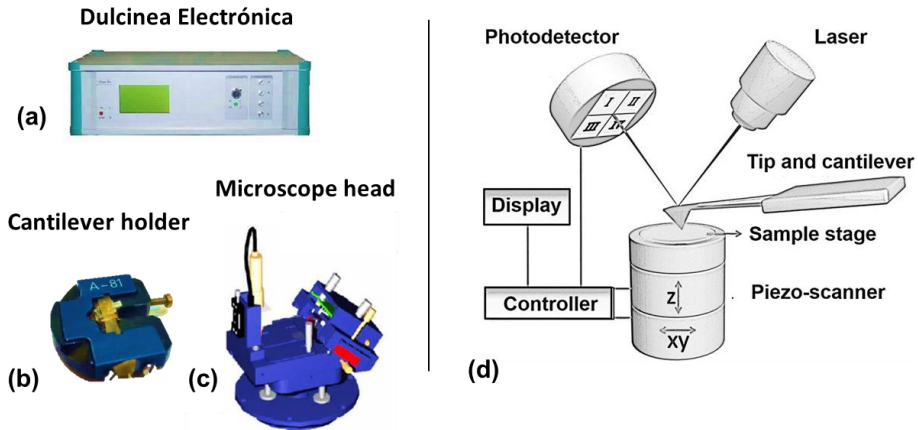
The main part of this thesis has been developed through Magnetic Force Microscopy (MFM)<sup>1,2</sup> measurements. MFM is an operation mode of the Atomic Force Microscope (AFM), a nanoscale characterization tool that was developed by G. Binnig and C. Quate<sup>3</sup> from IBM, after the invention of its precursor, the Scanning Tunnel Microscope<sup>4</sup> (STM). The irruption of STM constituted a tremendous breakthrough in the field of nanoscience and as a reward; Binnig and Rohrer were awarded with the Nobel Prize in 1986. It opened the path to the development of the Scanning Probe Microscopies<sup>5</sup> (SPM) family which entailed rapid progress in different research fields due to their wide range of applicability. Amongst them, the Near-Field Scanning Optical Microscope<sup>6</sup> (SNOM) or the Atomic Force Microscope arose. One of the main assets of SPM lies in its versatility to measure interactions of



different origins at the nanoscale. Atomic Force Microscopies are based on the interaction between the sample and a sharp probe. By simply adjusting the probe features, the AFM user has access to the detection of a wide range of interactions, such as mechanical properties, electronic transport properties, surface potential, magnetic interactions, chemical forces, thermal gradients, etc.

### **1.1. Fundamentals**

The AFM<sup>3</sup> consists of a cantilever with a very sharp probe at its end –apex radius  $\sim 10$  nm- that is used to scan the sample surface. The cantilever is typically made of silicon or silicon nitride with a tip radius of curvature on the order of nanometers. It is manufactured by microfabrication techniques and its features (shape of the probe, coating and microcantilever force constant) are selected depending on the type of sample and the properties that will be explored. Briefly explained, when the tip is brought close to the sample surface, forces between tip and sample lead to the deflection of the cantilever that obeys Hooke's law. The system used along this thesis, a custom modified Cervantes model, was commercialized by Nanotec Electrónica S.L. and the software WSxM<sup>7</sup> was used for data acquisition. Its detection system, integrated in the microscope head, consists of an incident laser which points at the end of the cantilever and whose light is reflected and collected by a 4 sectional photodiode (Figure 2.1). The cantilever deflection is thus detected through the displacement of the reflected laser spot on the photodiode. Other microscope brands commercialize systems where the tip deflection is detected using a fiber interferometric sensor.<sup>8</sup> As in Figure 2.1., the sample is mounted on a three axis displacement tubular piezo-scanner that allows scanning. The cantilever is piezoacoustically excited, through a dithering piezo that vibrates with the application of a voltage. Additionally, an optical microscope helps the user to localize different areas of the sample.



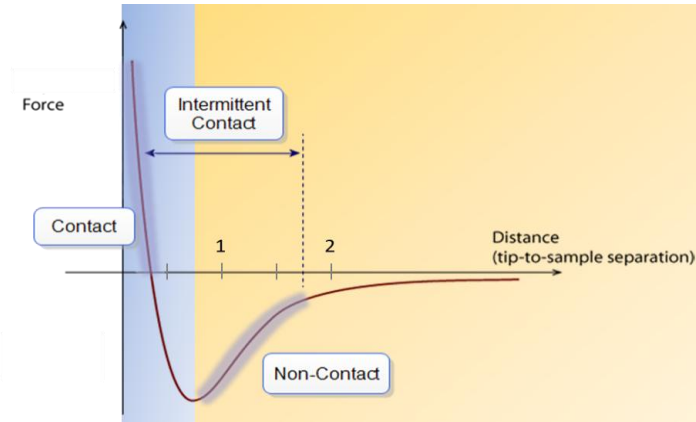
**Figure 2.1** Parts of the experimental set-up: (a) Control electronic system, (b) cantilever holder and (c) microscope head. (d) Show schematically the main components of the head with the piezo scanner where the sample is mounted. Adapted from [ref9].

At short distances, the Lennard-Jones potential describes the interactive forces:

$$w(r) = -A/r^6 + B/r^{12} \quad (1)$$

where  $r$  is the separation between tip and sample and  $A$  and  $B$  are interaction constants. In the resulting curve (Figure 2.2), two regimes are distinguished: in the proximity of the sample the tip experiences repulsive interaction whilst going a bit further the attractive region can be reached.

The two widespread imaging modes, each of them with their assets and drawbacks, serve for different purposes. The contact-mode is performed in the repulsive regime, where the tip is dragged over the sample, using the cantilever deflection as a feedback signal to keep the cantilever at constant height. However, the second mode, namely the dynamic mode,<sup>10</sup> is the most versatile. The cantilever is oscillated close to its resonant frequency while the tip scans the sample closely. This mode enables not only to avoid tip degradation, but it also provides the opportunity to obtain further simultaneous information from the sample from the detection of additional observables such as oscillation amplitude, phase shift, frequency shift, etc. The dynamic mode is the standard operation mode in magnetic force microscopy.



**Figure 2.2** Tip-sample short range interaction given by the Lennard-Jones potential. Repulsive regime has been colored in light blue and attractive in light orange. Adapted from [ref11].

## 1.2. Dynamic mode

### 1.2.1. Fundamentals

There are two main dynamic AFM modes depending on the parameter chosen for the main feedback loop. Amplitude modulation (AM),<sup>12</sup> which is the mode that has been used along this thesis, utilizes the oscillation amplitude as a feedback to image the topography of the sample. It is widely used for imaging in air. In Frequency Modulation (FM)<sup>13</sup> conversely, appropriate to work in ultra-high vacuum (UHV), the oscillation frequency is used as a reference channel. While frequency-modulated images are being recorded, an additional feedback loop is used to keep the oscillation amplitude constant by adjusting the drive amplitude. This mode allows separating conservative and non-conservative interactions.

Point mass models<sup>14,15</sup> provide a formal description of the cantilever motion in dynamic atomic force microscopy, assuming the cantilever to be a micromechanical oscillator of point mass  $m$  and elastic constant  $k$ . The equation of motion includes the local tip-sample interaction, the dissipative forces that buffer the motion with a damping coefficient  $\mu$  and the driving force  $F_{exc}(t)$  that excites the cantilever. Therefore the system can be described by the equation of a driven harmonic oscillator:

$$F(t) - kz - \mu \frac{dz}{dt} = m \frac{d^2z}{dt^2} \quad (2)$$

The external driving force is provided by a small piezoelectric placed on the cantilever holder that is subjected to an AC voltage and provides mechanical vibration of frequency  $\omega$  to the cantilever.

$$F(t) = F_0(\omega t) \quad (3)$$

If we rearrange the terms in the equation we can define the natural frequency  $\omega_0$  and the quality factor  $Q$  of the oscillation.

$$\frac{d^2z}{dt^2} + \frac{\mu}{m} \frac{dz}{dt} + \frac{k}{m} z = \frac{F(t)}{m} \quad (4)$$

$$\omega_0 = 2\pi f_0 = \sqrt{\frac{k}{m}} \quad (5)$$

$$Q = \frac{m\omega_0}{\mu} \quad (6)$$

Equation (4) can be solved for any driving force with no loss of generality, using the solutions  $z(t)$  that satisfy the unforced equation, where  $F(t) = 0$ . Damped sinusoidal oscillations solve the equation.

$$z(t) = A e^{-\frac{\omega_0 t}{2Q}} \sin\left(\sqrt{1 - \left(\frac{1}{2Q}\right)^2} \omega_0 t + \varphi_0\right) \quad (7)$$

Where the amplitude and phase, as a function of the frequency, acquire the form:

$$A(\omega) = \frac{F_0/m}{\sqrt{(\omega_0^2 - \omega^2)^2 + (\omega\omega_0/Q)^2}} \quad (8)$$

$$\varphi = \tan^{-1} \frac{\omega\omega_0/Q}{\omega_0^2 - \omega^2} \quad (9)$$

Notably, the oscillation amplitude and phase depend on the quality factor  $Q$ . The lever resonance frequency, which is modified by the damping, can be related to the resonator natural frequency through the following formula:

$$\omega_r = \omega_0 \sqrt{1 - \frac{1}{2Q^2}} \quad (10)$$

The above mentioned observables, namely amplitude, phase and frequency, constitute information channels that account for different interactions. Changes in the resonance frequency are recorded to study various interactions, such as for instance, magnetostatic. When the tip-sample interactions  $F_{ts}$  are considered, several approximations need to be made in order to simplify the motion equation. If interactions are small enough to be described as perturbations of the cantilever motion,  $F_{ts}$  can be expanded into Taylor series as follows:

$$F(t) + F_{ts} - kz - \mu \frac{dz}{dt} = m \frac{d^2z}{dt^2} \quad (11)$$

$$F_{t-s} = F_{t-s}(z=0) + \left(\frac{dF_{t-s}}{dz}\right) z + \frac{1}{2!} \left(\frac{d^2F_{t-s}}{dz^2}\right) z^2 + \dots + \frac{1}{n!} \left(\frac{d^n F_{t-s}}{dz^n}\right) z^n \quad (12)$$

The first two terms of the expansion are introduced in equation 11 whilst the rest are neglected.

$$m \frac{d^2z}{dt^2} + \mu \frac{dz}{dt} = \left[ k - \left(\frac{dF_{t-s}}{dz}\right) \right] z = F(t) + F_{ts} \quad (13)$$

$$k_{eff} = \left[ k - \left(\frac{dF_{t-s}}{dz}\right) \right] \quad (14)$$

$$\omega_{eff} \approx \sqrt{\frac{k_{eff}}{m}} = \sqrt{\frac{\left[ k - \left(\frac{dF_{t-s}}{dz}\right) \right]}{m}} = \sqrt{\frac{k}{m}} \sqrt{1 - \frac{\left(\frac{dF_{t-s}}{dz}\right)}{k}} \quad (15)$$

Since the gradient is considered as a perturbation of the motion  $\frac{\left(\frac{dF_{t-s}}{dz}\right)}{k} \ll 1$ , function  $f(x) = c\sqrt{1-x}$  is also expanded as a first order Taylor polynomial.

$$\omega_{eff} \approx \sqrt{\frac{k}{m}} \left( 1 - \frac{\left(\frac{dF_{t-s}}{dz}\right)}{2k} \right) \quad (16)$$

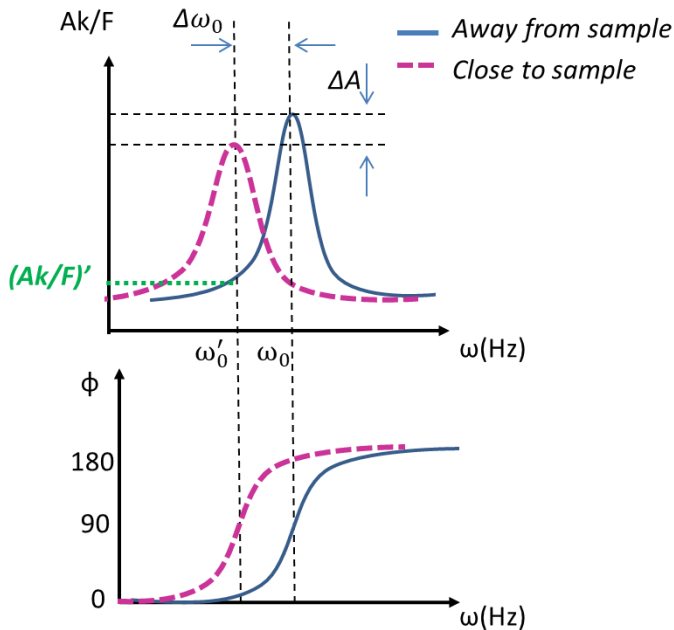
$$\Delta\omega_{eff} = \frac{\omega_0}{2k} \left(\frac{dF_{t-s}}{dz}\right) \quad (17)$$

Thus, the effective frequency shift gives us a measure of the force gradient experienced by the tip due to the interaction with the sample. However, we need to keep in mind that this approximation is only valid when oscillations are very small.

In the last years, other advanced modes have been developed based on the simultaneous excitation of two or more cantilever eigenmodes. Multifrequency AFM, proposed by the group of Prof. Ricardo Garcia,<sup>16,17</sup> is now a well-established method amongst the AFM community, although it has not been performed in the work presented in this manuscript.

### 1.2.2. Phase Lock Loop

Along this thesis, the use of the Phase Lock Loop (PLL) was systematic. This is a second feedback loop that keeps the phase constant (close to  $90^\circ$ ) when the tip is in the range of the sample interaction. As we see in Figure 2.3., if the tip is subjected to attractive force gradients, the amplitude transfer function  $Ak/F$  experiences a shift to the left, which means that the cantilever changes its natural frequency from  $\omega_0$  to a smaller frequency value  $\omega_0'$ . Additionally, the curve becomes wider and flatter. These two curves have been plotted according to equations 8 and 9 in section 1.2.1.

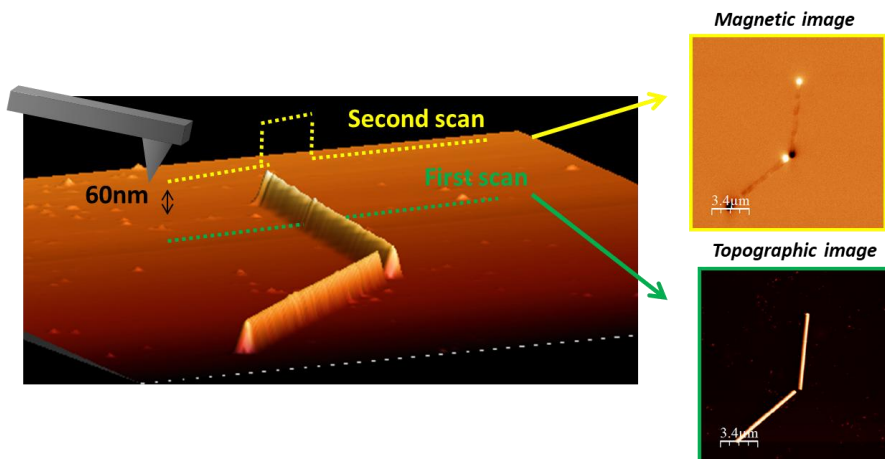


**Figure 2.3** Change in the amplitude transfer function and phase lag as a result of bringing the tip under the influence of the sample attractive interaction.

If the PLL is not enabled when the tip approaches the sample, the corresponding amplitude transfer function decreases to  $(Ak/F)'$  -marked with a green dashed line- due to (i) the shift of the curve and (ii) the fact that the new curve is flattered. When dissipative forces are present, it is advisable to enable the PLL to avoid this amplitude loss. This feedback introduces little changes in the excitation frequency to maximize the amplitude.

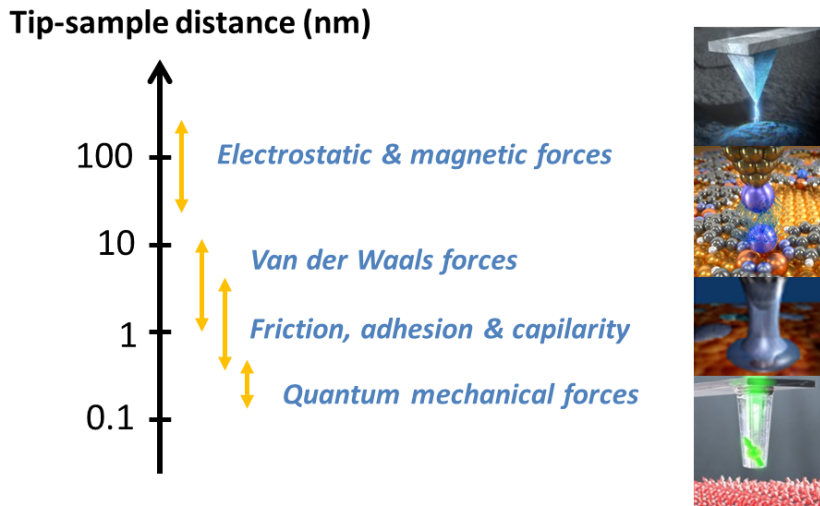
## 2. Magnetic Force Microscopy

As pointed out before, Magnetic Force Microscopy is a particular operation mode of the Atomic Force Microscope which was separately developed by two SPM groups in 1987. If a magnetic coating is provided to regular AFM tips, they become sensitive to stray fields of ferromagnetic samples. Magnetic coatings, typically composed CoCr or simply Co, possess between 25 to 50 nm thicknesses. We demonstrated before that the force gradients, under some specific conditions, can be obtained recording variations in the resonance frequency of the cantilever. The detection of magnetic interactions requires, as a result, operating the system in the dynamic mode as well as enabling the two pass mode (Figure 2.4).



**Figure 2.4** Two pass mode to measure the topography and the magnetic signal in magnetic nanowires.

The two pass mode<sup>18</sup> takes advantage of the fact that each type of interaction is dominant at a different length scale (tip sample distance, Figure 2.5). As a matter of fact, in our experiments we work in the attractive regime, where van der Waals interaction perturbs the cantilever motion and consequently the topographic signal is obtained. This is followed by a second scan of the same line with the tip withdrawn few tens of nanometers, distance beyond which the tip is mainly sensitive to electrostatic or magnetic (long-range) forces. For the measurement of flat surfaces, the second pass can be maintained at constant height.



**Figure 2.5** Dominant interactions in the different tip sample length scales. Images adapted from [ref19].

However, for the samples studied along this thesis, the second pass is required to repeat the profile obtained in the first scan, to avoid topographic crosstalk. This is the most common method when dealing with larger samples with sharp morphological changes.

The magnetic energy of a ferromagnetic tip with  $\mathbf{M}_{tip}$  magnetic moment in the presence of the sample stray field  $\mathbf{H}_{sam}$  is given by the integral

$$E = -\mu_0 \int (\mathbf{M}_{tip} \cdot \mathbf{H}_{sam}) dV_s \quad (18)$$

The force experienced by the tip can be derived from the energy gradient.



$$F_{t-s} = -grad (E(r)) \quad (19)$$

$$F_{t-s} = \mu_0 \int \nabla (M_{tip} H_{sample}) dV_{tip} = \mu_0 \left[ \int m_x \frac{\partial H_{sample,x}}{\partial x} + \int m_y \frac{\partial H_{sample,y}}{\partial y} + \int m_z \frac{\partial H_{sample,z}}{\partial z} \right] \quad (20)$$

Equation 17, that correlates the frequency shift and the force gradient, can be applied to magnetostatic interaction:

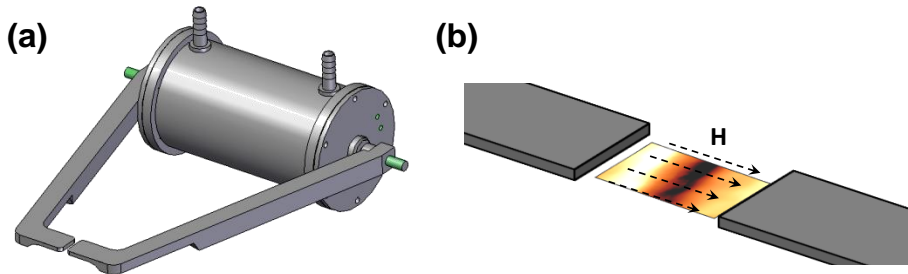
$$\Delta\omega_{eff} = -\frac{\omega_0 \mu_0 m_{tip}}{2k} \left( \frac{\partial^2 H_{sample,z}}{\partial z^2} \right) \quad (21)$$

Therefore, in MFM as the tip probes the sample, the frequency shift in the retrace mode is indicative of the tip-sample magnetic force gradient. These expressions have been derived neglecting mutual influence between them.

At this point, it is important to stress that when the two pass mode is performed, the detected force gradient might account for any long range forces. This might be an asset if the user can separate the contributions, but generally it constitutes a problem for non-expert MFM users that can lead to misinterpretation of the MFM signal.<sup>20</sup>

## 2.1. Variable Field MFM

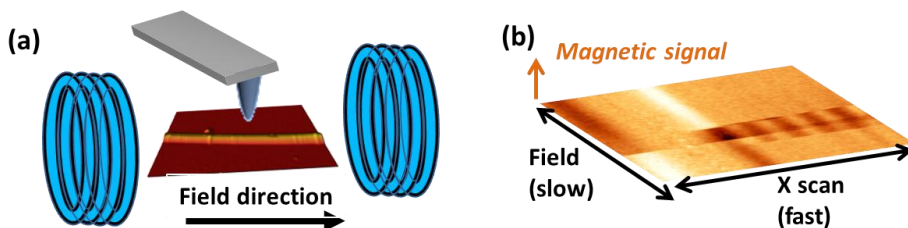
On top of this, in the experimental set-up two coils systems have been added to the MFM to apply *in-situ* field to the sample<sup>21</sup>, as shown in Figure 2.6. The simple magnetic circuit consists of a copper wire solenoid coupled to a soft iron path that conducts flux lines to a gap, where the sample is placed. The fields are controlled though a power supply operated with the software. The Variable-Field (VF) MFM measurements presented in the manuscript have been performed under in-plane magnetic fields that can reach up to 800 Oe. This option is of uttermost importance, since it opens the path to the study of different configuration at changing magnetization stages plus the quantification of critical fields.



**Figure 2.6** (a) Schematic view of the experimental coil. (b) Gap between soft iron pieces.  
Courtesy of Dr. Pablo Ares and Dr. Miriam Jaafar.

## 2.2. 3D modes

The 3D mode<sup>22</sup> concept has been extensively exploited along this thesis, to study subtle changes occurring to the magnetic configuration under applied magnetic field. This mode allows recording information of one single scan line of the sample, while a selected magnitude (tip sample distance, magnetic field, etc.) is swept.<sup>22</sup> Although it permits to measure typical SPM magnitudes as function of any other two magnitudes of the system, in our particular case, they have been utilized to perform a magnetic field sweep in the slow scan line (see Figure 2.7), while frequency shift channel is recorded as output.<sup>23,24</sup>



**Figure 2.7** (a) Scheme of the non-standard advanced MFM operation mode where the magnetic field is applied in the axis of the wire while the magnetic signal is recorded along this line. (b) Output image when non-standard VF-MFM measurements are conducted.

This technique has proven to be very convenient to unveil features of magnetization reversal processes that cannot be detected through standard VF-MFM due to constraints related to image acquisition timings. As a matter of fact, we benefit not only from the time saving from imaging a single scan line, but also from the speed at which this measurement can be performed,

which can reach 8Hz. For clarity, along this thesis we refer to these operation modes as *Advanced VF-MFM modes*.

### 2.3. Combination of MFM with Kelvin Probe Force Microscopy

Accumulated charges on the surface or different work functions of tip and sample, might lead to a voltage difference between tip and sample. Considering that magnetic and electrostatic interactions are strong in the same range, namely from 20 to 100nm above the surface, a crosstalk effect can appear.

To discriminate magnetic and electric signals, it is often necessary to perform simultaneous MFM and Kelvin Probe Force Microscopy (KPFM),<sup>25</sup> which is an SFM mode to measure the contact potential map between tip and sample. Enabling the two modes at the same time<sup>26</sup> allows point-by-point compensation of the electrostatic signal to cancel it out and obtain a purely magnetic contrast.

Formally, an AC voltage  $V_{AC}$  and a bias voltage  $V_{DC}$  are applied to the tip

$$V = (V_{DC} - V_{CPD}) + V_{AC} \cdot \sin(\omega t) \quad (22)$$

The tip and sample can be considered as a capacitive system (of capacitance  $C$ ), whose acting force is given by

$$F = \frac{1}{2} \frac{dC}{dz} V^2 \quad (23)$$

Introducing expression 22 in equation 23 and rearranging the terms yields three force terms

$$\mathbf{F} = \mathbf{F}_{DC} + \mathbf{F}_{\omega} + \mathbf{F}_{2\omega} \quad (24)$$

where

$$F_{DC} = \frac{dC}{dz} \left[ \frac{1}{2} (V_{DC} - V_{CPD})^2 + \frac{1}{4} V_{AC}^2 \right] \quad (25)$$

$$F_{\omega} = \frac{dC}{dz} [V_{DC} - V_{CPD}] V_{AC} \sin(\omega t) \quad (26)$$

$$F_{2\omega} = -\frac{1}{4} \frac{dC}{dz} V_{AC}^2 \cos(2\omega t) \quad (27)$$

In order to cancel out the electrostatic interaction between the tip and the sample, the component of the force that oscillates  $\sin(\omega t)$  (equation 26) is nullified by applying the corresponding  $V_{dc}$  at each tip point; this is the output of the Kelvin feedback.

In some cases the combination of MFM and KPFM modes is essential to avoid misinterpretation of the images.<sup>20</sup>

### 3. Tip engineering

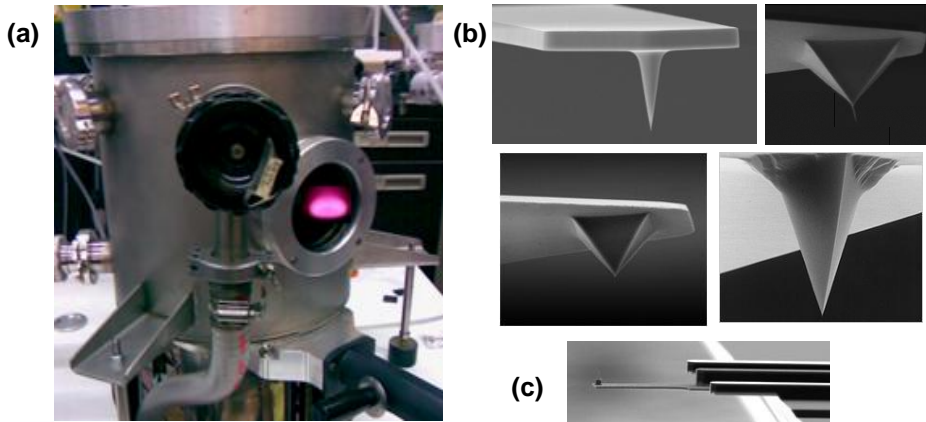
The tip is generally considered the most critical element of the microscope. As explained before, different tip coatings can be used to probe a variety of nanoscale interactions. On the other hand, depending on the sample and the required working mode, the tip characteristics must be carefully selected. Despite the wide choice of AFM tips offered in the market, along this thesis it was found that they do not always suit specific requirements to perform non-standard or subtle measurement. For this reason, this third part of chapter 2 is dedicated to the instrumental development carried out to adapt commercial AFM tips to measurements presented in this manuscript as well as for additional research lines that remain open.

To carry out MFM measurement, AFM tips need to be functionalized with a magnetic element. However, before taking this step we need to carefully think of the type of sample we need to measure in terms of size, magnetic coercivity, mechanical hardness, electrical properties, etc. Prior to the selection of the magnetic sensitive element, there are two main features that need to be chosen: tip ending shape and cantilever force constant (see Figures 2.8b and 2.8c)

The tip shape affects not only the lateral resolution of the measurement, but also the stray fields due to field line concentration in sharp enough tips. In

addition, different effects can arise if, for instance, a single face of a pyramidal tip is coated, instead of the full pyramid.

The lever force constant constitutes the second degree of freedom. Mechanically soft samples require low force constant microcantilevers to avoid damage, while harder cantilevers provide bigger stability to the measurement. As it will be later addressed, the choice of the lever has major implications in the magnetic signal to noise ratio.



**Figure 2.8** (a) Sputtering chamber used to coat AFM tips with Cobalt. (b) AFM tips with different shape available in the market. (c) AFM tip with a 70 $\mu$ m cantilever, from NT-MDT.

Previous work carried out in the group laid the ground for further development of tips for specific purposes.<sup>18,19,29</sup> In the work here presented, most of the probes have been coated through physical sputtered deposition.<sup>30</sup> However, in the last part some alternatives to this method are presented and their assets and drawbacks are discussed.

Sputtering is performed in home-built system (Figure 2.8) which consists of a vacuum chamber with two magnetrons and a Radio Frequency power supply. Cobalt and Chromium targets have been used. The depositing parameters – optimized in a previous work<sup>27</sup> – are carefully chosen to ensure highly flat surfaces with small grain size. The coating process is conducted as follows: The sample is placed inside the chamber and the pressure is lowered to  $10^{-6}$  mbar, then argon is introduced in the chamber and the plasma ignition pressure is selected to  $2.5 \times 10^{-2}$ . Choosing 90W and 295V of bias voltage, the

plasma lights up and the working pressure is reduced to  $10^{-2}$ . The output thickness is controlled by the deposition time.

### 3.1. Low moment tips coated by sputtering

The minimization of the tip stray field influence over the sample is a common concern for every MFM group<sup>31</sup> and it has been a frequently addressed problem throughout this thesis. Many of the results presented in Chapters 4 and 5 have been performed with home-coated low moment tips, to avoid artifacts caused by commercial tips, which usually have large stray fields.

A MFM user needs to keep in mind that the MFM contrast does not give direct information from the sample magnetization, but it rather accounts for tip-sample interaction. Thus, chances are that the MFM probe alters the configuration of the sample, or conversely, that the sample magnetization reverses the tip magnetization. Hartmann et al. established the necessary conditions to avoid these artifacts.<sup>32</sup>

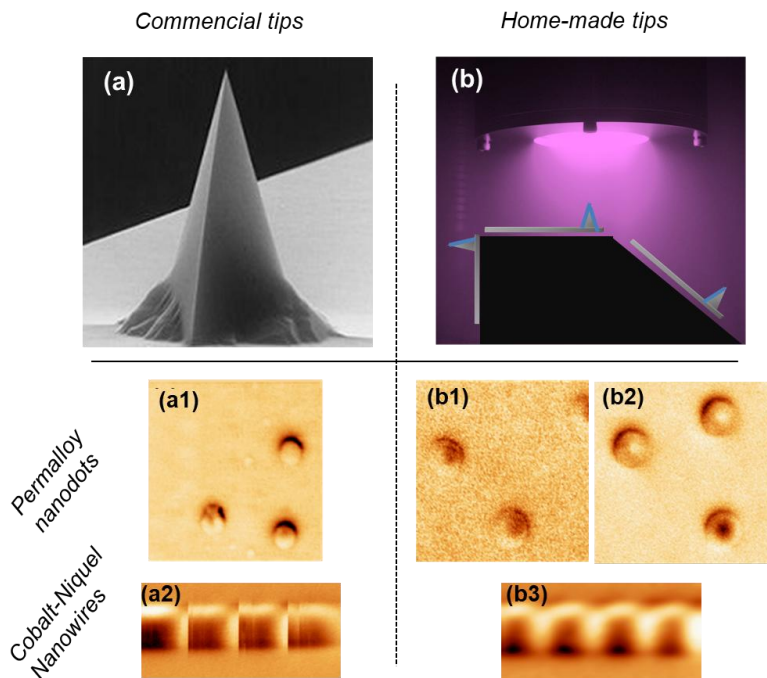
$$H_k^{sam} > M_s^{tip} \quad (28)$$

$$H_k^{tip} > M_s^{sam} \quad (29)$$

where  $H_k$  is the anisotropy field and  $M_s$  is the saturation magnetization. The fulfilment of the first condition entails that the tip does not alter the magnetic configuration of the sample, while the second condition implies that the sample does not provoke a switching of the tip magnetic state. Consequently, a material with high coercivity is preferred for the magnetic coating of the probes and with an adequate stray field depending on the studied sample.<sup>29</sup> Commercial tips are made of a CoCr alloy, but they possess high stray field to ensure good sensitivity.

The study of soft nanodots, addressed in chapter 5, is one of the objectives of this thesis. The measurement of this particular type sample constitutes a major challenge due to two main reasons: (i) The low signal - stray field- of Py together with its magnetically soft nature hinders the MFM probe selection; a tip which is sufficiently sensitive is needed that, at the same

time, does not modify the magnetic configuration of the nanodots. The task of choosing the right tip is not straightforward. A first attempt was performed with a commercial low moment tip from Nanosensors, but the probe was discarded due to strong effect on the sample magnetic configuration (Figure 2.9a1). (ii) The size of the nanodots lies close to the lateral resolution of the MFM tip. It should be noted that the lateral resolution of the AFM is always limited by the tip-sample convolution effect it is, in the best cases, above 10nm. In MFM tips, the magnetic coating of the MFM tips increases the tip final diameter, compromising the lateral resolution. Furthermore, considering that the magnetic images in air are performed at least at 20nm retrace distances to avoid topographic crosstalk, the achievement of a resolution below 20nm requires very good working conditions.



**Figure 2.9** (a) Commercial PPP- MFM R Nanosensors MFM tip and (b) sketch showing the possible manners of placing the tips in the holder, to grow the ferromagnetic coating in different ways, with the same type of lever. (a1), (b1) and (c1) are resulting images of Py nanodots using different tips. (a2) and (b3) show a piece of a soft CoNi NW imaged with a commercial and a home-made tip.

To measure soft nanodots, cantilevers with 3N/m force constant and pyramidal tips of triangular base have been chosen. In view of the size of the nanodots (140nm of diameter), some attempts were performed using lateral coated tips.<sup>29</sup> Coating one single face of the pyramid allows keeping a thinner tip apex diameter, as well as well-defined perpendicular tip magnetization. These tips have shown to be high performance probes for several samples with sizes close to the resolution. Nevertheless, to image vortices lateral coating breaks the symmetry of the tip, displacing the magnetic layer axis -and thus the magnetic image- from the topographic one (see Figure 2.9b1).

After different attempts, a 45nm thick Co layer was deposited, which resulted to be the optimum thickness for imaging (Figure 2.9b2). Notice that this thickness corresponds to a simultaneously grown thin film and that the layer deposited onto the pyramid, considering its shape, the efficient coating should be thinner than this nominal value. This approach was also used to measure soft magnetic nanowires in Chapter 4 (Figure 2.9b3).

In summary, when commercial tips influence the sample magnetization, coating AFM tips by sputtering deposition is a good approach. The design of the optimal tip to measure a particular sample requires, the performance of several attempts, varying the coating thickness and its configuration.

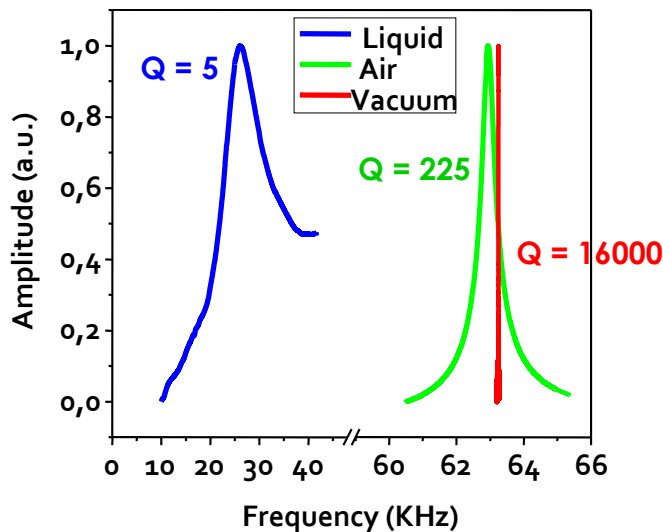
### **3.2. Tips for liquid environments**

The incorporation of nanomagnets to the field of nanomedicine constitutes a striking challenge for the groups working in nanomagnetism. Applications such as magnetic hyperthermia, magnetic resonance imaging or drug delivery –where nanoparticles are used as agents to lead the drug to a precise organ, guided by externally applied fields<sup>33</sup> - involve new demands in terms of characterization at the nanoscale. In particular, the study of the nanowires and nanodots presented in this thesis has been financially supported by two national projects that i) envisage the use of these magnets for hyperthermia and water decontamination ii) are focused on instrumental development of the microscope to characterize magnetic biological specimens.



Conducting the study of nanoparticles in biological media would be highly desirable, for instance, within organic tissues or encapsulated in virus capsids.<sup>34</sup> Several works are aimed to pave the way to the applicability of MFM for the detection of magnetic nanostructures in liquid environments.<sup>35,36,37</sup> In the most recent of all, from Ares et al., despite obtaining reasonable lateral resolution as well as enough signal-to-noise ratio in a 30 nm oxide nanoparticles, the quality of the images is still far from those in air conditions, due to the low oscillation quality factor in liquid environment (Figure 2.10), an intrinsic limitation of the technique. As the authors claim in the article, the development of suitable MFM probes would enhance the signal/noise ratio.

In many cases, working with biological samples such as viruses,<sup>38,39</sup> requires specific conditions to avoid damage due to the pressure applied by the probe. As a matter of fact, operating the system in the dynamic mode happens to be less harmful,<sup>40</sup> in addition to the use of low force constant AFM probes.<sup>41</sup> Besides, as pointed out by Ares et al., the implementation of magnetic tips with low cantilever force constants and higher resonance frequency would significantly improve the signal to noise ratio, despite increasing the fundamental noise level.



**Figure 2.10** Resonant curves of a commercial cantilever in different environments. Taken from [ref36].

A simple calculation can be made to obtain of the signal to noise ratio improvement if a low constant lever is used. In dynamic AFM the signal noise is proportional to  $\sqrt{1/kQ}$ <sup>10</sup>, whereas the signal is proportional to  $\omega_0/k$ .

Cantilever	$k$ (N/m)	$\omega_{res}$ (kHz)
A	2	75
B	0.1	110

**Table 2.1** Features of a standard force constant cantilever (A), typically used for air MFM measurements, and a soft non-magnetic (B) cantilever, typically used for measurements in liquid media.

In Table 2.1 we have gathered the force constant and resonance frequency that belong to tip A (Nanosensors PPP- MFM & Budget Sensors, MagneticMulti75-G) and tip B (softer lever tip, Olympus BioleverMini BL-AC40TS-C2). Using these values, we can calculate the signal-noise ratio  $r$  improvement due to the utilization of a softer cantilever.

$$r = \omega_0 \sqrt{\frac{Q}{k}} \quad (30)$$

$$r_B/r_A \sim 4.5 \quad (31)$$

In view that theory predicts an improvement in the signal to noise ratio, low  $k$  MFM tips available from different companies in the market –Team Nanotech, Mikro-masch-were tried and compared to a 2N/m  $k$  commercial MFM tip from Nanosensors (details in table 2.2). However, all of them failed to perform measurements under reasonable stability conditions in water.

company	name	Nominal $k$ (N/m)	Problems
Nanosensors <sup>42</sup>	PPP-MRMR	2	Poor signal-to-noise ratio
Team Nanotec <sup>43</sup>	HR-MFM	0.7	Degradation of magnetic coating
Mikro-masch <sup>44</sup>	NSC36/Co-Cr/Al BS	0.6	Unstable in liquid & degradation of magnetic coating

**Table 2.2** Summary of the probes used to measure MFM in liquid.

Olympus company commercializes a probe called Biolever Mini,<sup>45</sup> commonly used for liquid experiments. It is characterized by a very short lever ( $L \sim 40 \mu\text{m}$ ) which gives rise to a low force constant of  $0.1 \text{N/m}$  and  $110 \text{kHz}$  resonance frequency in air. This kind of levers, with small force constants were coated with cobalt by physical sputter deposition.<sup>29</sup>

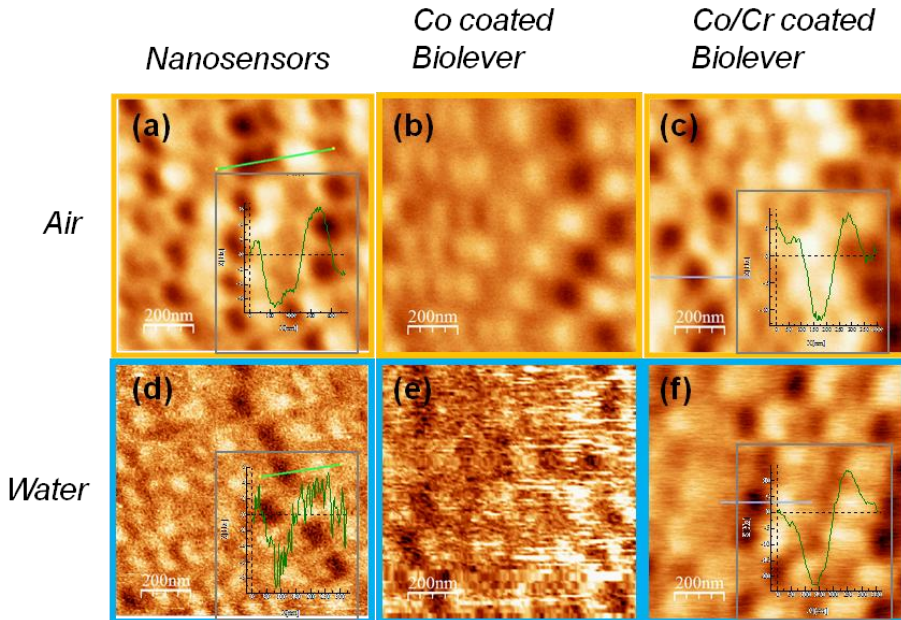
For experiments in liquids, generally, imaging was performed through the Drive Amplitude-Modulation (DAM) operation mode<sup>46</sup>, which is similar to FM and provides higher stability. Briefly, this mode developed and patented by D. Martínez-Martín, M. Jaafar and J. Gómez Herrero (from Universidad Autónoma de Madrid) in 2011 bases its performance in the use of two nested feedback loops: one to maintain the cantilever oscillation amplitude constant by adjusting the driving force, and a second one where the driving force is used as the feedback variable for topography imaging. Using the DAM operation mode, allows getting closer to the sample than in AM,<sup>36</sup> and avoids magnetic crosstalk in the topographic signal as compared to FM, since there are no contributions to the frequency shift in topography.

On a first attempt, the Biolever probe was fully coated by sputtering with  $30 \text{ nm}$  of Co and a calibration sample ( $320 \text{ Gb}$  hard disk with well-defined out-of-plane domains) was measured to evaluate the quality of the images. The experiment was carried out as follows: (i) a first image was performed in air conditions, (ii) the probe was dipped into water, making sure to form a water meniscus with the sample to perform an image and finally (iii) the tip and sample were properly dried and a new image was recorded. The output images are displayed in Figure 2.11.

Notably, the image performed in air conditions possesses a very high signal compared to those performed by commercial AFM tips of  $K=2 \text{N/m}$ . On the contrary, the image performed in water lacks of a good signal-to-noise ratio, owing to high noise which hampers the stabilization of the tip. The subsequent image carried out after drying the tip and sample displays significantly lower MFM signal compared to the very first image of the sequence. This fact evidences that when the tip is dipped in water, either the Co layer oxidizes with the consequent loss of magnetic sensitivity or that the magnetic coating layer detaches from the tip apex.

The combination of the Biolever Mini with a ferromagnetic coating is partially successful. Our next concern is to find a suitable protective layer to avoid damage coming from oxidation or detachment of the magnetic coating. In this context, chromium is a widespread used material to improve adhesion between layers. The deposition of a thin layer of Cr on the probe prior to the Co deposition could prevent the detachment of Co when introduced in water. Additionally, an outer Cr layer could also hinder the oxidation of the ferromagnetic layer. Several combinations were tried to obtain a good magnetic signal, together with a sufficient protection without raising the tip radius. With the aim of increasing the tip stray field, some attempts were addressed to the coating of a unique face of the tip pyramid. The main problems of this approach are that if one single face is coated, the chromium capping layer is less efficient and does not fully protect the ferromagnetic layer.

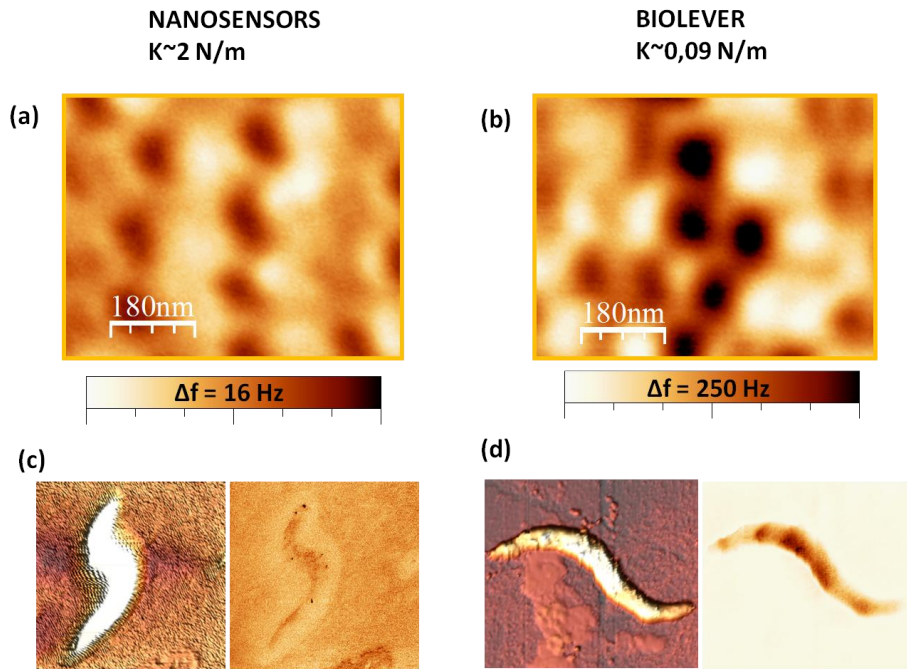
The best signal-to-noise ratio images were obtained by growing Cr (4 nm)/Co (30 nm)/Cr (4 nm) multilayers onto the tip. In Figure 2.11 a comparison between images obtained with commercial MFM tips and home coated Biolever Mini is presented. Remarkably, in liquid measurements the home coated Biolever minimizes the noise displayed by the commercial nanosensors (Figure 2.11f) which opens the possibility to image samples with biological interest. We have therefore succeeded to design and fabricate a high performance MFM tip which is stable to measure in liquid media.



**Figure 2.11** Comparison between images obtained both in air and in liquid media of a calibration sample (HD), with (a) & (c) a PPP-MFMR from Nanosensors, (b) a home-coated Co Biolever Mini and (c) a home coated Co/Cr Biolever mini.

### 3.3. Enhanced sensitivity tips

Along the previous investigation, we found that Co coated Biolevers resulted in very high performance MFM probes, providing large signals up to one order of magnitude beyond the commonly used commercial MFM tips. Co coated Biolevers possess higher sensitivity than the standard ones, which is convenient to image (i) samples of very low signal and (ii) soft samples whose magnetic configuration is altered by standard MFM tips. Due to the high signal of Biolevers, a thinner coating is required to obtain reasonable signals, which leads to similar signals than commercial MFM tips with lower tip stray fields. We have found that although fabrication companies do not advice the use of Biolevers in air, it is possible to use them in ambient conditions.



**Figure 2.12** (a) Magnetic image of a HD performed with a nanosensors PPP-MFMR. (b) Equivalent image of a HD, performed with a biolever with the comparable coating thickness to PPP-MRMR. Topographic and MFM images of a magnetotactic bacteria performed with (c) a nanosensors probe and (d) a biolever. All images obtained in air.

In Figure 2.12, the resulting images performed with standard MFM tip and a coated biolever Mini, evidence that a much higher signal is obtained with the second, under the similar working conditions. Remarkably, by changing the lever mechanical properties, the frequency shift range rises from 16 to 250 Hz – while the force gradient, which is proportional to the tip and sample magnetization, does not change significantly, despite having less magnetic material in the biolever. It is  $4.1 \times 10^{-2}$  N/m for the biolever, compared to the  $8.5 \times 10^{-2}$  N/m obtained with the nanosensors. The final apex of the tip can also influence this fact, as in sharper tips generate higher stray field.

In view of these results, these tips allow us to address the MFM characterization of magnetotactic bacterias.<sup>47,48</sup> These measurements have been performed in the frame of an ongoing collaboration with the group of Professor M.L. Fernandez-Gubieda, from the University of the Basque Country. This system entails serious complications to measure when it comes to detect their magnetic signals. They can be 1-3  $\mu\text{m}$  high, depending on

their state, and they contain chains of magnetite nanoparticles of a few tens of nanometers of size. The chain is buried into the bacteria and therefore, the tip-nanoparticle distances can be very high, leading to very small tip-sample interaction. To overcome this barrier, we have used Co coated biolevers. We want to stress that (i) the magnetic signal arises as a result of the use of a higher sensitivity probe (Figure 2.12d) and (ii) topographic image is pretty stable when measuring with a BioleverMini.

After significantly improving signal-to-noise ratio, ongoing work on this research line is addressed to measure magnetotactic bacterias as well as virus capsids with ferromagnetic particles in biological media.

### **3.4. Alternatives to sputtering: using magnetic nanowires as probes**

So far, several challenges have been overcome by growing a ferromagnetic coating through physical sputtering deposition. In the literature, however, several works propose different approaches to make an AFM tip magnetic.<sup>49,50</sup> In most cases, they constitute an attempt to address one of the main unresolved issues amongst the MFM community: to provide quantitative data about the sample magnetization. This is due, in part, to the difficulty to characterize the magnetic probes properly. Even if this problem is solved, the calculation of the magnetization pattern from the measured signal is equally not-trivial since it requires the inverse solution of a three-dimensional convolution integral.<sup>51</sup>

One of the approaches to overcome this drawback consists in the application of simplifying tip-sample models. Commercial pyramidal tips are too far from behaving like magnetic monopoles or dipoles. In this regard, it was proposed to utilize nanoparticles, nanowires and Fe filled carbon nanotubes<sup>52</sup> as MFM probes, since their dimensions and magnetic features can be easily quantified. Moreover, in the elongated probes, owing to their axial magnetization they can be considered as a monopole. J.M Garcia et al. proposed to use electrodeposited magnetic nanowires as overall monopole behavior MFM probes.<sup>53,54</sup> Shortly after, G. Yang et al. reported the feasibility of performing good resolution MFM images with NWs attached to the AFM tip by dielectrophoresis.<sup>55</sup> This method consists in dipping an electrically contacted AFM tip into a solution full of NWs and in attracting nanowires into it through the application of an dc field through the tip. The

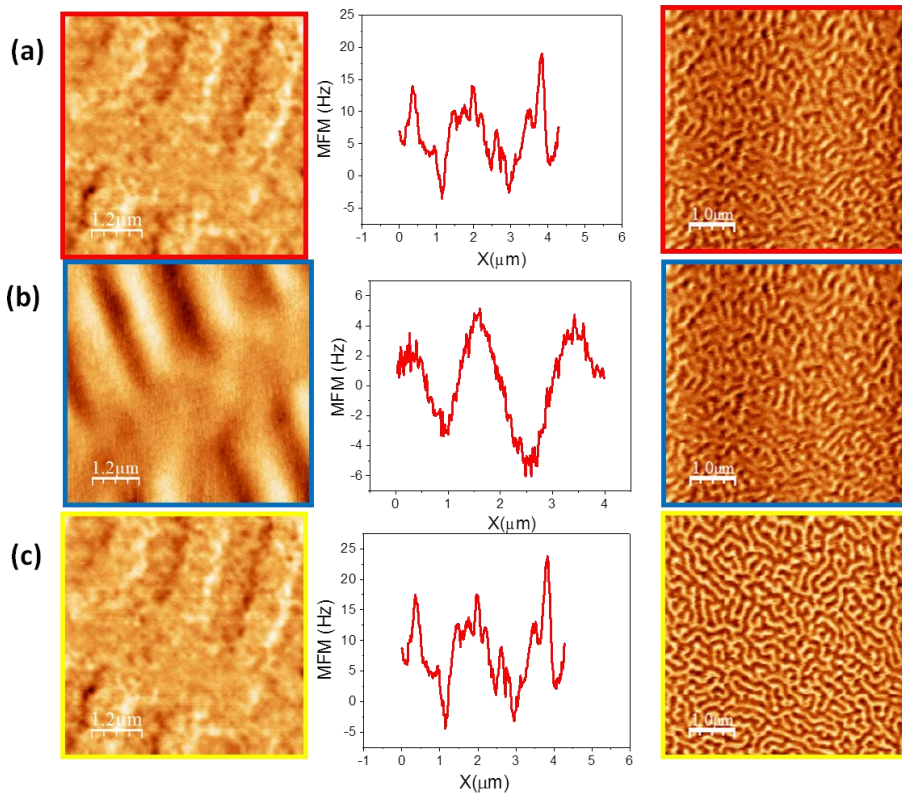
main drawbacks of this technique are associated to the lack of control of over the amount of nanowires that attach to the tip.

In an attempt to use magnetic nanowires as MFM probes, we tried to reproduce this last experiment. Nevertheless, when it was implemented in our laboratories, we found that the remains of the dissolved membrane introduced considerable dirt in the cantilever, up to hampering to reflect the laser signal necessary to operate the system.

An alternative approach was therefore conducted, based on the performance of force-distance curves on nanowires spread on a silicon substrate. Imaged performed on Hard Drive Disks (HDD), can be used as straightforward evidence to check that one or more nanowires are glued to tip, without further characterization. For a good interpretation of images, performing Scanning Electron Microscopy (SEM) measurements is advisable, to verify the position of the nanowires and the state of the edge utilized for the imaging.

The nanowires used for this part were made of either of pure Cobalt or of an iron cobalt copper alloy of 150nm of diameter. The magnetic configurations of these NWs are studied in detail in Chapters 3 and 4. Nevertheless, we advance without explaining further details that iron-cobalt-copper (FeCoCu) NWs present overall axial magnetization, while Co NWs tend to form vortices.<sup>56</sup>



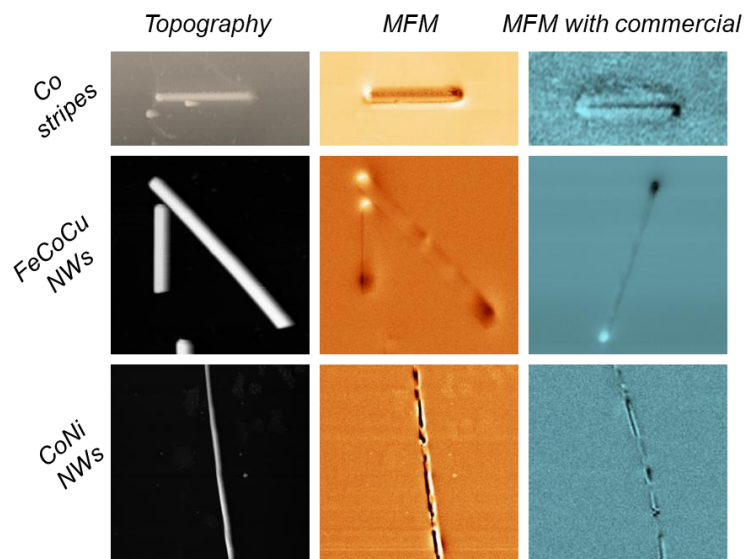


**Figure 2.13** MFM images of HD, corresponding profiles and images of a CoPt film with well-defined OOP magnetization. Images have been performed with (a) a MFM probe commercialized by Budget Sensors, (b) a FeCoCu NW and (c) a Co NW.

The choice of NWs with different magnetic configurations leads to important consequences in the resulting images. In Figure 2.13a, an image performed with a commercial MFM probe is compared to images obtained with hanging NWs. Images performed with commercial tips -which possess axial magnetization- are comparable to those obtained with the Co probe. Individual grains are visualized to a larger extent and narrower contrast is present in the poles. Nevertheless, measurements with Fe NWs shown in Figure 2.13b, look like typical images obtained with degraded tips. Subsequently, a CoPt thin film with well-defined OOP magnetization is imaged with the three tips. Again, the image obtained with tip with the Co NW displays the better resolution and sensitivity than FeCoCu. The high performance of the Co NW as a MFM probe is attributed to its magnetization configuration. Co nanowires develop a core-shell structure with multiple

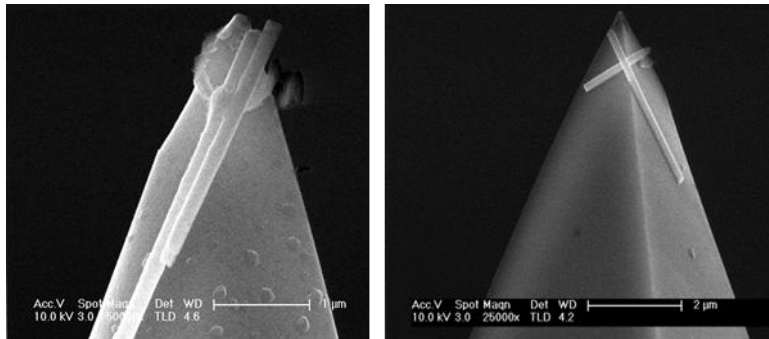
vortices in the shell and an axial core. This axial core is the source of OOP stray field and is responsible for the OOP domain imaging. Although the determination of the core size from XMCD-PEEM measurements is non-trivial, Bran et al. suggest that the size of the core in Co nanowires is very small compared to their diameter.<sup>56</sup>

Further examples are given below of images performed with NWs as the magnetic probes, which are useful not only for thin films of planar stripes, but we have also succeeded to measure cylindrical nanowires with complex configurations (Figure 2.14). The measurement conditions have been optimized for each particular tip.



**Figure 2.14** Examples of MFM images performed with different NWs on AFM tips, with compared MFM images made with commercial tips in blue scale.

However, the main drawback of this method is the lack of control over the NW position in the tip, in addition to picking more than one wire at the same time (Figure 2.15). Some challenges remain open, such as (i) the improvement of the ethanol solution that contains the NWs to succeed in the NW picking though electrophoresis and (ii) the functionalization of the NWs to improve their adhesion.



**Figure 2.15** Examples of magnetic nanowires stack onto commercial AFM probes.

### 3.5. Controlled approach: grown nanorods on AFM probes.

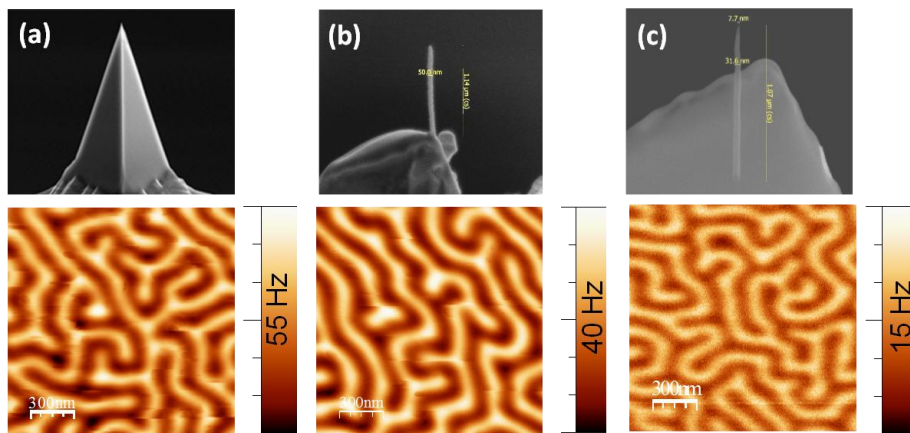
The use of NWs as active components in AFM tips, replacing the widespread coating method, has high potential in terms of quantification of data and improving the lateral resolution. Nevertheless, as we have seen, placing the nanowires in the right position of the tips is a difficult requirement to meet, and the ahead explained method lacks from reproducibility. Through Focus Electron Beam Induced Deposition (FEBID) nanorods of different materials can be fabricated<sup>57,58</sup> achieving high control over the nanorod position and material features in terms of crystallinity and phase, and remarkable control over geometrical parameters. Several examples can be found in the literature where grown nanorods are used as MFM probes.<sup>59,60</sup>

The stray field of these tips can be measured through EH and estimated by micromagnetic simulations. Currently, the development of probes with magnetic nanorods has extended its initial purpose of quantitative analysis of MFM measurement. In fact, the outstanding control over the growth of Co or Fe nanorods onto levers of different features has opened up additional opportunities to customize probes for samples who demand different measuring parameters.

Through a collaboration with the group of J.M. de Teresa, from the Instituto de Nanociencia de Aragón-, Fe nanorod (radius 30 nm and final radius below 7 nm) tip has been used which are of particular relevance in the Chapter 5 of this thesis, where the lowest possible interacting tip is required to evaluate the magnetic configuration of a soft sample. The sharp ending of these tips,

provide remarkable lateral resolution in samples with sizes lying close to the resolution limits.

In Figure 2.16, two different examples of grown iron nanowires are shown, together with the obtained MFM images of a reference CoPt thin film sample, with well-defined out-of-plane maze domains. They are compared to a commercial MFM tip from Nanosensors. Thicker nanowires possess comparable out-of-plane signal to commercial probes (Figure 2.16b), while thinner NWs do not produce “jumps” in the sample magnetization due to lower stray field (Figure 2.16).



**Figure 2.16** Comparison of the signal obtained with (a) a commercial probe, (b) a grown thick Fe nanorod and a (c) grown thin Fe nanorod on a CoPt out-of-plane reference sample, under the same working conditions.

In summary, growing nanorods on AFM tips is useful not only to perform quantitative analysis of the MFM images, but also obtain very sharp tips with good lateral resolution and small magnetic stray field to image magnetically soft samples. Besides, the shape of the nanorods permits to perform the second scan (retrace) closer from the surface since it exerts lower Van der Waals interaction. Although work on this research line is still in progress, outstanding results have been obtained in the previously introduced Biolever Mini. Measurements performed with Fe nanorods grown on low force constant microcantilevers happen to be surprisingly stable in air and water environments. A work reporting all these results is still in preparation.

## 4. Conclusions

Magnetic Force Microscopy constitutes a powerful imaging technique at the nanoscale that requires no exhaustive sample preparation, which can be performed in several environments and allows a dynamic study of the magnetization reversal process by *in-situ* field application, together with high resolution morphological mapping.

Coating AFM tips with a ferromagnetic material offers a wide range of options to design the right probe for an experiment: the lever feature can lead to higher or lower signal, the position of the coating enhances or smooths the stray field and the coating thickness can be selected according to the sample coercivity and magnetization values.

Cantilevers with low force constants are promising for measuring in liquids plus they can be helpful to enhance the signal to measure low interacting samples.

Magnetic nanowires attached to AFM tips are useful for measuring different samples and performing a quantitative analysis. Nanowires with different magnetic configurations can be sources of different output. The main drawback of this technique is the lack of controllability over the nanowire position, as compared to FEBID grown nanorods.

The combination of Magnetic Force Microscopy with micromagnetic simulations is highly recommended, in the study of three dimensional nanoobjects. Since MFM is mainly a surface imaging technique, different magnetic configurations might lead to similar MFM images, thus interpretation of images is not fully straightforward.

The following article has been sent for publication in relation with the work presented in this chapter:

- (1) Iglesias-Freire, Ó.; Jaafar, M.; Berganza, E.; Asenjo, A. Customized MFM probes with high lateral resolution. *Beilstein J. Nanotechnol.* **7**, 1068–1074 (2016).

## 5. References

1. Martin, Y. & Wickramasinghe, H. K. Magnetic imaging by 'force microscopy' with 1000Å resolution. *Appl. Phys. Lett.* **50**, 1455–1457 (1987).
2. Sáenz, J. J. *et al.* Observation of magnetic forces by the atomic force microscope. *J. Appl. Phys.* **62**, 4293–4295 (1987).
3. Binnig, G. & Quate, C. F. Atomic Force Microscope. *Phys. Rev. Lett.* **56**, 930–933 (1986).
4. Binnig, G. & Rohrer, H. Scanning tunneling microscopy. *Surf. Sci.* **126**, 236–244 (1982).
5. Wickramasinghe, H. K. Scanned-Probe Microscopes. *Scientific American* **261**, 98–105 (1989).
6. Betzig, E. & Chichester, R. J. Single molecules observed by near-field scanning optical microscopy. *Science* **262**, 1422–1425 (1993).
7. Horcas, I. *et al.* WSXM: A software for scanning probe microscopy and a tool for nanotechnology. *Rev. Sci. Instrum.* **78**, (2007).
8. No Title. Available at: <http://www.attocube.com/attomicroscopy/>.
9. No Title.
10. García, R. Dynamic atomic force microscopy methods. *Surf. Sci. Rep.* **47**, 197–301 (2002).
11. No Title. Available at: <http://www.nanophys.kth.se/>.
12. Martin, Y., Williams, C. C. & Wickramasinghe, H. K. Atomic force microscope-force mapping and profiling on a sub 100-Å scale. *J. Appl. Phys.* **61**, 4723–4729 (1987).
13. Albrecht, T. R., Grütter, P., Horne, D. & Rugar, D. Frequency modulation detection using high-Q cantilevers for enhanced force microscope sensitivity. *J. Appl. Phys.* **69**, 668–673 (1991).
14. Rodríguez, T. R. & García, R. Tip motion in amplitude modulation (tapping-mode) atomic-force microscopy: Comparison between continuous and point-mass models. *Appl. Phys. Lett.* **80**, 1646–1648 (2002).
15. Melcher, J., Hu, S. & Raman, A. Equivalent point-mass models of continuous atomic force microscope probes. *Appl. Phys. Lett.* **91**, (2007).
16. Martínez, N. F. *et al.* Bimodal atomic force microscopy imaging of isolated antibodies in air and liquids. *Nanotechnology* **19**, (2008).
17. Garcia, R. & Herruzo, E. T. The emergence of multifrequency force microscopy. *Nature Nanotechnology* **7**, 217–226 (2012).
18. Hosaka, S., Kikukawa, A., Honda, Y., Koyanagi, H. & Tanaka, S. Simultaneous observation of 3-dimensional magnetic stray field and surface structure using new force microscope. *Jpn. J. Appl. Phys.* **31**, L904–L907 (1992).
19. scixel. Available at: [http](http://).
20. Martínez-Martín, D., Jaafar, M., Pérez, R., Gómez-Herrero, J. & Asenjo, A. Upper bound for the magnetic force gradient in graphite. *Phys. Rev. Lett.* **105**, (2010).
21. Jaafar, M. *et al.* Variable-field magnetic force microscopy. *Ultramicroscopy* **109**, 693–

- 699 (2009).
22. Gómez-Navarro, C. *et al.* Scanning force microscopy three-dimensional modes applied to the study of the dielectric response of adsorbed DNA molecules. in *Nanotechnology* **13**, 314–317 (2002).
  23. Jaafar, M. *et al.* Hysteresis loops of individual Co nanostripes measured by magnetic force microscopy. *Nanoscale Res. Lett.* **6**, 1–6 (2011).
  24. Schwarz, A. & Wiesendanger, R. Magnetic sensitive force microscopy. *Nano Today* **3**, 28–39 (2008).
  25. Nonnenmacher, M., O'Boyle, M. P. & Wickramasinghe, H. K. Kelvin probe force microscopy. *Appl. Phys. Lett.* **58**, 2921–2923 (1991).
  26. Jaafar, M. *et al.* Distinguishing magnetic and electrostatic interactions by a Kelvin probe force microscopy–magnetic force microscopy combination. *Beilstein J. Nanotechnol.* **2**, 552–560 (2011).
  27. Jafaar, M. Procesos de imanacion en la nanoescala mediante microscopia de fuerzas magneticas . (Universidad Autonoma de Madrid, 2009).
  28. Iglesias-Freire, O. Advances in Magnetic Force Microscopy. (Universidad Autónoma de Madrid, 2014).
  29. Iglesias-Freire, Ó., Jaafar, M., Berganza, E. & Asenjo, A. Customized MFM probes with high lateral resolution. *Beilstein J. Nanotechnol.* **7**, 1068–1074 (2016).
  30. Panchal, V. *et al.* Calibration of multi-layered probes with low/high magnetic moments. *Sci. Rep.* **7**, (2017).
  31. Wren, T., Puttock, R., Gribkov, B., Vdovichev, S. & Kazakova, O. Switchable bi-stable multilayer magnetic probes for imaging of soft magnetic structures. *Ultramicroscopy* **179**, 41–46 (2017).
  32. Hartmann, U. Magnetic force microscopy: Some remarks from the micromagnetic point of view. *J. Appl. Phys.* **64**, 1561–1564 (1988).
  33. Tietze, R. *et al.* Magnetic nanoparticle-based drug delivery for cancer therapy. *Biochemical and Biophysical Research Communications* **468**, 463–470 (2015).
  34. Jaafar, M. *et al.* Structural insights into magnetic clusters grown inside virus capsids. *ACS Appl. Mater. Interfaces* **6**, 20936–20942 (2014).
  35. Giles, R. *et al.* Noncontact force microscopy in liquids. *Appl. Phys. Lett.* **63**, 617–618 (1993).
  36. Ares, P., Jaafar, M., Gil, A., Gómez-Herrero, J. & Asenjo, A. Magnetic Force Microscopy in Liquids. *Small* **11**, 4731–4736 (2015).
  37. Dietz, C., Herruzo, E. T., Lozano, J. R. & Garcia, R. Nanomechanical coupling enables detection and imaging of 5 nm superparamagnetic particles in liquid. *Nanotechnology* **22**, (2011).
  38. Baclayon, M., Wuite, G. J. L. & Roos, W. H. Imaging and manipulation of single viruses by atomic force microscopy. *Soft Matter* **6**, 5273 (2010).
  39. Kuznetsov, Y. G. & McPherson, A. Atomic Force Microscopy in Imaging of Viruses and Virus-Infected Cells. *Microbiol. Mol. Biol. Rev.* **75**, 268–285 (2011).
  40. Hansma, P. K. *et al.* Tapping mode atomic force microscopy in liquids. *Appl. Phys. Lett.* **64**, 1738–1740 (1994).



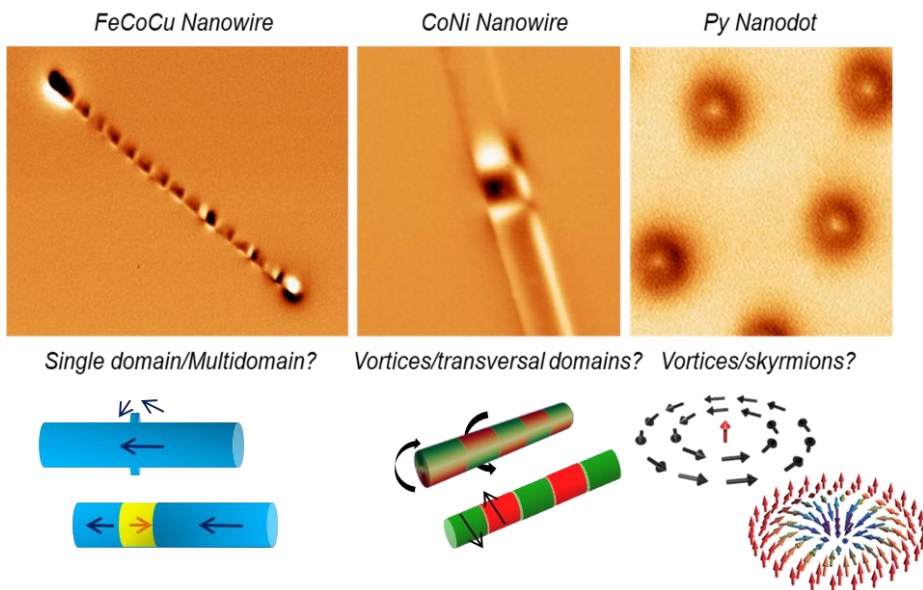
41. Meng, X. *et al.* Broad modulus range nanomechanical mapping by magnetic-drive soft probes. *Nat. Commun.* **8**, (2017).
42. No Title. Available at: <http://www.nanosensors.com/>.
43. N. Available at: <http://www.team-nanotec.de/>.
44. No. Available at: <https://www.spmtips.com/>.
45. No Title.
46. Jaafar, M. *et al.* Drive-amplitude-modulation atomic force microscopy: From vacuum to liquids. *Beilstein J. Nanotechnol.* **3**, 336–344 (2012).
47. Faivre, D. & Schüler, D. Magnetotactic bacteria and magnetosomes. *Chem. Rev.* **108**, 4875–4898 (2008).
48. Fdez-Gubieda, M. L. *et al.* Magnetite biomineralization in magnetospirillum gryphiswaldense: Time-resolved magnetic and structural studies. *ACS Nano* **7**, 3297–3305 (2013).
49. Winkler, A. *et al.* Magnetic force microscopy sensors using iron-filled carbon nanotubes. *J. Appl. Phys.* **99**, 104905 (2006).
50. García Roman, E. L., Martínez orellana, L., Díaz Lagos, M. & Huttel, Y. Modification of atomic force microscopy tips by deposition of nanoparticles with an aggregate source. **1**, 1–12 (2013).
51. García, J. M. *et al.* Quantitative interpretation of magnetic force microscopy images from soft patterned elements. *Appl. Phys. Lett.* **79**, 656–658 (2001).
52. Vock, S. *et al.* Monopolelike probes for quantitative magnetic force microscopy: Calibration and application. *Appl. Phys. Lett.* **97**, (2010).
53. García, J. M., Thiaville, A. & Miltat, J. MFM imaging of nanowires and elongated patterned elements. in *Journal of Magnetism and Magnetic Materials* **249**, 163–169 (2002).
54. García-Martín, J. M. *et al.* Imaging magnetic vortices by magnetic force microscopy: Experiments and modelling. *J. Phys. D. Appl. Phys.* **37**, 965–972 (2004).
55. Yang, G. *et al.* Magnetic nanowire based high resolution magnetic force microscope probes. *Appl. Phys. Lett.* **87**, 1–3 (2005).
56. Bran, C. *et al.* Spin configuration of cylindrical bamboo-like magnetic nanowires. *J. Mater. Chem. C* **4**, 978–984 (2016).
57. Pablo-Navarro, J., Magén, C. & De Teresa, J. M. Three-dimensional core-shell ferromagnetic nanowires grown by focused electron beam induced deposition. *Nanotechnology* **27**, (2016).
58. Pablo-Navarro, J., Magén, C. & de Teresa, J. M. Purified and Crystalline Three-Dimensional Electron-Beam-Induced Deposits: The Successful Case of Cobalt for High-Performance Magnetic Nanowires. *ACS Appl. Nano Mater.* acsanm.7b00016 (2018). doi:10.1021/acsanm.7b00016
59. Gavagnin, M. *et al.* Free-standing magnetic nanopillars for 3D nanomagnet logic. *ACS Appl. Mater. Interfaces* **6**, 20254–20260 (2014).
60. Utke, I., Hoffmann, P., Berger, R. & Scandella, L. High-resolution magnetic Co supertips grown by a focused electron beam. *Appl. Phys. Lett.* **80**, 4792–4794 (2002).



## APPENDIX A: Micromagnetic simulations, a complementary tool for the interpretation of MFM images.

Many of the experiments carried out along this thesis have been supported by micromagnetic simulations. It is important to recall that MFM was conceived to study planar samples, since it is mainly sensitive to superficial charges. Thus, simulations are a good way to complement MFM imaging analysis of 3 dimensional objects.

The MFM user needs to be aware that for nanostructures with complex magnetic configurations – nanowires with core-shell magnetization distribution, for instance, the MFM images do not provide complete information to determine the domain configuration. Figure A.1 collects some examples of complex magnetization distributions that can lead to a similar MFM images.



**Figure A.1** Examples of MFM images compatible with more than one magnetic configuration.

Micromagnetic simulations can be carried out by different Micromagnetic packaged which numerically integrate the set of ordinary differential equations given by the Landau-Lifshitz and Gilbert equation over time.

The two methods that are most widely spread in micromagnetic modelling are the so-called finite difference and the finite element methods. They differ in the spatial discretization of the defined geometry. While the finite difference approach subdivides the space into small cubes or cells, the finite element approach does it typically in tetrahedra. Both have their assets and drawbacks.

In this thesis, the open source widely used code Object Oriented MicroMagnetic Framework (OOMMF) package based on finite difference was applied for modelling. Finite difference approaches possess an error associated with the staircase discretization, although this can be reduced by choosing a small discretization size. On the other hand, finite difference packages require less computer memory (RAM).

### A.1. Landau-Lifshitz-Gilbert Equation

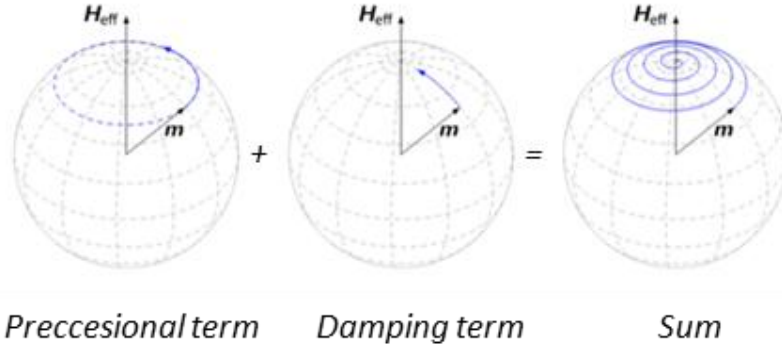
In micromagnetism, the magnetization dynamics are given by the Landau-Lifshitz-Gilbert (LLG) equation. This is a differential equation solved by micromagnetic simulation software that describes the precession of the magnetic moment around an effective magnetic field vector. In 1935, Landau and Lifshitz proposed the first dynamical model for the precessional motion of the magnetization. The equation is given by

$$\frac{d\mathbf{M}}{dt} = \gamma\mu_0\mathbf{M} \times \mathbf{H} \quad (32)$$

where  $\gamma$  is the gyromagnetic ratio and  $\mu_0$  is the vacuum permeability. They introduced an additional term to the equation describing phenomenologically the damping (dissipative) effect

$$\frac{d\mathbf{M}}{dt} = \gamma\mathbf{M} \times \mathbf{H}_{eff} - \frac{\lambda}{M_s}\mathbf{M} \times (\mathbf{M} \times \mathbf{H}_{eff}), \quad (33)$$

where  $\lambda$  is a phenomenological constant characteristic of each material. Figure 2.18 schematically describes the two terms of the equation of motion.



**Figure A.2** Time evolution of the magnetic moment  $\mathbf{m}$  around an effective field  $\mathbf{H}_{\text{eff}}$ . The motion can be separated into a precessional term and a damping term. Adapted from [ref<sup>1</sup>].

Years later, in 1955, Gilbert derived the precessional motion equation (31) from the Lagrangean formulation and described the dissipative term as originated owing to a viscous force proportional to the derivatives of the magnetization components.

$$\frac{\partial \mathbf{M}}{\partial t} = -\gamma \mathbf{M} \times \mathbf{H}_{\text{eff}} + \frac{\alpha}{M_s} \mathbf{M} \times \frac{\partial \mathbf{M}}{\partial t} \quad (34)$$

where  $\alpha$  is the Gilbert damping constant. Assuming that

$$\gamma_L = \frac{\gamma}{1+\alpha^2} \text{ and } \lambda = \frac{\gamma \alpha}{1+\alpha^2} \text{ LL and LLG equations are equivalent.}$$

## A.2. Micromagnetic assumptions

Several models exist to describe ferromagnetic materials. Despite being magnetism of quantum mechanical origin, micromagnetic theory has proven to be a reliable tool in certain length scales (see table below). In contrast to domain theory it is able to resolve the inner structure of domain walls.

Micromagnetism assumes that magnets are mesoscopic continuous mediums where atomic-scale structure can be ignored:  $\mathbf{M}(\mathbf{r})$  and  $\mathbf{H}_d(\mathbf{r})$  are time dependent, non-uniform, continuously varying functions of fixed spontaneous magnetization  $\mathbf{M}_s$  that fulfill the condition:

$$\mathbf{M}(\mathbf{r}) = M_s \cdot \mathbf{m}(\mathbf{r}); \quad |\mathbf{m}(\mathbf{r})| = 1$$

Considering the simplifications introduced by the micromagnetic theory, one needs to evaluate if the model is valid for a specific problem. For instance, given that the micromagnetic approach considers homogeneous magnetization, it presents some limitation to describe singularities. The only stable singular structure in a ferromagnet is the Bloch Point (BP). In a closed surface, surrounding the point, the magnetization vectors on this surface cover the surface of the unit sphere exactly once. This definition implies that the modulus of the magnetization must vanish at the BP center, so that micromagnetism does not apply in this region. However, it was demonstrated by Thiaville et al. that micromagnetic calculations allow the presence of BP between meshes, although they underestimate their energy.<sup>2</sup>

Temperature effects are another example of the limitations of this model. They can be described as perturbations of single magnetic moments, which disagrees with the homogeneous magnetization assumption. For OOMMF users, several extensions can be found where thermal fluctuation effects are modelled,<sup>3</sup> transforming the standard LLG equation to a stochastic differential equation.<sup>4</sup> OOMMF gives, additionally, the option of choosing an initial random configuration according to a specified random seed value. This is an easy way to reach different energy minimum configurations, avoiding the non-stochastic nature of the software.

Similarly, additional extensions have been created to simulate spin-polarized currents,<sup>5</sup> which are not otherwise considered.

Finally, many times the micromagnetic user fails to find an agreement between modelling output and experimental results due to the absence of defects amongst the simulation specifications. There are several ways in which defects can be introduced in simulations, such as the inclusion of small non-magnetic areas amongst the ferromagnetic areas, small changes in the anisotropy axis along the geometry, etc.

## References

1. <http://micromagnetics.org/>.
2. Thiaville, A., García, J. M., Dittrich, R., Miltat, J. & Schrefl, T. Micromagnetic study of Bloch-point-mediated vortex core reversal. *Phys. Rev. B - Condens. Matter Mater. Phys.* **67**, (2003).
3. [http://www.nanoscience.de/group\\_r/stm-spstm/projects/temperature/download.shtml](http://www.nanoscience.de/group_r/stm-spstm/projects/temperature/download.shtml).
4. Lyberatos, A., Berkov, D. V. & Chantrell, R. W. A method for the numerical simulation of the thermal magnetization fluctuations in micromagnetics. *J. Phys. Condens. Matter* **5**, 8911–8920 (1993).
5. Zhang, S. & Li, Z. Roles of nonequilibrium conduction electrons on the magnetization dynamics of ferromagnets. *Phys. Rev. Lett.* **93**, (2004).





## **CHAPTER 3:**

# **Domain wall pinning in magnetic nanowires**

Since in 2008 Parkin et al., launched the concept of the so-called racetrack memory,<sup>1</sup> many groups have deepened the investigation of magnetic domain-wall pinning mechanisms in planar nanostripes.<sup>2,3</sup> Generally, the realization of spintronic based devices relies on the fabrication of optimal stripes/nanowires with well-defined pinning sites, where the magnetization reversal can be induced by spin-polarized current through a step-by-step domain wall motion. In fact, domain walls are considered to behave as quasi particles<sup>4</sup> that can be manipulated by magnetic fields,<sup>5</sup> spin polarized currents<sup>6</sup> or pinning potentials induced by geometrical changes in the nanostructures.<sup>3</sup> In materials with weak magnetocrystalline anisotropy, patterned notches<sup>7</sup> or antinotches<sup>8</sup> are expected to modify the energy landscape and create different energy barriers for the domain wall propagation.

However, it was found that individual cylindrical<sup>9,10</sup> nanowires present some features that make them more convenient for applications, such as not showing a Walker breakdown,<sup>11,12</sup> an effect that limits the DW propagation speed at high external fields. Besides, their cylindrical geometry favors the development of vortex domain walls that move uniformly,<sup>13</sup> contrary to the transverse domain walls extensively studied in two dimensional structures.

Several ways have been proposed in the literature to control DW pinning in cylindrical nanowires. Analogously to notches in planar structures, introducing changes in the diameter has been an extensively explored way on the attempt to create pinning sites.<sup>14,15</sup> On the other hand, chemical electrodeposition gives the chance of growing consecutive segments of different materials, which is an alternative approach to pin domain walls at the interfaces.<sup>16</sup>

The aim of this chapter is the study of two different mechanisms to control the magnetization reversal in nanowires with axial magnetization. During his PhD thesis, Dr. O. Iglesias-Freire –a former member of the Magnetic Force Microscopy group- carried out some preliminary work on the study pinning mechanisms in bamboo-like nanowires of smaller diameter,<sup>17,18</sup> showing that it is necessary to work on thicker nanowires to achieve higher control on the crystalline structure and surface roughness.

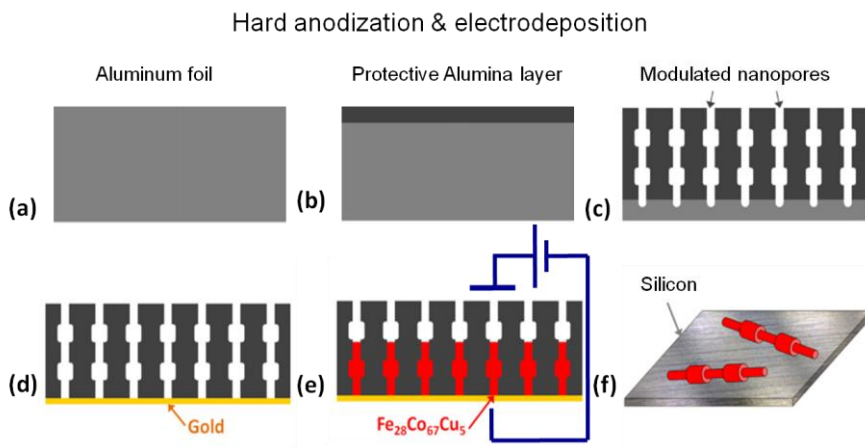
Hereafter, an extensive study has been performed in what we have called *bamboo-like* nanowires, cylindrical nanowires with periodically grown

antinotches, that lead to a publication<sup>19</sup> in 2016. After this, some alternatives approaches to pin DW are presented and discussed.

## 1. Sample preparation

### 1.1. Fabrication of nanowires through electrodeposition

All the magnetic nanowires studied along this thesis have been grown by Dr. C. Bran –member of the group of Nanomagnetism and Magnetization Reversal Processes of the ICM- through chemical electrodeposition into alumina porous membranes (see Figure 3.1). This is a commonly used method to grow cylindrical nanowires<sup>20,21</sup> due to its low cost and high fabrication yield, compared to lithography based techniques. The alumina membranes serve as a mold to subsequently grow the nanowires, i.e. it is a key step to define a straight geometry –choosing the pore diameter-, or on the contrary, to create little geometrical variations. To grow nanowires whose diameter is in the range between 100-150nm, anodic alumina oxide (AAO) membranes are synthesized by pulsed hard anodization, depending on the desired modulation type.<sup>14</sup> Prior to the pore growth, a pre-anodization is performed to grow a protective layer. The geometry of the pores and the interpore distance is controlled by the anodization time, voltage, temperature and pH of the bath.



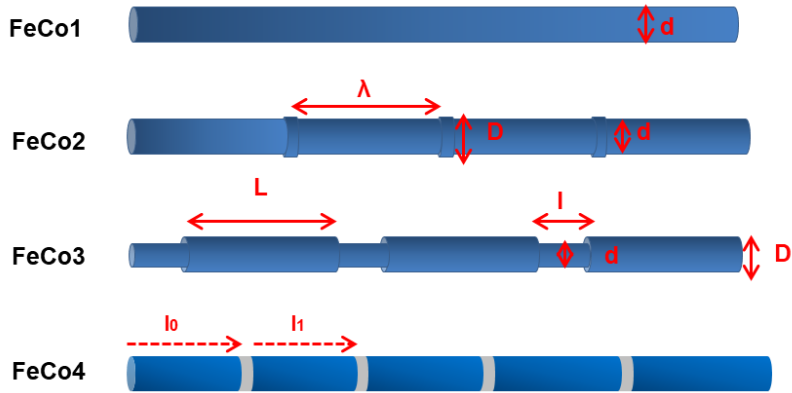
**Figure 3.1** Growth of modulated nanowires. (a) Beginning from an aluminum foil (b) a protective alumina is grown through a pre-anodization. (c) Modulated pores are grown through pulsed anodization. (d) After the removal of the aluminum foil a gold electrode is sputtered for the (e) potentiostatic electrodeposition. (f) Finally NWs are deposited onto a Silicon substrate for their individual study. Adapted from [ref.17].

The template to grow FeCo based nanowires was obtained by pulsed hard anodization<sup>15,22</sup> in oxalic aqueous<sup>23</sup> solution (0.3M) containing 5 vol.% ethanol at a constant temperature of 0 °C. In a first step a constant voltage of 80 V was applied for 900s to produce a protective aluminum oxide layer at the surface of the disc, which avoids breaking or burning effects during subsequent hard-pulse anodization. The voltage is slowly increased (0.08 V/s) to 140 V and kept constant for 600 s, which ensures the parallel alignment of the nanochannels.

The composition of the NWs alloy is Fe<sub>28</sub>Co<sub>67</sub>Cu<sub>5</sub> (hereafter referred to as the FeCoCu nanowires), as determined by Energy Dispersive Spectroscopy (EDS). After electrodeposition, the nanowires are released from the alumina membrane using a mixed solution of CrO<sub>3</sub> and H<sub>3</sub>PO<sub>4</sub>. The membrane is dissolved and the nanowires need to be cleaned in ethanol, before they are spread onto a substrate. For the individual study of the nanowires with MFM, a protocol for the nanowire preparation onto the substrate has been developed, which is detailed in Appendix 1.

## **1.2. Approaches to control the Domain Wall pinning**

In this chapter, four types of samples of similar composition Fe<sub>28</sub>Co<sub>67</sub>Cu<sub>5</sub> are presented, where different strategies have been adopted to accomplish pinning of the domain walls at specific geometrical positions (see Figure 3.2). A sample with constant diameter and composition (FeCo1) has been grown for comparison. The main features of all samples are gathered in Table 3.1. In all cases, the composition has been chosen due its weak magnetocrystalline anisotropy. Additionally, regarding practical applications, its high Curie temperature allows operating in a wide temperature range.



**Figure 3.2** Schematic representation of the four types of NWs studied along this chapter.

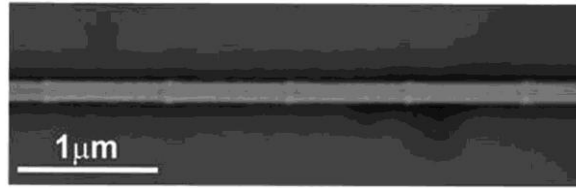
Sample	FeCo1	FeCo2	FeCo3	FeCo4
Geometrical features	Straight	Bamboo-like	Modulated	Multisegmented
Parameters	$d=150\text{nm}$	$\lambda=0.8\ \mu\text{m}$ $d=150\text{nm}$ $D=170\text{nm}$	$L=1\ \mu\text{m}$ $l=0.4\ \mu\text{m}$ $d=110\text{nm}$ $D=140\text{nm}$	$d_i(x) = d_{i-1} + 30\text{nm}$ $L_{\text{Cu}} = 30\text{nm}$
Average length	$12\ \mu\text{m}$	$12\ \mu\text{m}$	$12\ \mu\text{m}$	$20\ \mu\text{m}$

**Table 3.1** Types of nanowires used in this chapter.

## 2. *Bamboo-like* nanowires

The modulated nanopores of the template to grow *bamboo-like* nanowires (FeCo2) were produced by periodically applying pulses of 140 V and 80 V for 30 and 10 s, respectively. The pulses were repeated 30 times to guarantee a total length of the modulated pores of few tens of microns.

Thus, nanowires with very high aspect ratio were grown by electrodeposition into the template with an average length of  $12\ \mu\text{m}$ , displaying a bamboo-like structure with a periodicity of 800 nm and diameters of about 150 nm (segment) and 170 nm (modulation), respectively (See Figure. 3.3).

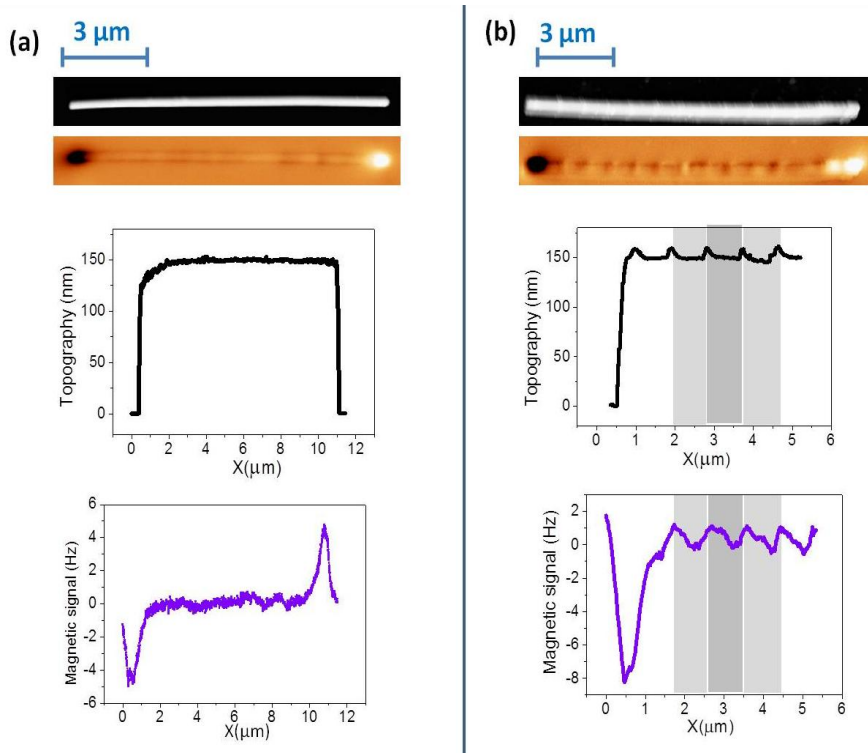


**Figure 3.3** SEM image of a nanowire showing bamboo-like diameter modulation.

### **2.1. Effect of the modulation on the spin configuration.**

Homogeneous (FeCo1) and bamboo-like NWs (FeCo2) with similar length were studied. The nanowires of constant diameter were used as a reference to evaluate the effect of the diameter modulation. A few tens of homogeneous and bamboo-like NWs were imaged in remanence after ac demagnetization. In most of the cases, images like those shown in Figure 3.4 are observed. The magnetic image in Figure 3.4a corresponds to the homogeneous diameter nanowire, where the dark and bright contrasts at the ends of the NW are the main noticeable features. That leads us to conclude its single domain configuration.

However, the MFM image in Figure 3.4b corresponding to the bamboo-like NW (FeCo2), displays the same dark and bright contrast at the ends plus additional, less intense, periodic contrasts along the wire. The comparison amongst magnetic and topographic images demonstrates the correlation between the periodic modulations in the diameter and the features in the MFM contrast.

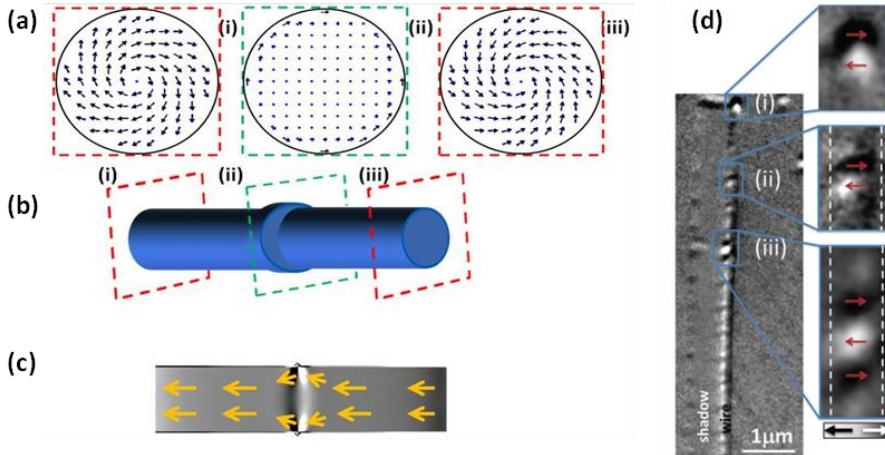


**Figure 3.4** Topographic and MFM images of (a) a NW with homogeneous diameter (FeCo1) showing a single domain configuration and (b) a bamboo-like NW (FeCo2) where the local modulations produce small divergences of the magnetization. Profiles along the main axis were performed in both NWs (only left part of the bamboo-like NW is shown for clarity purposes).

Simulations performed with OOMMF show overall axial magnetization and two equal vortices appearing at both edges of the NW (i) and (iii) (see Figure 3.5). However, at the position with enlarged diameter (ii) a pseudo-vortex with a large core is expected. Notice that the MFM is hardly sensitive to this pseudo-vortex due to the lack of stray field. Nevertheless, the bright and dark contrasts along the NW axis are induced by the weak stray field close to the modulation (as shown in the sketch in Figure 3.5). The presence of the ahead explained vortices was later experimentally confirmed by XMCD measurements in the CIRCE beam of the Alba Synchrotron, in collaboration with Dr. L. Aballe, Dr. M. Foester and Dr. A. Fraile Rodriguez. As it was pointed out in Chapter 1, where different magnetic domain imaging techniques are compared, XMDC possesses the capacity of imaging the inner magnetization configuration of nanostructures, in contrast to MFM which is



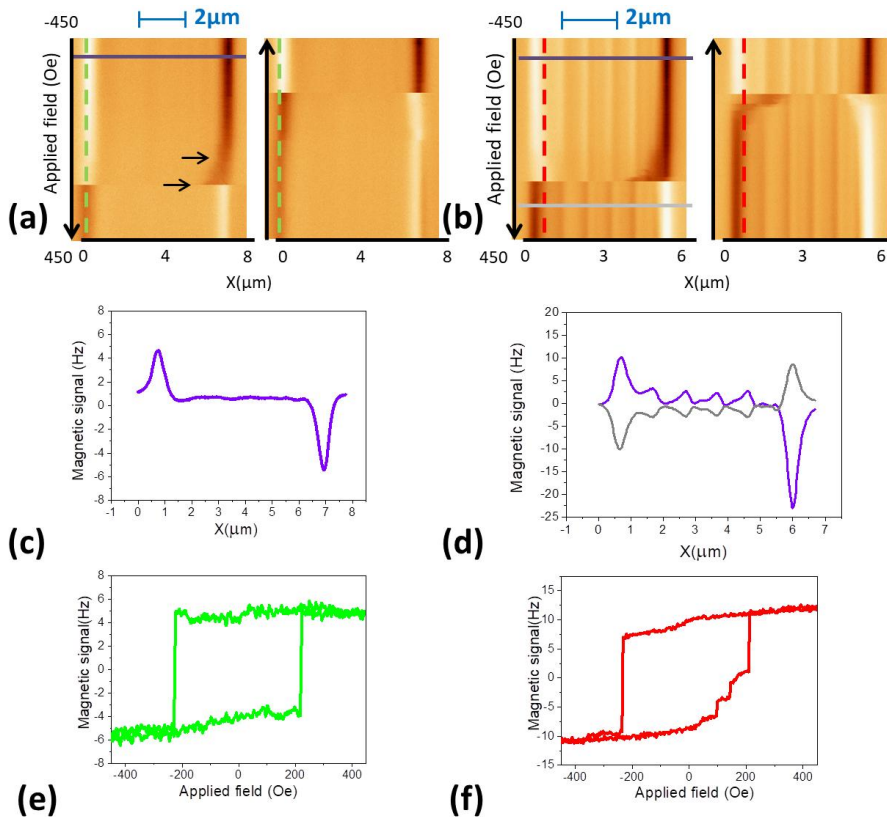
mainly surface stray field sensitive. In the inset of Figure 3.5d, white-dark contrasts demonstrate the formation of vortices at certain positions, as predicted by simulations.



**Figure 3.5** Micromagnetic simulations of the spin configuration of a modulated NW calculated by OOMMF: different vortex configurations (a) appear along the NW (i), (ii) and (iii). (b) Sketch of the simulated nanowire. (c) In a section along the wire, magnetization divergence plus some arrows indicating the magnetization direction are depicted. (d) Experimental evidence (XMCD image) of vortex formation.

## 2.2. Vortex mediated magnetization reversal

Magnetization reversal processes in both straight and bamboo nanowires were investigated by using a non-standard MFM technique<sup>24</sup> already explained in section 2.2 of Chapter 2. In modulated NWs, the in-plane magnetic fields available in our set-up, applied parallel to the main axis of the NWs, are not high enough to reach the magnetic saturation but are sufficient to reverse their magnetization. Figure 3.6a and b show the evolution of the magnetic contrast under *in-situ* applied magnetic fields for NWs with homogeneous and modulated diameter, respectively. For high magnetic fields, the homogeneous NW is saturated and thus the MFM signal exhibits the so called dipolar contrast (see the profile shown in Figure 3.6a measured along the solid purple line). As the field is swept, the bright/dark contrast at the ends of the NW decreases gradually due to the reduction of the magnetostatic interaction between the tip and the sample



**Figure 3.6** Non-standard MFM based image of nanowires (a) with homogeneous diameter and (b) bamboo-like geometry. (a) Two critical fields have been marked with arrows. (b) In the bamboo-like nanowires, a DW propagated towards the opposite end, jumping from one pinning site to the next. (c) Profile measured along the solid line in (a). (d) Profiles measured along the purple and gray lines marked in (b). Based on these images, non-conventional hysteresis loops of (e) homogeneous and (f) bamboo-like nanowires were depicted corresponding to the dashed lines in (a) and (b).

Presumably, vortices are developed at the ends of the nanowires as the field goes down and they propagate when the coercive field is reached spreading an opposite magnetization domain -as predicted for NWs with diameters beyond a few tens of nanometers.<sup>10</sup>

In Figure 3.6e the evolution of the contrast in one ends of the NW is depicted. MFM data in Figure 3.6a and 3.6d suggest a bistable behavior where either positive or negative remnant configuration is possible. Notice that, in principle, DWs can nucleate simultaneously in both ends. However, the local geometry of each particular NW determines whether one or two DWs are involved in the magnetization reversal.<sup>25</sup> Slight differences in the

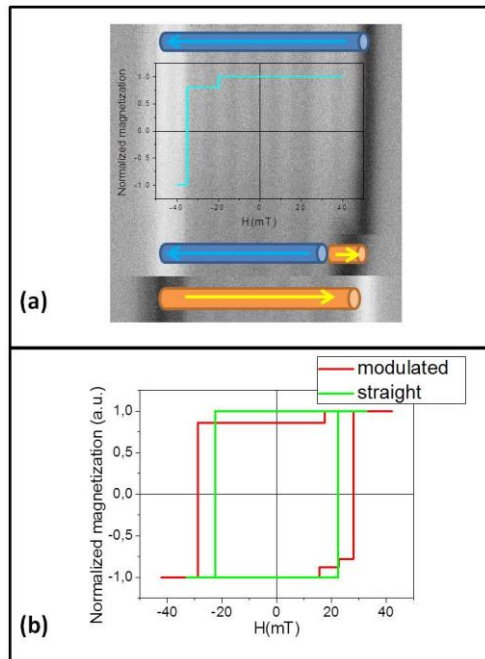
critical fields between different nanowires are expected due to small morphological differences amongst them.

Unlike homogeneous nanowires, the measurements corresponding to bamboo NWs outstandingly show the intermediate pinning of the DW in specific diameter modulation sites near the ends of the NW (see the evolution of the dark contrast in the image corresponding to the branch from + 450 to - 450 Oe in Figure 3.6b). It should be noticed that the contrast at the enlarged diameter regions remains even at the highest applied field (see Figure 3.6b). At a critical field, a DW depins and propagates along the NW. At the diameter modulations the MFM contrast is reversed as the DW passes through, in good agreement with the micromagnetic simulations presented above. In the following image -corresponding to the branch from - 450 to + 450 Oe-, we observe even more clearly that the DW stops in two identified modulated sites giving rise to small jumps in the hysteresis loop until finally reaching the far end of the NW.

Since the driven parameter, the magnetic field, is sweeping continuously, after the first depinning, the applied magnetic field is much higher than the critical field i.e. the domain wall speed increases.<sup>26,27</sup> The pinning at intermediate sites are metastable configurations. Small variations in the DW propagation and asymmetries are measured in successive field cycling for the same nanowire which evidences how critical the data acquisition speed might be in these measurements. We must keep in mind that the scanning speed of the MFM is around 100 microns per second, much smaller than the propagation velocity.

The normalized hysteresis loops of the FeCo<sub>2</sub> NW -shown in Figure 3.6f- were obtained from the MFM image in Figure 3.6b. However bamboo-like NWs present several intermediate configurations and therefore, the data from one of the NW ends is not representative of the whole NW. To obtain a conventional hysteresis loop a reconstruction procedure is needed. By using these results, we have calculated an average hysteresis loop for the modulated NW (Figure 3.7) that allows us to give an average coercive value of 250 Oe.<sup>14</sup>

### **2.2.1. Reconstruction of the hysteresis loop of a single NW**



**Figure 3.7** (a) The normalized magnetization is calculated for each configuration using geometrical considerations. (b) Reconstructed hysteresis loops for both kinds of nanowires.

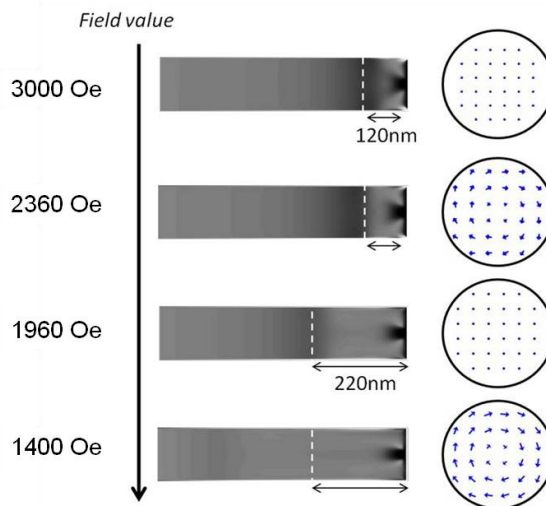
We have evaluated the changes of the magnetic moment along the axis associated to the jumps as shown in the Figure 3.6a. In this simple model the initial and final magnetization values are considered -1 and 1 respectively, and the values from the configurations in between are calculated from purely geometrical considerations.

The hysteresis loops obtained when we plot the profiles obtained from the MFM data are similar to the conventional hysteresis loops which quantify the magnetization in the NW axis as a function of the applied field. Nevertheless, we have to keep in mind that MFM is sensitive to the stray field of the sample, in the out of plane direction. This means that, especially in the case of the diameter modulated NWs, although the hysteresis curves might seem similar to the conventional, the size of the Barkhausen jumps is not real. Further calculus need to be performed, since a single profile at the edge gives only information of the local changes in the magnetization.

On another note, the decrease of contrast intensity in the ends of the NWs as the magnetic field is swept (for instance Figure 3.6a), can be understood

through micromagnetic simulations. Beginning from a saturated configuration, spin configurations were recorded for different stages while the field was being lowered. The divergence of the magnetization – comparable to the MFM data- was calculated with the software and it was represented in a gray scale. In the figure below, a transversal slice through the middle of the cylinder is shown. As it can be seen in Figure 3.8, a vortex which nucleates right after losing saturation by decreasing the field expands towards the center of the NW. Notice that, the spin configuration is shown in the right gives as an idea of the extension of the vortex for each stage.

This effect can be detected by advanced MFM modes as a decrease in the intensity of the signal (frequency shift), since MFM is a surface technique with high magnetic sensitivity. Nonetheless, the growth of the vortex is not detected in terms of lateral growth until it becomes very notable, due to the limitations in spatial resolution.



**Figure 3.8** Sequence showing the dynamical evolution of the vortex nucleated at one end of the NW. A piece of 500 nm has been represented.

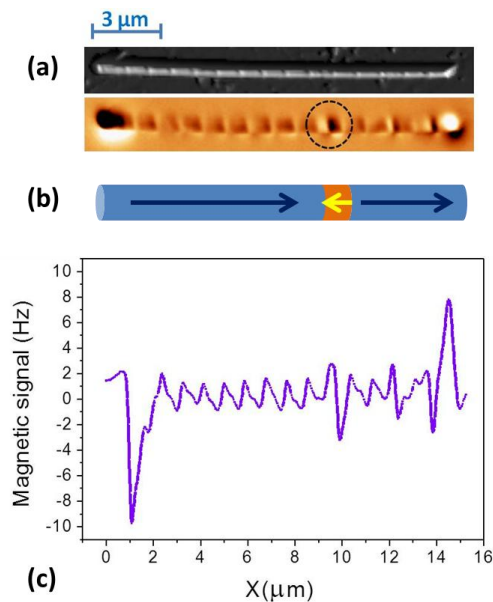
It is therefore concluded from the simulations that a vortex nucleates at one of the ends, right after the fields acquires a value below its saturation field; this vortex nucleates and grows in thickness, expanding towards the center.

In the straight NWs, magnetization at the surface switches first followed by the core. This explanation is in good agreement with the experimental data

shown in Figure 3.6. At a certain value of the field, the magnetic contrast at the nanowire end is suddenly reversed when the closure structure becomes energetically unstable; a domain nucleates, the domain wall is depinned and propagates along the NW length resulting in a single large Barkhausen jump. A recent publication<sup>28</sup> unveils that the shell reverses in the first place, giving rise to the creation of a skyrmion tube, until the core reverses. Therefore, we can distinguish two critical values: (i) the first one, corresponds to the region where we are able to measure the enlargement of the vortex; (ii) the second one, where we see a single Barkhausen jump without intermediate configuration due to the quick propagation of the domain wall, around 6 orders of magnitude beyond the scanning speed. Both have been marked with arrows in Figure 3.6a.

### 2.3. Domain Wall pinning

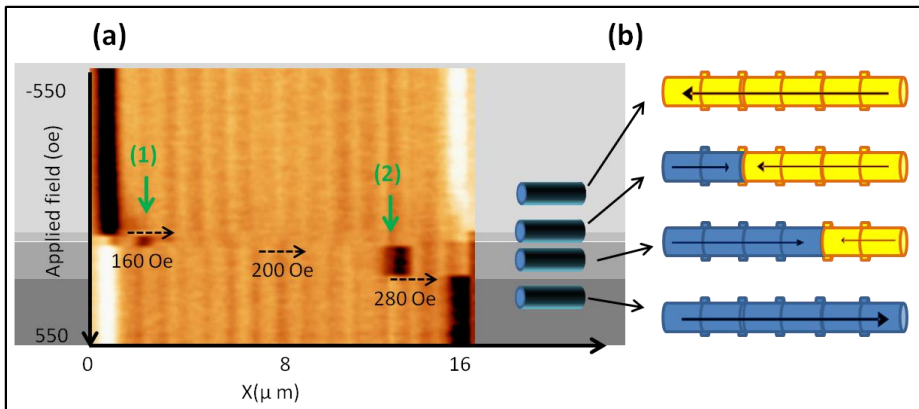
Although the configurations shown so far are the most usual, we have also found different behaviors. Around 30% of the measured NWs present high contrast (bright and dark) spots as the one displayed in the MFM image in Figure 3.9(a). They have been identified in positions that match with enlarged diameter regions along the NW (marked with a circle).



**Figure 3.9** Nanowire with several strong black-white contrasts in the positions of enlarged diameter.

However, their corresponding topographic images show that there are no obvious morphological differences between the spots that present higher contrast. Despite not being energetically favorable, such strong contrast could be eventually interpreted as originated by a small domain with the magnetization opposite to the main nanowire magnetization, such as in Figure 3.9b. Nevertheless, most of the bamboo-like nanowires present MFM images that are compatible with single domain configuration with a periodic local spin divergence induced at the sites of increased diameter. To obtain deeper insight into the magnetic configuration and their evolution under applied magnetic field, non-standard VF-MFM measurements were performed on several NWs displaying one or more strong contrasts in the middle.

In some cases, it was proven not only that a DW is pinned, but we even succeeded to move the position of the domain wall from one pinning site to another, as in Figure 3.10.

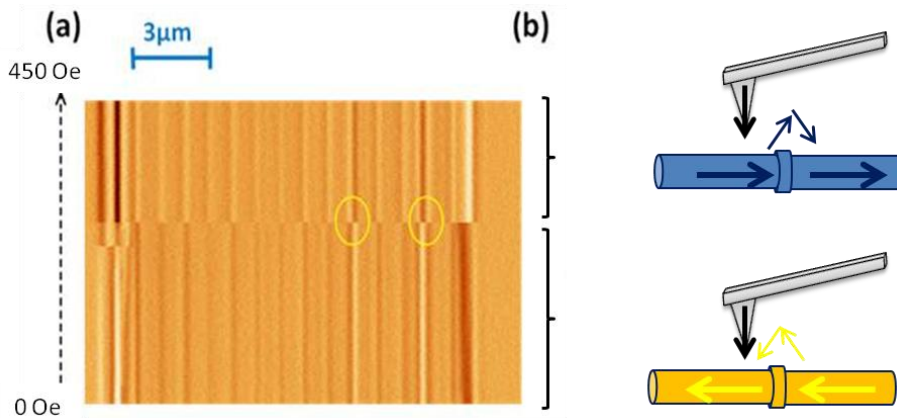


**Figure 3.10** (a) Non-standard MFM image of a NW where a DW is pinned. The DW “jumps” from one modulation to another under the externally applied magnetic field. The sketches in (b) illustrate the four different configurations observed in the MFM measurement.

The magnetic field was swept between  $\pm 700$  Oe although here only the region from  $-550$  to  $550$  Oe is shown. In the image shown in Figure 3.10, we observed the pinning of domain walls in different regions of the NW and at different magnetic fields. A segment on the left side begins their magnetization reversal at  $160$  Oe, moreover, at  $200$  Oe the domain wall jumps to the right and finally, the reversal of the whole nanowire does not

occur until 280 Oe magnetic field is applied. Notice that, as expected, this NW presents slightly magnetically harder behavior than the NW shown in Figure 3.6b.

However, more commonly, the presence of strong contrasts along the nanowires can sometimes be misleading, since it does not necessarily manifest the existence of a pinned domain wall, as in the case of the data presented in figure 3.11.



**Figure 3.11** (a) Non-standard MFM image of a NW which seems to have a pinned DW in its remnant state. It is demonstrated that the strong contrast spots, inside the yellow circle, cannot be ascribed to a DW, as it is illustrated in (b).

In Figure 3.11a, contrary to that shown in Figure 3.10, there is no DW displacement. When the magnetization of the whole wire changes its direction, the area in the yellow circle reverses its contrast, due to the change of sign of the OOP component of the stray field at the diameter enlargement (see Figure 3.11b), which is coupled to the axial magnetization direction. This behavior cannot be explained with the existence of a pinned domain wall but rather with the existence of high stray field regions induced by the presence of defects.

The two different behaviors shown ahead, speak highly of the convenience of performing VF-MFM measurements to determine whether a domain wall is pinned or not. MFM images in remanence alone are not conclusive, since high surface contrast might lead us to think that DWs are pinned when they are not.

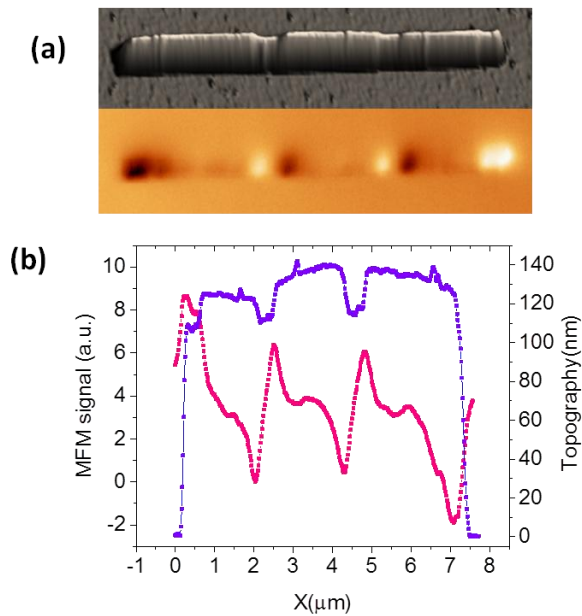


Furthermore, making use of this VF-MFM advanced technique we can track the movement of the wall along the NW, and quantify the necessary field to move the DW and the exact position at which it will be pinned. This is a necessary feature for spintronic devices, which makes these bamboo-like nanowires promising candidates to be used in applications.

### 3. Diameter modulated nanowires

Some works in the literature claim that the notches in cylindrical NWs, constitute energy wells that produce a stronger pinning potential than antinotches.<sup>12</sup> With the purpose of investigating their effect on the magnetization reversal, nanowires of varying diameter segments were grown by electrodeposition. The segment lengths ( $l=400$  nm;  $L= 1000$ nm) have been chosen in a way to create a notched structure (see FeCo<sub>3</sub> in table 3.1).

Regarding fabrication, nanopores with tailored periodical diameter modulations were produced by applying pulses of 130 and 100 V for 5 and 150 s, respectively. The pulses were repeated 30 times to obtain a total length of the modulated pores of about 50  $\mu$ m.

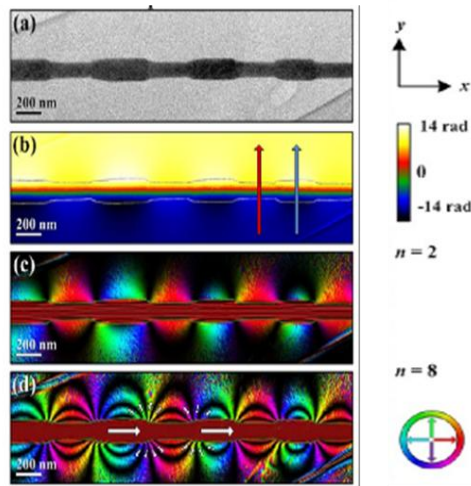


**Figure 3.12** MFM and topographic images of a notched NW, together with their profiles. MFM signal is represented in pink and topography is represented in purple.

Figure 3.12b shows MFM and AFM profiles of a representative nanowire. It is important to highlight that each NW displays a different length, different number of segments and consequently, they might end with either big  $D$  or small  $d$  diameter in the edges.

The importance of the type of ending in the magnetic charge distribution and emerging stray field was studied by Dr. L.A. Rodriguez et al. through electron holography.<sup>29</sup> Profiles from the magnetic and topographic images plotted in Figure 3.12b, show that in remanence, the presence of the notches gives rise to the appearance of magnetic charges (see intermediate intensity contrasts, at the middle of the nanowire). Still, the edges present the strongest dark-bright contrast, which is indicative of an overall axial magnetization. Based on the experience acquired in the previous part of this chapter, where the presence of charges account for a strong stray field at the points where there is a change in the diameter, instead of a domain wall, we are skeptical about the presence of DWs in this particular notched structure.

Electron holography measurements were performed in the frame of collaboration work with the group of Prof. E. Snoeck, from the CEMES-CNRS in Toulouse. Measurements carried out by Dr. L. A. Rodriguez show the lack of domains together and inner axial magnetization, together with high stray field emerging from the notches (Figure 3.13).

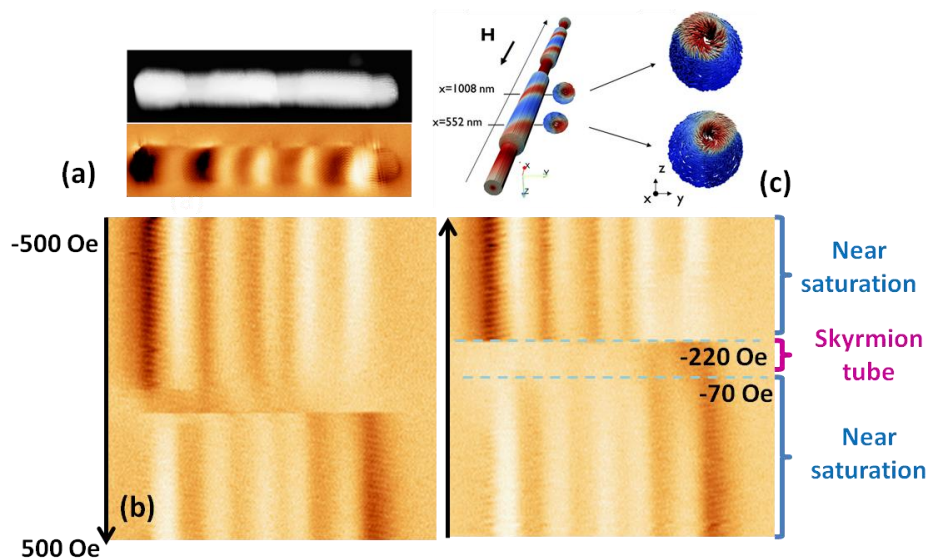


**Figure 3.13** (a) TEM image displaying the morphology of the NW. (b) EH magnetic phase shift image reconstructed for a section of the NW. (c) and (d) Magnetic flux images reconstructed from the magnetic phase shift images using an amplifier factor of  $n = 2$  and  $8$ , respectively.

Color in the magnetic flux images indicates only the magnetic induction direction according to the inserted color wheel. White arrows account for an overall axial magnetization. Taken from [ref29].

Again, the magnetization reversal of these NWs was studied by the advanced Variable field MFM measurements, explained in chapter 2. Interestingly, MFM confirms the absence of domain pinning shown by EH. This might be indicative of i) a pinning mechanism that occurs in a time scale beyond our measurement capacity or ii) specific dimensions of the sample not favoring the potential well predicted theoretically.

Some nanowires reverse their magnetization in a single Barkhausen jump, just like straight nanowires do. In addition, their critical fields do not show significant variation in comparison to their straight counterparts. Nevertheless, some differences have been found in their magnetization reversal, compared to straight or *bamboo-like* nanowires. An atypical behavior has been found in some of the nanowires which, as evidenced in Figure 3.14b, lose their contrast at a certain field range when their magnetization is being reversed by an axial magnetic field. In its remnant state, however, the nanowire does not display any unusual feature (Figure 3.14a).



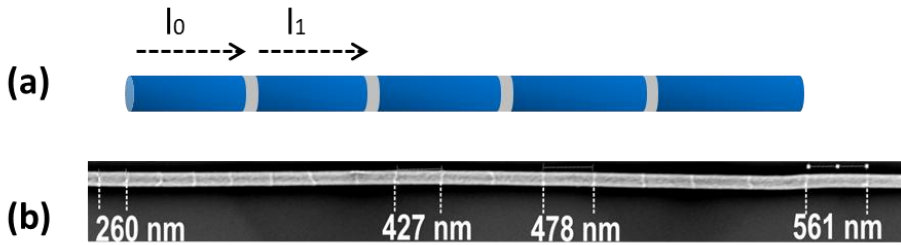
**Figure 3.14** (a) Topographic and magnetic images of a NW. (b) VF-MFM displaying a field range where stray field contrast is unexpectedly lost. (c) Skyrmionic tubes formed in the demagnetization and zoom of their cross sectional view. Adapted from [ref<sup>28</sup>].

Recently, J.A. Fernández-Roldán et al. published a theoretical description of peculiar reversal mechanisms found in Ni and FeNi nanowires with diameter modulation.<sup>28</sup> They claim that for nanowires with large enough diameter differences  $D-d$ , the magnetization reversal takes place beginning with the formation of vortices at the notches and followed by the rotation of the spins of the outer shell. The switching of the magnetic moments in the shell previous to the rotation of those in the core, entails the creation of a Bloch skyrmion tube, prior to the switching of the magnetization of the whole NW.

This effect might explain the lack of MFM contrast in the range between  $\pm 70$  to  $\pm 220$  Oe, if we keep in mind that the core and the shell would generate stray fields of opposite sign in the edges of the nanowire which could compensate in such a way to produce no net MFM signal. The same applies to the areas with notches, where the formation of vortices can lead to stray field attenuation. Future XMCD-PEEM experiments, with in-situ fields might be convenient to directly visualize the core and shell magnetization simultaneously and confirm this interpretation of the VF-MFM data.

#### 4. FeCo nanowires with separated by Cu layers

The introduction of segments of a different material along ferromagnetic nanowires is another way of creating controlled pinning sites (FeCo4).<sup>30</sup> This can be done by alternating two ferromagnetic materials of different magnetic features (i.e. coercivity), or by using a non-magnetic material playing the role of controlled defect. In this part of the thesis we have studied the influence of Cu segments in the magnetization reversal of FeCo nanowires. On the other hand, the unidirectional motion of the DWs is a desired feature for the consecution of a DW shift registers or spintronic based logic devices. In an attempt to tune the energy landscape and create a domain wall ratchet,<sup>31,32</sup> Cu segments have been spaced out with growing separation distance, making the ferromagnetic segments bigger as they move from one edge to the opposite (see Figure 3.15). A magnetic ratchet device originates in the asymmetric energy barrier and allows linear motion in a single direction preventing it in the opposite one.



**Figure 3.15** (a) Sketch to illustrate the size pattern displayed by the nanowires. (b) SEM image showing the segment size increment.

The size of each individual segment is given by

$$l_i(x) = l_{i-1} + \alpha$$

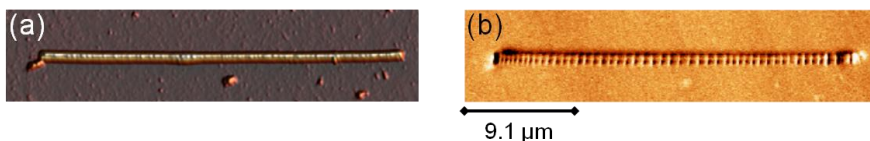
where  $d$  is the size of each ferromagnetic segment and was chosen to be  $\alpha = 15\text{nm}$ . In turn, the Cu segment size remains constant (30nm).

As in former examples, NWs were grown by potentiostatic electrodeposition, whose rate grows in time to result in FeCo magnetic segments with increasing length from one end to the opposite one.

#### 4.1. Correlation between topography and magnetization

MFM experiments were performed in a number of nanowires (over ten different sample nanowires). Data presented here is representative of the overall behavior.

Measurements were undertaken firstly in the “as prepared” magnetic state (Figure 3.16). As expected, the strong dark-white magnetic contrast confirms the overall axial magnetization in the nanowires. The intermediate dark-bright pattern conversely, evidences the presence of magnetic charges at the FeCo/Cu interfaces. Figure 3.16 shows the topographic and magnetic images of a selected typical nanowire. Notice that the length of segments increases from around 300 nm to 1000 nm as one moves from the left to the right end.



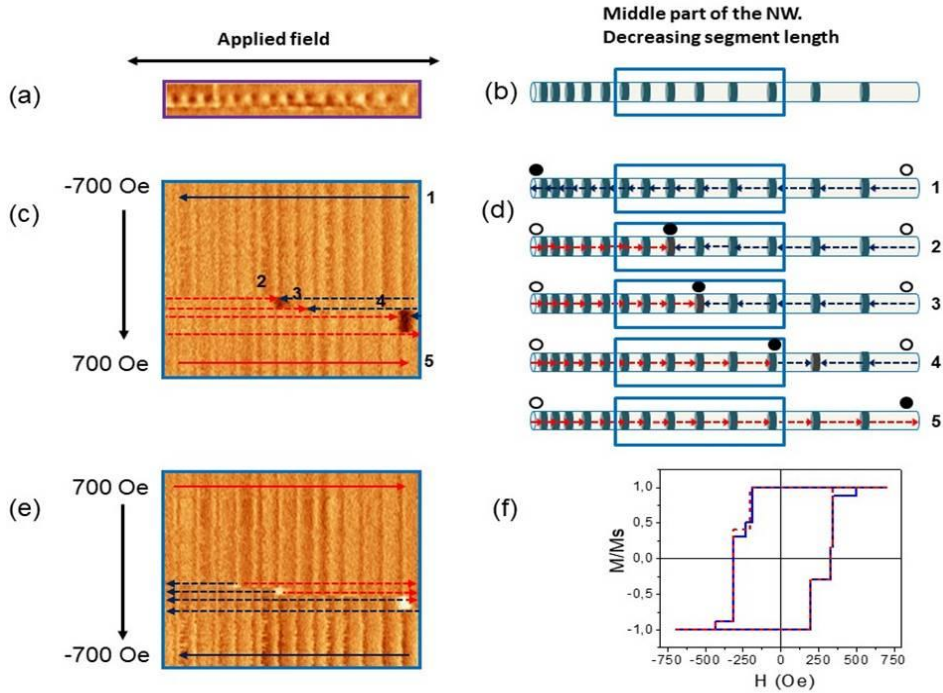
**Figure 3.16** (a) Topographic and Magnetic (b) images of the multisegmented nanowire in as-prepared magnetic state. MFM image shows that magnetic charges are accumulated at the FeCo/Cu interfaces.

## 4.2. Magnetization reversal

To study the magnetization reversal process, further measurements were carried out under *in-situ* applied magnetic field along the nanowires through non-standard MFM modes explained in chapter 2. The maximum applied field, around 700 Oe, is high enough to overcome the main irreversible magnetization processes although possibly not the magnetic saturation.

Figure 3.17b shows the schematic view of a whole NW and the MFM image (Figure 3.17a) of its central part. Several successive minor hysteresis loops are performed under the same conditions (panel (c) and (e) show the first one, schematically explained in Figure 3.17d). Since the whole NW could not be imaged at once due to size restrictions, we have added a white or black circle as a reminder of the corresponding MFM contrast where it would correspond if the whole NW was measured. In the first branch (Figure 3.17c), only a black contrast moves in the scanned area, while in the second branch (Figure 3.17e) the field is reversed and a white contrast is moving along the central area.

It is possible to reconstruct a hysteresis loop from the numerical data in the non-standard MFM images. It is shown in Figure 3.17f: loop 1 is depicted in blue and loop 2 is represented with a red dashed line and shows less jumps, although the curves generally overlap. Both loops correspond to the same nanowire, measured in equivalent conditions, which evidences the stochastic nature of the pinning.

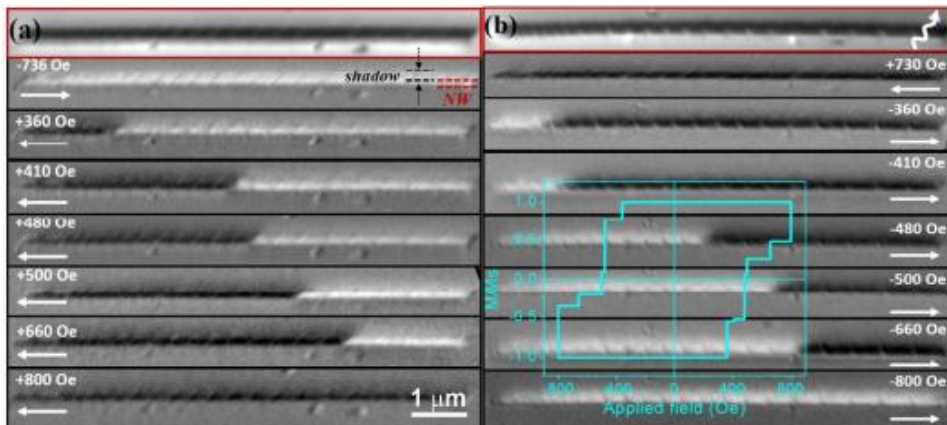


**Figure 3.17** (a) MFM image of the central part of the nanowire where the measurement with field is carried out. (b) Sketch of the multisegmented nanowire, with the short segments located in the left side. In (c) and (e), the sample is submitted to a minor hysteresis cycle. (d) Shows schematically the magnetic configuration that the piece of nanowire undergoes during field swept in (c). The hysteresis curve has been reconstructed in blue (f), together with a subsequent cycle.

We underline the following results: i) magnetization reversal proceeds in few steps by which a reverse domain forms and a “domain barrier” is created at intermediate local positions. Notice that we use the term domain barrier instead of domain wall, because there is a non-magnetic segment (Cu) forcing the magnetization to reverse in steps. ii) The number and position of such pinning centers may vary from scan to scan (as well as from nanowire to nanowire) although in some cases preferred sites are observed. iii) Regarding the quantitative values, switching occurs at around 200 Oe in the shorter segments and increases to 300 or 500 Oe (i.e., 500 Oe at the nanowire in Figure 3.17) as one moves to longer segments.

XMCD-PEEM measurements were carried out at ALBA Synchrotron, with the assistance of Dr. L. Aballe, Dr. M. Foester and Dr. A. Fraile-Rodríguez for the

determination of the magnetization distribution both at the surface and at the inner part of nanowires. Direct X-ray Absorption Spectroscopy (XAS) images at the Co L3 absorption edge are shown inside a red square for chemical identification of the Cu segments (Figure 3.18). Below, XMCD-PEEM images contain information about the NW surface and from the core. The NW contrast display dark-bright signal from the NW surface photoemission (dotted lines labeled NW). The shadow corresponds to the photoemission from the substrate after transmission through the wire core (region of uniform opposite contrast). In-plane magnetic field up to  $\pm 800$  Oe was applied to track the evolution of the domain configuration. The results show good agreement with MFM data shown in Figure 3.18.



**Figure 3.18** Sequences of XAS (marked in red, and indication of the beam direction) and PEEM images of a multisegmented FeCo/Cu nanowire, previously magnetized under maximum field along rightward (a) and leftward (b) polarity, where Cu segments can be identified. Selected PEEM images under increasing applied field along the leftward (a) and rightward (b) polarity.

The inset in (b) shows the reconstructed hysteresis loop.

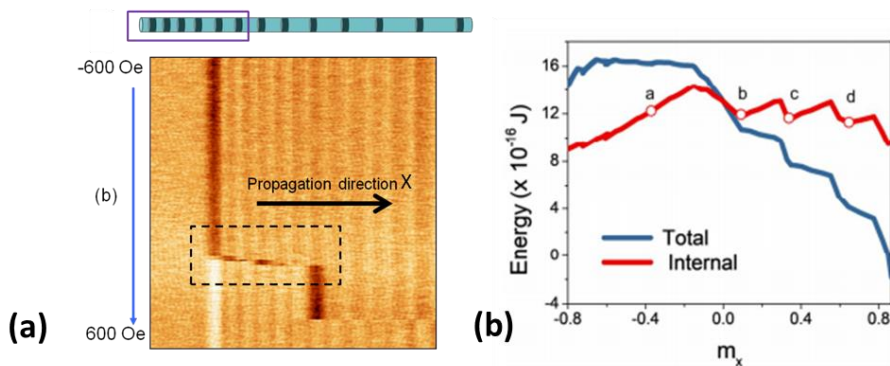
#### 4.2.1. Directional DW propagation

After imaging several NWs, we confirm that in every sample the magnetization reversal begins in the end with smaller segments towards that with increasing segments size. This effect can be noticed in the image below, where thanks to the magnetic charges accumulated in the interfaces, we can see that segments in the left are smaller than those in the right. We should keep in mind that we are dealing with a non-standard MFM image of one



end of the NW, hence, there is a strong contrast arising from the stray field of the edge.

Attention should be paid to the subtle stair-like contrast propagating towards the right, inside a dashed square (Figure 3.19). This probes that the magnetization reversal takes place segment by segment unidirectionally, as it was intended by growing increasing segment sizes. At a certain field (370 Oe) the propagation stops and more energy is needed to overcome the next barrier, probably due to an uncontrolled defect during fabrication.

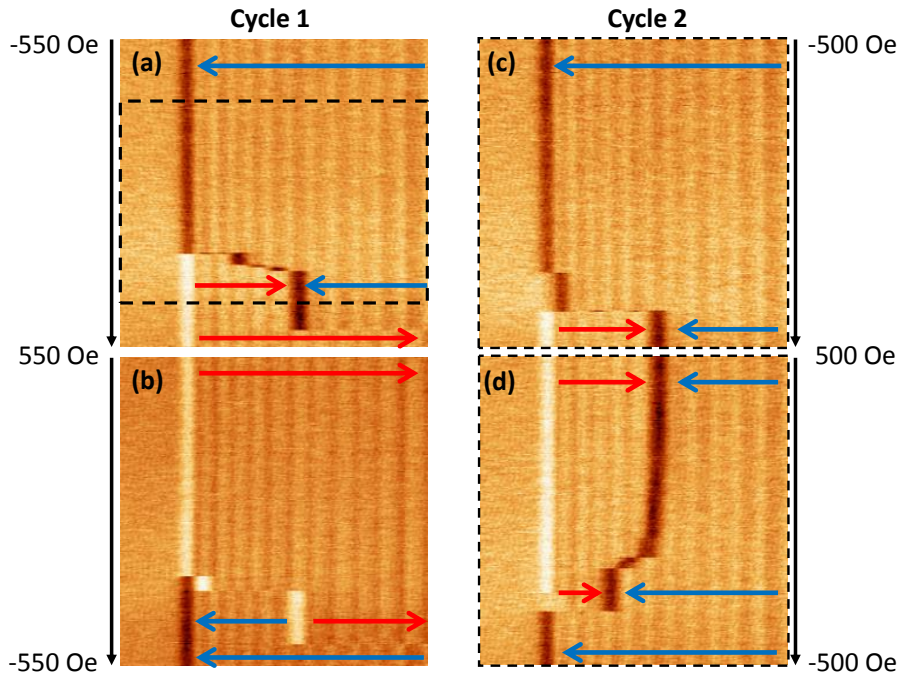


**Figure 3.19** (a) Edge of the nanowire with shorter segments subjected to a minor hysteresis loop. Inside the dashed square little jumps can be appreciated where segments are reversing their magnetization one by one, from left to right. (b) The DW propagation is unidirectional due to the energy landscape.

The unidirectional propagation has been accomplished by the manipulation of the energy landscape, creating a magnetic ratchet through the sequential increase of the ferromagnetic segments. Micromagnetic simulation analysis (Figure 3.19b) performed by J.A. Fernandez-Roldan and O. Fesenko, shows that magnetization pinning in the idealized modelled case occurs in short segments only. Although pinning centers are stabilized by defects in real systems (Figure 3.19a), they are not true energy minima states.<sup>33</sup>

After studying one particular NW, its critical fields, preferential sites, etc., we can reach some control over its configurations. An example is shown in Figure 3.20. Notice that the piece of NW is the same as the one presented in Figure 3.19. In Figure 3.20c and d, a smaller field range has been selected in order to keep the right part of the NW with opposite magnetization to the

rest of the NW. This control is fully necessary for the development of domain wall based information storage technologies.



**Figure 3.20** (a) Shows a sketch of the NW, where the short segments are located in the left. (b), (c), (d) and (e) display two subsequent minor hysteresis loops, where the magnetization reversal takes begins in the area with shorter segments.

## 5. Conclusions

Periodical enlargements of the diameter, such as in bamboo-like nanowires, change the magnetization reversal process, making the domain wall stop in every modulation site. The switching of the magnetization is vortex mediated.

The presence of uncontrolled growing defects has a big influence on the magnetization reversal.

Amongst the three approaches used to pin domain walls, the growth of a non-magnetic spacer has been statistically the most successful.

The growing separation of ferromagnetic segments with Cu layers is a successful way of controlling the propagation direction. It was already known that segments with smaller aspect ratio are magnetically softer due to smaller demagnetizing field.

Magnetic Force Microscopy proves to be a reliable tool for the study of uniaxial magnetic nanowires. Particularly, the use of advance VF-MFM modes is necessary to determine if a pinning mechanism is taking place.

There is room for further investigation to find fully reliable means to control the pinning mechanism. The combination of two types of defects is encouraged for future works. Diameter modulation in the interfaces between ferromagnetic and non-magnetic spacers might help to stabilize intermediate pinning sites.

Segment by segment increase in the diameter modulation, within reasonable dimensions, could create increasing energy barriers to move a domain wall from one position to the next.

The following articles have been sent for publication in relation with the work presented in this chapter:

- (1) Bran, C.; Berganza, E.; Palmero, E.M.; Fernández-Roldán, J.A.; P. del Real, R.; Aballe, L.; Foerster, M.; Asenjo, A.; Vázquez, M. Spin configuration of cylindrical bamboo-like magnetic nanowires. *J. Mater. Chem. C* **4**, 978–984 (2016).
- (2) Berganza, E.; Bran, C.; Jaafar, M.; Vazquez, M.; Asenjo, A. Domain wall pinning in FeCoCu bamboo-like nanowires. *Sci. Rep.* **6**, (2016).
- (3) Rodríguez, L. A.; Bran, C.; Reyes, D.; Berganza, E.; Vázquez, M.; Gatel, C.; Snoeck, E.; Asenjo, A. Quantitative Nanoscale Magnetic Study of Isolated Diameter-Modulated FeCoCu Nanowires. *ACS Nano* **10**, 9669–9678 (2016).
- (4) Bran, C.; Berganza, E.; Fernandez-Roldan, J.A.; Palmero, E.; Meier, J.; Calle, E.; Jaafar, M.; Forster, M.; Aballe, L.; Fraile Rodriguez, A.; P. del Real, R.; Asenjo, A.; Chubykalo-Fesenko O.; Vazquez, M. A ratchet-like effect in magnetic cylindrical nanowires. *Submitted*.

## 6. References

1. Parkin, S. S. P., Hayashi, M. & Thomas, L. Magnetic domain-wall racetrack memory. *Science* **320**, 190–194 (2008).
2. Faulkner, C. C. *et al.* Artificial domain wall nanotraps in Ni<sub>81</sub>Fe<sub>19</sub> wires. *J. Appl. Phys.* **95**, 6717–6719 (2004).
3. Pi, U. H. *et al.* Static and dynamic depinning processes of a magnetic domain wall from a pinning potential. *Phys. Rev. B - Condens. Matter Mater. Phys.* **84**, (2011).
4. Kläui, M. Head-to-head domain walls in magnetic nanostructures. *Journal of Physics Condensed Matter* **20**, (2008).
5. Beach, G. S. D., Nistor, C., Knutson, C., Tsoi, M. & Erskine, J. L. Dynamics of field-driven domain-wall propagation in ferromagnetic nanowires. *Nat. Mater.* **4**, 741–744 (2005).
6. Yamaguchi, A. *et al.* Real-Space Observation of Current-Driven Domain Wall Motion in Submicron Magnetic Wires. *Phys. Rev. Lett.* **92**, (2004).
7. Bogart, L. K., Atkinson, D., O’Shea, K., McGrouther, D. & McVitie, S. Dependence of domain wall pinning potential landscapes on domain wall chirality and pinning site geometry in planar nanowires. *Phys. Rev. B - Condens. Matter Mater. Phys.* **79**, (2009).
8. He, K., Smith, D. J. & McCartney, M. R. Observation of asymmetrical pinning of domain walls in notched Permalloy nanowires using electron holography. *Appl. Phys. Lett.* **95**, (2009).
9. Da Col, S. *et al.* Observation of Bloch-point domain walls in cylindrical magnetic nanowires. *Phys. Rev. B - Condens. Matter Mater. Phys.* **89**, (2014).
10. Ferguson, C. A., Maclaren, D. A. & McVitie, S. Metastable magnetic domain walls in cylindrical nanowires. *J. Magn. Magn. Mater.* **381**, 457–462 (2015).
11. Yan, M., Kákay, A., Gliga, S. & Hertel, R. Beating the Walker limit with massless domain walls in cylindrical nanowires. *Phys. Rev. Lett.* **104**, (2010).
12. Chandra Sekhar, M., Goolaup, S., Purnama, I. & Lew, W. S. Depinning assisted by domain wall deformation in cylindrical NiFe nanowires. *J. Appl. Phys.* **115**, (2014).
13. Piao, H. G., Shim, J. H., Djuhana, D. & Kim, D. H. Intrinsic pinning behavior and propagation onset of three-dimensional Bloch-point domain wall in a cylindrical ferromagnetic nanowire. *Appl. Phys. Lett.* **102**, (2013).
14. Palmero, E. M., Bran, C., Del Real, R. P. & Vázquez, M. Vortex domain wall propagation in periodically modulated diameter FeCoCu nanowire as determined by the magneto-optical Kerr effect. *Nanotechnology* **26**, (2015).
15. Esmaeily, A. S., Venkatesan, M., Razavian, A. S. & Coey, J. M. D. Diameter-modulated ferromagnetic CoFe nanowires. in *Journal of Applied Physics* **113**, (2013).

16. Ivanov, Y. P., Chuvilin, A., Lopatin, S. & Kosel, J. Modulated Magnetic Nanowires for Controlling Domain Wall Motion: Toward 3D Magnetic Memories. *ACS Nano* **10**, 5326–5332 (2016).
17. Iglesias-Freire, Ó. *et al.* Spin configuration in isolated FeCoCu nanowires modulated in diameter. *Nanotechnology* **26**, (2015).
18. Iglesias-Freire, O. Advances in Magnetic Force Microscopy. (Universidad Autónoma de Madrid, 2014).
19. Berganza, E., Bran, C., Jaafar, M., Vazquez, M. & Asenjo, A. Domain wall pinning in FeCoCu bamboo-like nanowires. *Sci. Rep.* **6**, (2016).
20. Minguez-Bacho, I., Rodríguez-López, S., Vázquez, M., Hernández-Vélez, M. & Nielsch, K. Electrochemical synthesis and magnetic characterization of periodically modulated Co nanowires. *Nanotechnology* **25**, (2014).
21. Vega, V. *et al.* Tuning the magnetic anisotropy of CoNi nanowires: Comparison between single nanowires and nanowire arrays in hard-anodic aluminum oxide membranes. *Nanotechnology* **23**, (2012).
22. Lee, W., Kim, J. C. & Cösele, U. Spontaneous current oscillations during hard anodization of aluminum under potentiostatic conditions. *Adv. Funct. Mater.* **20**, 21–27 (2010).
23. Bran, C. *et al.* Spin configuration of cylindrical bamboo-like magnetic nanowires. *J. Mater. Chem. C* **4**, 978–984 (2016).
24. Jaafar, M. *et al.* Hysteresis loops of individual Co nanostripes measured by magnetic force microscopy. *Nanoscale Res. Lett.* **6**, 1–6 (2011).
25. Allende, S., Altbir, D. & Nielsch, K. Magnetic cylindrical nanowires with single modulated diameter. *Phys. Rev. B - Condens. Matter Mater. Phys.* **80**, (2009).
26. Shinjo, T., Okuno, T., Hassdorf, R., Shigeto, K. & Ono, T. Magnetic vortex core observation in circular dots of permalloy. *Science (80-. )*. **289**, 930–932 (2000).
27. Burn, D. M. & Atkinson, D. Suppression of Walker breakdown in magnetic domain wall propagation through structural control of spin wave emission. *Appl. Phys. Lett.* **102**, (2013).
28. Fernandez-roldan, J. A., Real, R. P., Bran, C. & Vázquez, M. Magnetization pinning in modulated nanowires : from topological protection to the ‘ corkscrew ’ mechanism. 1–29 (2018). doi:10.1039/C8NR00024G
29. Rodríguez, L. A. *et al.* Quantitative Nanoscale Magnetic Study of Isolated Diameter-Modulated FeCoCu Nanowires. *ACS Nano* **10**, 9669–9678 (2016).
30. Oázkale, B. *et al.* Multisegmented FeCo/Cu nanowires: Electrosynthesis, characterization, and magnetic control of biomolecule desorption. *ACS Appl. Mater. Interfaces* **7**, 7389–7396 (2015).
31. Franken, J. H., Swagten, H. J. M. & Koopmans, B. Shift registers based on magnetic domain wall ratchets with perpendicular anisotropy. *Nat. Nanotechnol.* **7**, 499–503

- (2012).
32. Lavrijsen, R. *et al.* Magnetic ratchet for three-dimensional spintronic memory and logic. *Nature* **493**, 647–650 (2013).
  33. Bran, C. *et al.* A ratchet-like effect in magnetic cylindrical nanowires. (*submitted*) (2018).





# **CHAPTER 4**

**Complex domain  
configurations in  
magnetic nanowires.**

Unveiling the magnetic configuration of nanowires with complex spin textures is a challenge that can be addressed with MFM.<sup>1,2</sup> In the previous chapter, we have described the magnetization reversal processes of several systems with uniaxial magnetization that present geometric and compositional modifications to gain control over it. In all cases FeCo alloy was chosen because of its low magnetocrystalline compared to the NW shape anisotropy.

Nonetheless, if a material with high anisotropy is selected, more complex domain configurations arise as a result of the interplay between shape and magnetocrystalline anisotropies.<sup>3,4</sup> Vortex configurations are expected for Co nanowires of around 100nm. The magnetization reversal modes of Co nanowires embedded in alumina membranes<sup>5,6,7</sup> have been an active subject of study.

As a matter of fact, some authors have proposed vortex based spintronic devices as an alternative to single domain elements,<sup>8,9</sup> due to the high stability of the vortex configurations under thermal fluctuations and low size of the core, whose polarization, pointing up or down can represent 0 or 1 states of a bit, in the case of a magnetic memory or a logic system.

However, less works focus on the study of individual Co cylindrical NWs<sup>3</sup> in comparison to the large amount of studies devoted to the investigation of Co lithographed nanostripes.<sup>10,11</sup> Curvature represents a major challenge in the characterization of cylindrical NWs, as well as some advantages from the application point of view, explained in Chapter 3. The absence of walker breakdown<sup>12</sup> is of particular relevance for applications. Obviously, any practical implementation of NWs in a device requires a deep understanding of the domain structure and magnetization reversal modes. In this context, individual imaging of the NWs<sup>13,14</sup> sheds some light on this subject.

This chapter is focused on cobalt based NWs, whose strong magnetocrystalline anisotropy -of the order of  $10^5 \text{J/m}^3$ -, contributes to the development of a perpendicular magnetization easy axis. Three sets of samples were all grown inside alumina membranes through potentiostatic electrodeposition, as explained in Chapter 3.

As in the case of FeCoCu NWs, the first studied set are made of pure Co with similar dimensions to those studied in Chapter 3 and variations in their diameters. We have analyzed the impact of the diameter variations over the magnetic configuration in Co NWs with different crystallographic structures.<sup>1</sup>

In the second set, CoNi alloy NWs of varying composition are studied<sup>15</sup>. Using a magnetic alloy is a good way of combining the properties of two different ferromagnetic materials and improving them. In this case, the aim is to study the influence of the composition over their resulting magnetic configuration.

Finally, in the last set, which is the most extensive work of the three presented here, magnetic/magnetic multisegmented nanowires are characterized.<sup>2</sup> CoNi and Ni segments –whose magnetic behavior is different—are consecutively alternated. As a result, a peculiar periodic magnetic configuration is found. All samples studied in this chapter were grown by Dr. C. Bran, from the group of Prof. M. Vazquez, in the electrochemistry laboratory from ICMM-CSIC.

CoNi alloys are very versatile magnetic materials that can exhibit either a soft or a hard magnetic behavior depending on the Co content. They present a significant magnetocrystalline anisotropy which makes them an alternative to Fe–Ni alloy based systems with small anisotropy.<sup>16</sup> Ni-rich NWs typically exhibit fcc structure, however, when Ni concentration decreases (Ni atoms are partially substituted by Co), a transition from fcc to hcp phase is observed<sup>17,18</sup>, although both crystalline structures seem to coexist for alloys close to  $\text{Co}_{50}\text{Ni}_{50}$ <sup>19</sup>, forming clusters of fcc and hcp crystals.

As stated in previous works,<sup>20,21,22</sup> CoNi bulk alloys can present very different magnetocrystalline anisotropy values depending on their exact composition. Thanks to the high solubility of Co atoms in the Ni lattice (and vice versa), it is possible to tailor the stoichiometry.

Although the magnetic properties of arrays of NWs have been studied in different works (see for example ref 23), fewer studies have focused on the magnetic states of isolated NWs. The main reason is that the observation of the magnetic configuration in isolated NWs requires advanced techniques with high sensitivity and lateral resolution.

For this study, three samples with varying Co and Ni content were fabricated (table 2). Their hysteresis loops (Figure 4.5) show that the magnetization easy axis can be tilted from axial to perpendicular by increasing the Co content. As a general rule, compositions closer to pure Co have dominant magnetocrystalline anisotropy, while shape anisotropy determines the magnetization in Ni rich NWs.

Multisegmented magnetic/metallic NWs are particularly interesting for engineering new magnetic structures and for the design of advanced spintronic devices.<sup>24</sup> Magnetic/Magnetic multilayers, instead, are designed to control the motion of a propagating domain wall at the frontier of segments with different anisotropy characteristics. Co-based NWs have the advantage of exhibiting a variety of magnetic properties that can be tailored in the fabrication process.<sup>25,26</sup>

## 1. Geometrically modulated Co NWs

Geometrical modulation of the nanowire diameter was introduced in Chapter 3 as a method to control the magnetization reversal and produce pinning sites. In this part, two Co samples were fabricated with *bamboo-like* shape and different crystallographic structure. Table 4.1 summarizes their main features. The right choice of electrodeposition conditions allow growing NWs of different crystallographic structure,<sup>7</sup> namely fcc or hcp, being the second one the most commonly found. The control over the crystallographic structure entails the selection of weaker or stronger magnetocrystalline anisotropy, since the corresponding anisotropy value of these phases differs in one order of magnitude. To grow these nanowires a  $\text{CoSO}_4 \cdot 7\text{H}_2\text{O}$  (0.36M)+ $\text{H}_3\text{BO}_3$ (0.16M) electrolyte was used.

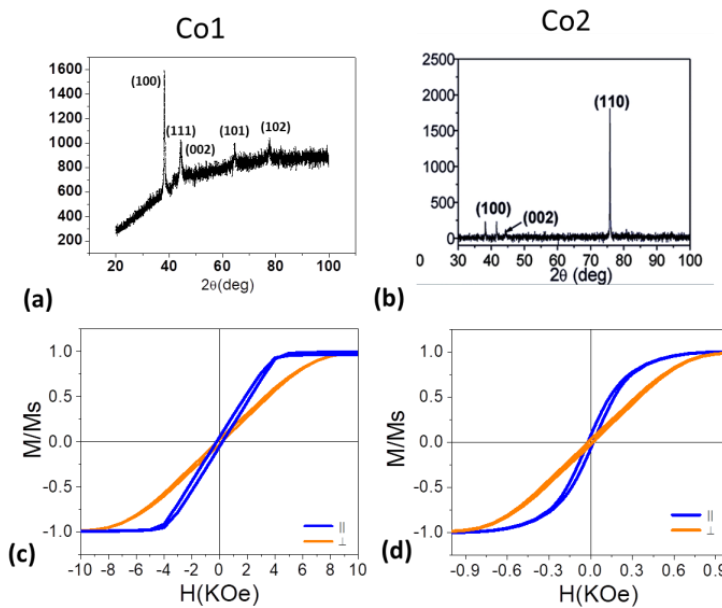
Sample	Co1	Co2
Texture	Fcc	Hcp
Periodicity	800nm	400nm
Average length	12 $\mu\text{m}$	12 $\mu\text{m}$
Diameter	150-170nm	150-170nm

**Table 4.1.** Summary of the Co *bamboo-like* NWs.

Strong magnetocrystalline anisotropy characterized hcp phase. Its hexagonal symmetry axis *c* tilts the easy axis of the nanowire, which lies almost

perpendicular to the cylinder axis. In this study, we wanted to assess the influence of the bamboo-like shape in magnetic nanowires with different magnetocrystalline anisotropies.

The data from table 4.1 has been verified by X-ray diffraction (XRD) and Scanning Electron Microscopy (SEM) measurements. As expected, sample Co1, grown in fcc texture (Figure 4.1a), has its magnetization easy axis in the axial direction (Figure 4.1c), while sample Co2, showing the characteristic hcp XRD peaks (Figure 4.1b) possesses a tilted easy axis.

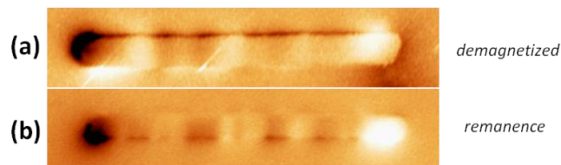


**Figure 4.1** (a) and (b) display XRD diffractogram from samples Co1 and Co2 respectively. (c) and (d) show the corresponding axial and perpendicular hysteresis loops of the studied NW arrays.

The effect of the geometrical modulation has been studied through standard MFM measurements, performing changes in their magnetic state with externally applied saturating fields or demagnetizing sequences (by applying decreasing fields of alternating sign).

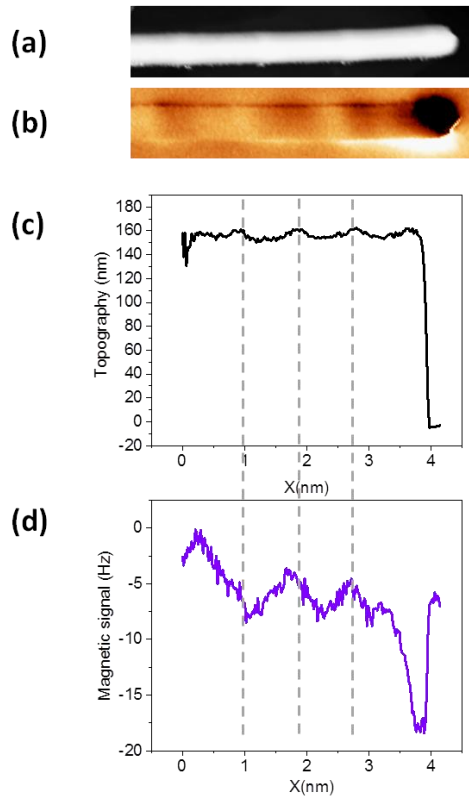
Sample Co1 presents diameter maxima every 800nm. It displays the same shape as the nanowire FeCo2 whose schematic representation is shown in Figure 3.1 of Chapter 3. Its fcc texture and lower magnetocrystalline anisotropy makes it more similar to the *bamboo-like* FeCoCu. As expected

from the hysteresis loops presented in Figure 4.1c, after growing with fcc texture, its easy axis coincides with the cylinder axis. Therefore, its MFM contrast is mainly dipolar –bright and dark edges- plus additional weaker signal in the middle. If the magnetic state of the sample is changed (Figure 4.2), it was statistically noted that the nanowires do not change their magnetic configuration. The shape anisotropy dominates inducing a bistable configuration, with the spins pointing in either axial direction.



**Figure 4.2** (a) Co1 in demagnetized state. (b) Different NW (of sample Co1) in remnant state, after been subjected to a perpendicular field.

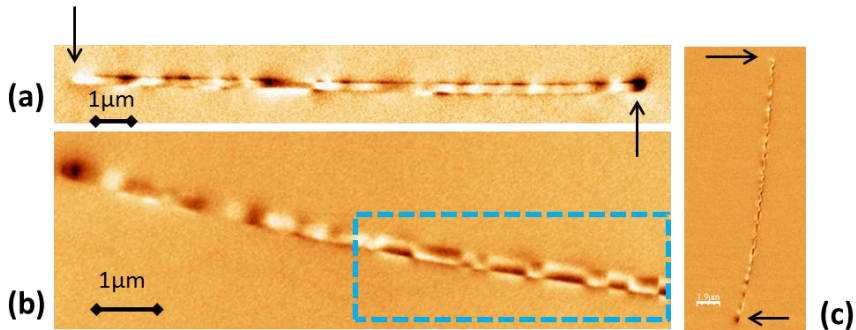
A simultaneous study of topographic and magnetic profiles (Figure 4.3 a-c and b-d) unveils a correlation, to some extent, between geometrical modulation and magnetic signal. This is not, however, as obvious as it is in FeCoCu NWs, although the dashed lines show relatively good agreement between topography and magnetic image.



**Figure 4.3** (a) Topography and (b) MFM image of a piece of nanowire (Co1). Their corresponding profiles in (c) and (d) reflect a correlation between geometrical modulation and magnetic configuration.

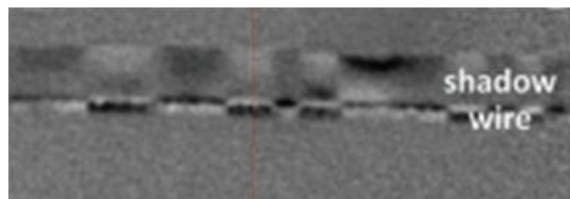
Sample Co2, instead, presents a complex magnetic configuration at first sight. Vortex formation is expected due to the anisotropy term competition, although in the demagnetized state (Figure 4.4a) the interpretation of the domain structure is not straightforward. When perpendicular field is applied –up to 18000 Oe–, vortex formation is promoted (blue dashed square in Figure 4.4b), as deduced from the dark-bright little segments coming from the OOP component of their stray field. The vortices extend several hundreds of nanometers in a non-periodical fashion, and thus, the geometrical modulation seems not to have any influence on it. The piece of NW in Figure 4.4b is a zoom of the nanowire in Figure 4.4c. Although due to measurement limitations this image does not display the magnetic configuration clearly, it shows that the edges of the nanowire present strong enough bright and dark contrasts, similar to the demagnetized NW in Figure

4.4a. This means that despite the complexity of the shell structure, there is a core oriented in the axial direction.



**Figure 4.4** (a) Co<sub>2</sub> NW in the demagnetized state. (b) displays a zoom of the lower part of the NW in MFM image of the NW in (c) after a subjecting it to a saturating perpendicular field.

This has been proven by XMCD measurements and confirmed through micromagnetic simulations.<sup>1</sup> As it can be deduced from the XMCD image in Figure 4.5 (performed in the Circe line of Alba synchrotron), the dark-bright contrast from the reflected signal (wire) and the opposite faint contrast from the transmitted signal (shadow), show accordance with the interpretation of the MFM images as a sequence of vortices. In the middle of the shadow, the faint contrast demonstrates that the core is axially oriented.



**Figure 4.5** XMCD image of sample Co<sub>2</sub>. Adapted from [ref1].

In general terms, we can claim that the modulation does not influence nanowires with strong perpendicular magnetocrystalline anisotropy, conversely to nanowires showing axial magnetization, as a result of the dominant shape anisotropy.



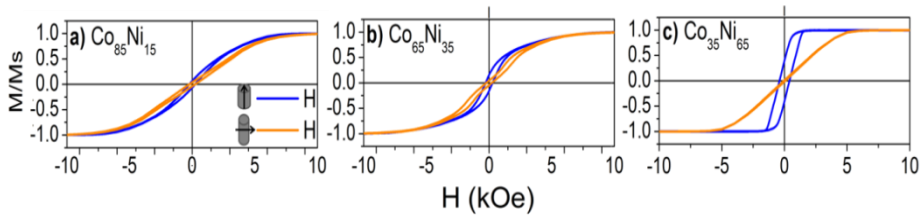
## 2. CoNi NWs: Choosing the magnetization axis.

$\text{Co}_x\text{Ni}_{100-x}$  ( $35 < x < 85$ ) alloy NWs were grown into the nanopores of AAO templates at room temperature by dc electrodeposition using the electrolytes: 0.12–0.09M  $\text{CoSO}_4$  + 0.063–0.084M  $\text{CoCl}_2$  + 0.057–0.095M  $\text{NiSO}_4$  + 0.058–0.084M  $\text{NiCl}_2$  + 0.32M  $\text{H}_3\text{BO}_3$ .<sup>19</sup> The composition of the nanowire arrays was selected by adjusting the deposition potential. The pH value was kept constant at about 3. Three samples have been studied in this part, whose details are gathered in table 4.2.

Sample	CoNi1	CoNi2	CoNi3
Composition	$\text{Co}_{85}\text{Ni}_{15}$	$\text{Co}_{65}\text{Ni}_{35}$	$\text{Co}_{35}\text{Ni}_{65}$
Texture	hcp	hcp+fcc	Fcc
Average length	18 $\mu\text{m}$	18 $\mu\text{m}$	8 $\mu\text{m}$
Diameter	120nm	120nm	120nm

**Table 4.2** Summary of the  $\text{Co}_x\text{Ni}_{100-x}$  alloy NWs, with varying composition.

As explained in the previous part, Co nanowires with hcp texture possess a perpendicular easy magnetization axis. If it is combined with Ni, the magnetization axis approaches the axial direction, as Ni content increases. This effect is verified by the hysteresis loops displayed in Figure 4.6.

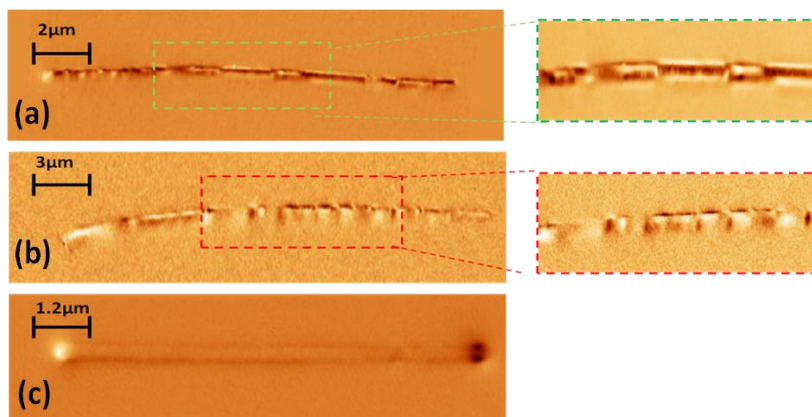


**Figure 4.6** Hysteresis loops of Samples CoNi1, CoNi2 and CoNi3.

Magnetic force microscopy shows that the Co rich NW presents a similar magnetic configuration to the one shown by Co2 in the previous section. Vortices of alternating chiralities (Figure 4.7a and 4.7b) minimize the magnetostatic energy and show up due to the transversal easy axis. In Ni rich NWs (Figure 4.7c), a dipole forms due to the weak anisotropy of Ni, which is negligible compared to the shape anisotropy.

Although the present MFM measurements are not conclusive, recent XMCD measurements show that nanowires of intermediate composition (CoNi2)

display transversal domains which coexist with vortex states.<sup>15</sup> Simulations support this fact and claim that Co rich NWs CoNi1 can also host transverse domains, with lower probability than CoNi2.



**Figure 4.7** Magnetic configuration of CoNi samples **(a)** CoNi1, **(b)** CoNi2 and **(c)** CoNi3 respectively.

We therefore conclude that compositional changes are a valid route to engineer particular domain configurations. However, particular defects can tip the energy balance to favor the creation of one configuration or another in a specific point of the NW. Despite shedding some light onto the domain configurations that one can reach by tailoring the composition, this study leaves an open door for further research to gain full control over the magnetization configuration.

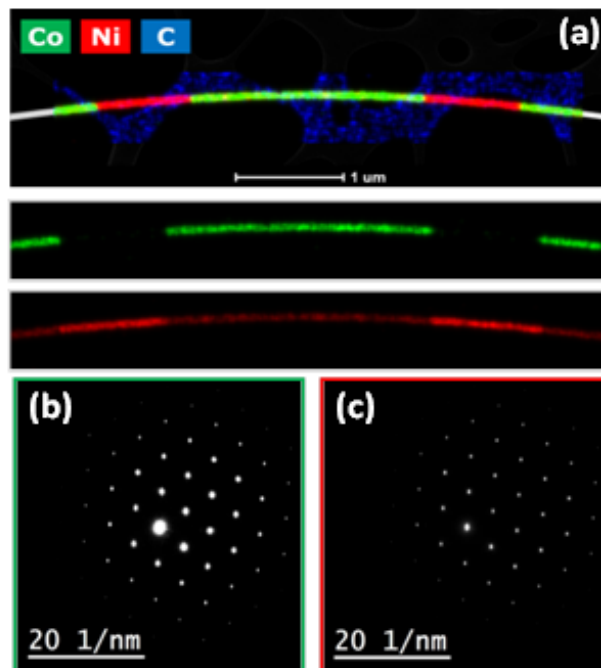
### 3. Multisegmented nanowires: CoNi-Ni.

In this part, multisegmented CoNi/Ni cylindrical NWs 120 nm in diameter and 20 μm long have been grown by electrochemical route into anodic alumina membranes (AAM). Ni and CoNi alloy segments have been alternated in the fabrication of these NWs, using two electrolytes  $\text{NiSO}_4$  (0.75 M) +  $\text{NiCl}_2$  (0.3 M) +  $\text{H}_3\text{BO}_3$  (0.3 M) and  $\text{CoSO}_4$  (0.125 M) +  $\text{CoCl}_2$  (0.08 M) +  $\text{NiSO}_4$  (0.065 M) +  $\text{NiCl}_2$  (0.11 M) +  $\text{H}_3\text{BO}_3$  (0.32 M). Their lengths, later confirmed by structural analysis, were chosen to conform a net of rods with low magnetic interaction between segments. Ni was chosen as spacer between CoNi segments, due to its low magnetization (0.61T). In addition, its lattice period allows good matching with CoNi alloy.

As highlighted in the previous section, different magnetocrystalline anisotropy values promote the development of different magnetic configurations. While in Ni segments the shape anisotropy dominates, in CoNi regions a competition between magnetocrystalline and shape anisotropies is expected.<sup>10</sup> Moreover, recently D. Reyes et al.<sup>27</sup> highlighted the strong dependence of the magnetic features of the NWs on their structural properties.

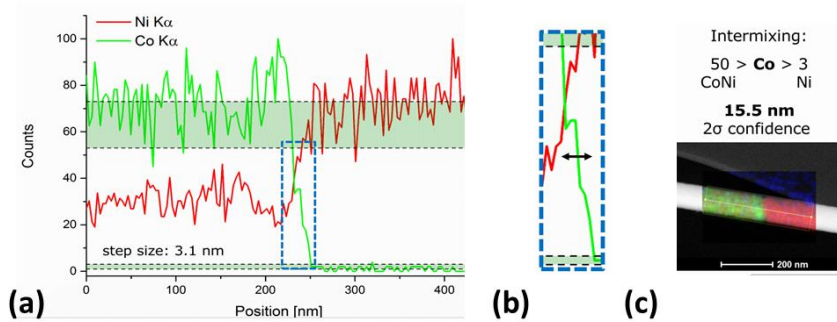
### 3.1. Crystallographic structure of CoNi segments.

To establish the relationship between structural and magnetic features, we carry on energy-dispersive X-ray spectroscopy (XEDS) measurements that enable us to map the regions with different composition and quantify the stoichiometry of the CoNi alloy (see Figure 4.8). The  $\text{Co}_{65}\text{Ni}_{35}$  segment composition has been determined and it was confirmed to be constant along the nanowire. XEDS mapping verify the sharp transition between the two layers, with an intermixing area around 15nm for Co into Ni layer (Figure 4.9), as well as the average length of the segments: 2200nm (CoNi) and 870nm (Ni).



**Figure 4.8** (a) Chemical mapping through XEDS allows identification of Co and Ni regions. STEM data superimposed to XEDS mapping as well as the separately XEDS maps corresponding to Co and Ni are shown. In (b) and (c) electron diffraction patterns of Co and Ni are presented, respectively. Both Co and Ni grow in the  $\langle 110 \rangle$  direction as shown.

Selected area electron diffraction (SAED) patterns confirms that Ni segments grow along the  $\langle 110 \rangle$  direction with fcc structure. Moreover, although it is expected that this  $\text{Co}_{65}\text{Ni}_{35}$  alloy presents a mixture between fcc and hcp phases,<sup>19</sup> CoNi segments grow epitaxially onto Ni fcc layer with a lattice parameter less than 1% bigger than the Ni lattice value. This means that in both layers the angle between the magnetic easy axis  $\langle 111 \rangle$  and the wire axis is  $35^\circ$ . As deduced from the STEM data, the size of the CoNi and Ni crystals are above 400 nm.



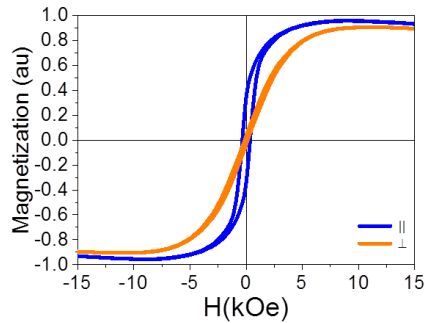
**Figure 4.9** (a) XEDS profile along the interface between layers, zoomed in (b). The piece of NW is shown in (c), with compositional contrast.

### 3.2. Single and multivortex domain configurations.

Vibrating Sample Magnetometer (VSM) measurements were performed on the alumina membrane before releasing the nanowires (Figure 4.10). The shape of the axial and transversal hysteresis curves show that the magnetization easy axis is closer to the parallel direction of the NW axis, despite the competition between magnetostatic energy<sup>28</sup> (see equation 3.1, considering  $N=0$  for long NWs) which is  $157.5 \text{ kJm}^{-3}$  and cubic magnetocrystalline anisotropy  $K_1=64 \text{ kJm}^{-3}$  for a single CoNi segment.

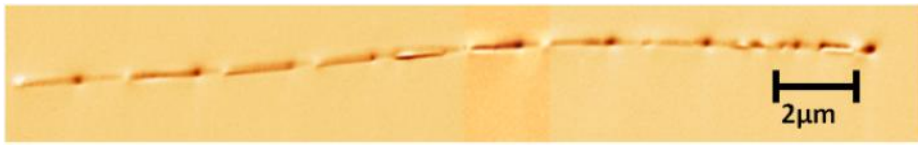
$$K_{sh} = [(1 - 3N)/4] \mu_0 M^2 \quad (3.1)$$

These values are very close and produce a soft magnetic behavior, favoring the formation of vortices.



**Figure 4.10** Normalized hysteresis loop of the NWs inside the membrane.

MFM imaging in the conventional lift mode at a constant height was performed next to investigate the domain configuration of individual NWs. An image of an entire nanowire has been reconstructed in Figure 4.11.

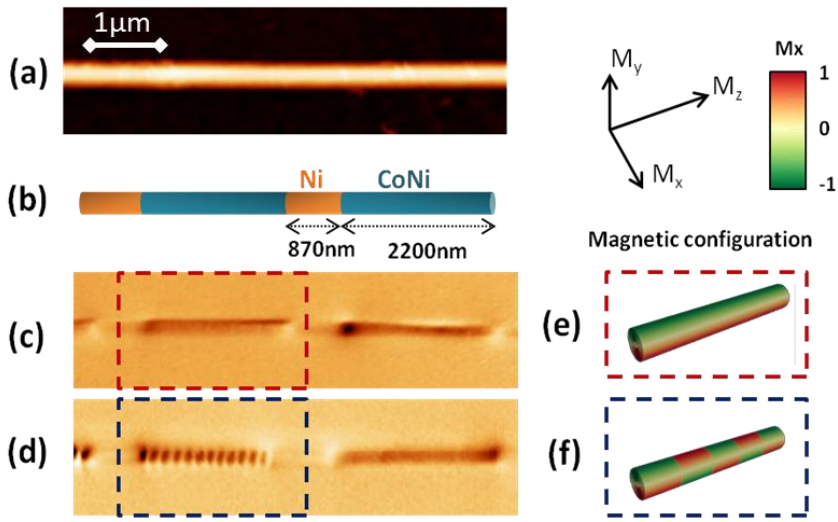


**Figure 4.11** The image of a full NW has been reconstructed from 3 MFM images. The wire was imaged in the *as prepared* magnetic state.

Figure 4.12 presents the results that correspond to the *as prepared* magnetic state of a piece of NW. Different features can be clearly distinguished. Firstly, the difference observed between the Ni and CoNi segments in the MFM signal: although in the topographic image (Figure 4.12a) both segments look identical, the MFM images (Figure 4.12c and 4.12d) reveal different magnetic configurations. On the one hand, all the Ni segments display a weaker and uniform contrast along the entire segment and, in most cases a bright-dark dipolar contrast appears at the ends of the Ni segment. Considering all this, MFM images from CoNi segments are interpreted as a single vortex with an axial core (Figure 4.12e) or a sequence of vortices of opposite chiralities (Figure 4.12f).

These MFM results are in good agreement with the single domain configuration expected for the Ni segments where the shape anisotropy, one

order of magnitude higher than the magnetocrystalline anisotropy, determines the magnetic configuration. On the other hand, contrary to the Ni segments, after performing statistics of more than 20 NWs and 80 segments, we found that the CoNi segments show two different trends.



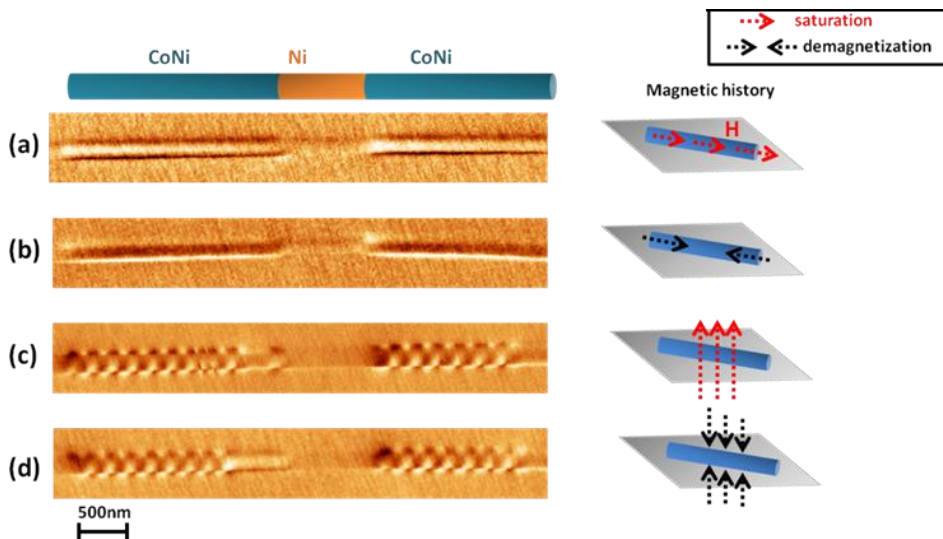
**Figure 4.12** (a) Topography, (b) geometry sketch and (c) and (d) MFM images of different NWs in as prepared magnetic state. Two different behaviours are shown by different CoNi segments. In (c) the segment in the red square shows a uniform magnetization, while in (d) a multidomain structure is displayed. (e) and (f) schematically show the expected magnetization configurations corresponding to (c) and (d) MFM images, respectively.

Some NWs display a dark/bright quasi-homogeneous contrast along the segment (see region marked with a red dashed square in Figure 4.12c). The other trend is shown in Figure 4.12d, where the magnetization of the CoNi segment breaks into domains (see region marked with a blue dashed square). Notice that due to the cylindrical shape and the size of the diameter, 120nm, the vortex configuration (with one or more vortices along the NW length) is expected for Co based NWs.<sup>1</sup>

The tight anisotropy balance of CoNi segments makes them suitable candidates to switch from one configuration to another by applying external magnetic fields. In Figure 4.13, the same piece of NW is successively exposed to magnetic fields of maximum amplitude of 18000 Oe and the remnant magnetic configuration is imaged. The region displayed in the MFM images in

Figure 4.13 corresponds to two CoNi segments separated by a Ni layer. Notice that the contrast in Ni segments keeps constant when the magnetic field changes, although the CoNi segments can develop a complex configuration.

After applying a saturating field or demagnetizing sequence (where the field switches from positive to negative values with a decreasing amplitude value) along the axial direction, see Figure 4.13a and Figure 4.13b respectively, a uniform contrast is observed in the MFM images. In addition, a dark/bright contrast appears in the lateral side of the segment. This configuration is similar to the one in Figure 4.12c and 4.12e. However, after applying a saturating magnetic field perpendicular to the nanowire axis, *i.e.* perpendicular to the magnetization easy axis, a multidomain periodic structure is again obtained in the MFM images (Figure 4.13c). Such zig-zag configuration with an alternate bright/dark contrast is analogous to the one shown in Figure 4.12d and 4.12f. Similar behaviour is found in the MFM image in Figure 4.13d obtained after exposing the NW to a perpendicular demagnetizing sequence. This observation allows us to determine the reproducibility of this complex structure.



**Figure 4.13** (a) Series of MFM images in a remnant state corresponding to the same piece of nanowire with different magnetic history after (a) applying a magnetic field of 18000 Oe in the axial direction, (b) demagnetizing in the axial direction, (c) applying a perpendicular magnetic field of 18000 Oe, and (d) demagnetizing in perpendicular direction.

### 3.3. Micromagnetic simulations

The complex configuration in multisegmented cylindrical NWs with their segments exhibiting magnetization easy axis along the nanowire, sparks new questions. Micromagnetic simulations are performed to shed light into the origin of this novel configuration and the coexistence of single and multivortex configurations, like the ones shown in Figures 4.13c and 4.13d. A three-layer CoNi/Ni/CoNi element has been considered for the following two simulations: In simulation 1, the initial magnetic configuration of the system was chosen as single vortex with the same chirality for each CoNi segment and axial magnetization for the Ni layer. The system was evolved until the minimum energy state was reached. The resulting configuration is shown in Figure 4.14a. In simulation 2, the remnant state configuration is simulated by gradually decreasing the perpendicular applied field from 18000 Oe to 0.

Two segments of  $1\mu\text{m}$  long  $\text{Co}_{65}\text{Ni}_{35}$  separated by a Ni segment of 500 nm were considered. Their diameter is 120nm and we have considered the fcc texture, grown in the  $\langle 110 \rangle$  direction as measured by HR TEM. The material parameters used for each composition are shown in Table 4.3. The magnetocrystalline anisotropy of Ni is low compared with the magnetostatic energy density, and thus, is set to zero.

For CoNi alloy, saturation magnetization was weighted regarding the stoichiometric composition with the values found in the literature.

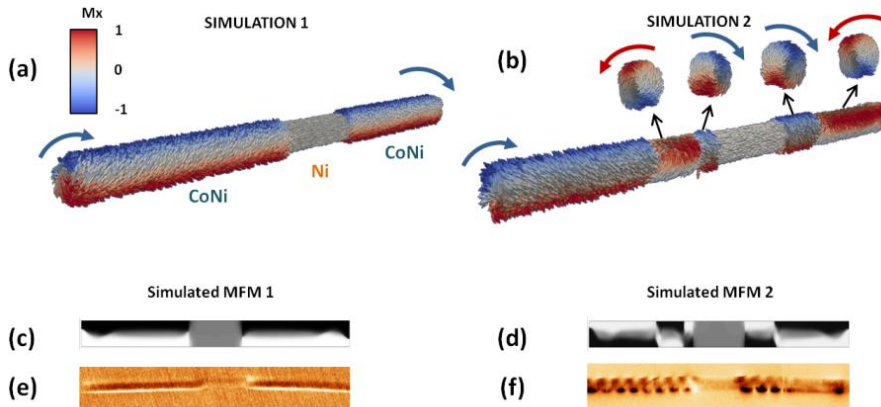
Material	$M_S$ [ $\text{A m}^{-1}$ ]	$A_{ex}$ [ $\text{J m}^{-1}$ ]	$K_1$ [ $\text{J m}^{-3}$ ]	Anisotropy
Ni	$0.48 \cdot 10^6$	$0.34 \cdot 10^{-11}$	0	None
$\text{Co}_{65}\text{Ni}_{35}$	$1.08 \cdot 10^6$	$0.45 \cdot 10^{-11}$	$6.4 \cdot 10^4$	Cubic

**Table 4.3** Parameters of the different materials used for the micromagnetic simulations.

Results show that Ni segments present always a simple axial magnetization. On the other hand, the single vortex spin configuration obtained for each CoNi segments after relaxation is a minimum energy state (Figure 4.14a). Simulation 2 shows a multivortex structure with consecutive vortices of opposite chiralities (Figure 4.14b) in the remnant state. Notice that the

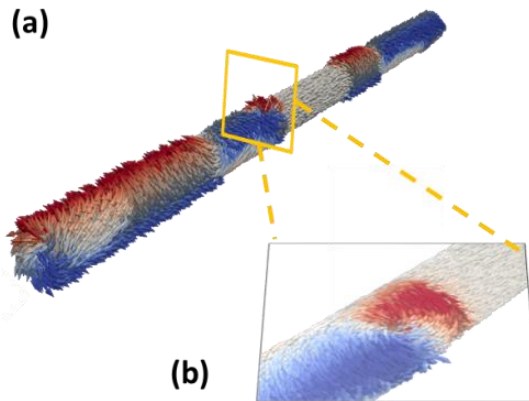


magnetic configurations of the CoNi segments are independent of the adjacent CoNi segments. The results are consistent with the configuration obtained experimentally, where the pattern of vortices is, nevertheless, periodic.



**Figure 4.14** Micromagnetic simulations show (a) a vortex along the two CoNi segments and a Ni segment with axial magnetization and (b) multivortex configurations in CoNi segments and a Ni segment with axial magnetization. In both Figures, positive and negative  $M_x$  components of the magnetization are depicted in red and blue colours and the grey colour is used for almost zero value. (c) and (d) display the corresponding simulated MFM images of the configurations shown in (a) and (b). Experimental MFM images displaying: (e) similar configuration as in (c) and (f) configuration similar to the one shown in (d).

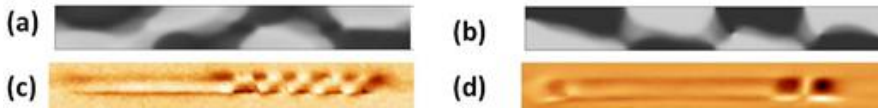
The simulations confirm that, in remanence, the magnetization of the CoNi core and Ni segments are parallel to the main axis. However, the CoNi regions present a complex magnetic configuration that tends to develop a vortex or multivortex states, as shown by the cross sections in Figure 4.14b for each vortex. It has been seen that the core of these vortices is a little bit displaced from the axis of the NW and the vortices themselves are tilted towards the anisotropy axis. Another interesting feature unveiled by the simulation is the possibility of the existence of vortices on the NW surface (Figure 4.15).



**Figure 4.15** (a) Simulated remnant configuration of CoNi/Ni/CoNi segment. (b) Inset of from (a) where a superficial vortex arises.

According to the energy values obtained with micromagnetic simulations, the multivortex state has nearly twice as much energy as the single vortex state. Despite being a single vortex energetically more favourable and therefore more common, either state is possible and can coexist in the same segment, as it has been experimentally proven (Figure 4.13d). This indicates that although the multivortex configuration represents a metastable state, it can be accessed by changing the magnetic history or stabilized by the defects.

Figures 4.14c and 4.14d display two simulated MFM images calculated from the configurations shown in Figure 4.13a and b. Considering that MFM is sensitive to the magnetization gradient, the divergence of the configuration has been represented. Coming back to the multivortex configuration, patterns with slight differences have been measured experimentally. In fact, simulations show that MFM images of multivortex segments might look different depending on the orientation of the nanowire and its easy axis with respect to the substrate. In Figure 4.16a and b, the simulated MFM image of multivortex configurations are shown, each showing a different orientation of the magnetocrystalline axis on the substrate. Below, Figure 4.16c and Figure 4.16d display experimental examples of such configurations.

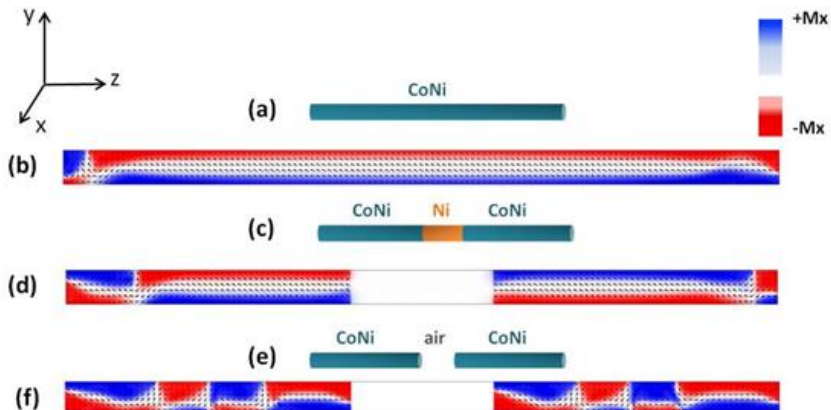


**Figure 4.16** (a) and (b) display simulated MFM images of the same CoNi segment with different orientation of the nanowire easy axis with respect to the substrate. (c) and (d) are examples of experimental MFM images of CoNi segments that present magnetic configurations similar to the ones simulated in (a) and (b).

We have to keep in mind that the anisotropy easy axis of the NWs,  $\langle 111 \rangle$  direction for fcc, is tilted  $35^\circ$  with respect to the cylinder axis. This means that since there is no axial symmetry, the MFM image might be slightly different depending on the orientation of the easy axis of the NW with respect to the substrate. This is something that is statistically expected for the experimental MFM measurements. See, for instance, the differences between Figure 4.12d and Figure 4.13b.

### 3.3.1. Multivortex configuration: Effect of the size

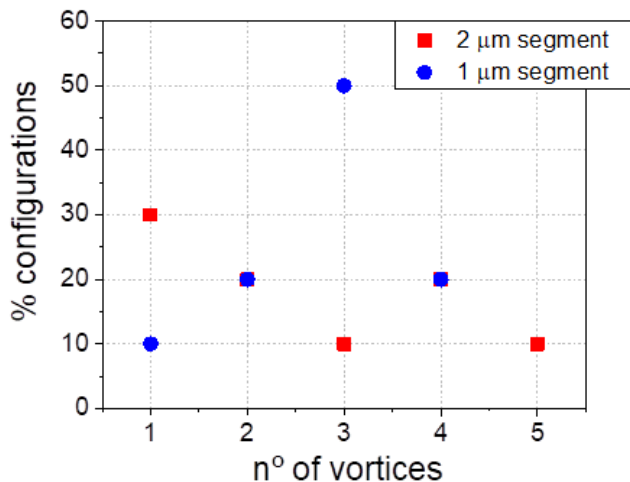
Whether Ni segments favor the formation or not of multivortex configuration is still an open question. Also the dimension of CoNi could play a role on the formation, stability and periodicity of the multivortex structure. Three simulations were performed to address this question. For all of them, an initial configuration of multivortices was chosen for CoNi, with a period of 250nm. In Figure 4.17a, a  $2.5 \mu\text{m}$  continuous NW was simulated.



**Figure 4.17** (a), (c) and (e) represent the type of simulated nanowires chosen for each simulation, where the initial magnetization is always multivortex for the CoNi segments. (b), (d), and (f) show their corresponding minimum energy configurations.

In the resulting configuration, only one out of 10 vortices (Figure 4.17b) did not annihilate. If the length of the segment is decreased to 1  $\mu\text{m}$ , the 4 vortices of the initial configuration remain. Next, a three-layer piece of NW (CoNi/Ni/CoNi) was simulated to study the effect of the presence of the Ni segment (Figure 4.17c). As shown in Figure 4.17d, the presence of the Ni segment lead to annihilation of the multivortex structure in favor of a double vortex state. Notice that in each segment, only 2 out of 4 initial vortices remain. Finally, if the Ni is substituted by a non-magnetic spacer (Figure 4.17e), the initial multivortex structure remains (Figure 4.17f).

These results seem to indicate that the multivortex configuration arises as a consequence of the size of the segment, instead of the presence of Ni. Some last simulations were performed to reinforce this statement. Several 1 and 2 microns CoNi segments were simulated with an initial random configuration, changing the random seed. The remaining energy minimum configurations are analysed and the number of vortices are quantified. In the graph below, the probability of creating from 1 to 5 vortices, in segments of 1 and 2 microns are shown. The graph in Figure 4.18 shows that for a smaller size it is more likely to develop vortices.

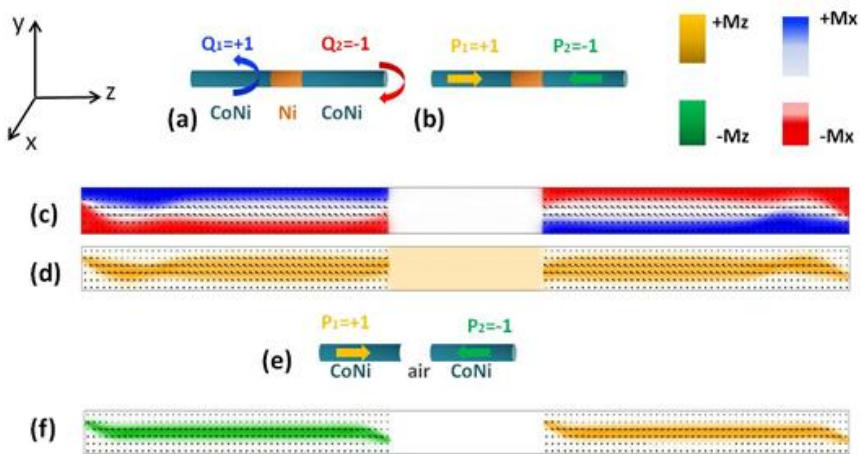


**Figure 4.18** Graph showing number of resulting vortices in simulations for 1 and 2 micron CoNi segments.

### 3.3.2. Polarity and chirality of single vortices

Conventional 2D vortices can present 4 degenerate states combining 2 possible chiralities ( $Q$ ) and polarities ( $P$ ). We want to study if our system displays the same 4 degrees of freedom as conventional vortices.

For the subsequent simulations, we follow the minimum energy configuration criteria for a three layer CoNi/Ni/CoNi NW with chosen initial magnetic configuration. As shown in Figure 4.19a and 4.19b, single vortices were initially chosen for the two CoNi segments with opposite chiralities (Figure 4.19a) or polarities (Figure 4.19b).



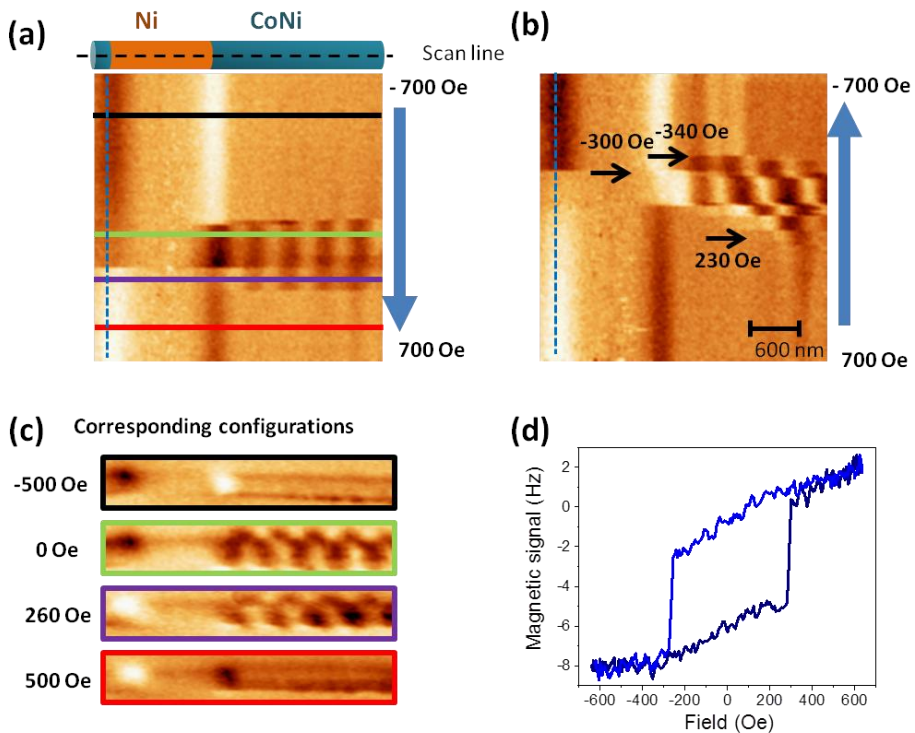
**Figure 4.19** (a), (b) and (e) show the schematic representations of the chosen initial configurations. (c), (d) and (f) display minimum energy configurations corresponding to the initial conditions in (a), (b) and (e).

The corresponding minimum energy configurations are shown in Figure 4.19c and 4.19d respectively. Since the vortices are not completely axially symmetric, we can expect some influence of the Ni segment magnetization on the vortex chirality in CoNi. However, in our simulations the presence of Ni segments does not seem to determine the chirality of the single vortices states in CoNi segments, as all the configurations ( $Q_1=Q_2$  and  $Q_1=-Q_2$ ) correspond to the energy minima. In the case of polarity, though, Figure 4.19d shows that when opposite polarities are chosen as initial configuration (Figure 4.19b), one of the CoNi segments inverts the polarity to minimize the energy.

As proven by the third simulation (Figure 4.19f) the CoNi segments are far enough to be non-interacting, and therefore, show independent polarities if the Ni layer is substituted by a non-magnetic spacer.

### 3.4. Study of domain configuration and coupling between segments under in-situ applied field.

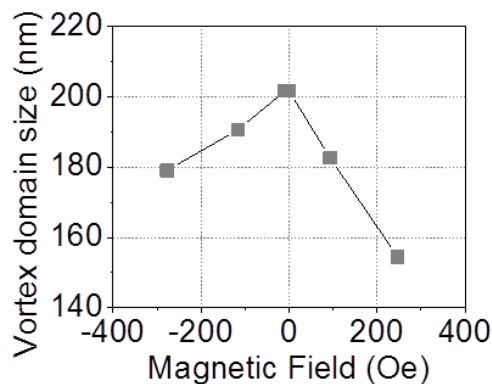
Finally, further measurements have been carried out with in situ applied magnetic field along the NWs using advanced MFM operation mode. A piece of NW with a multivortex state is chosen to track its evolution under applied magnetic fields (Figure 4.20). X scan is taken parallel to the NW axis and the top of the NW is repeatedly scanned. The magnetic field sweeps between maximum/minimum values of  $\pm 700$  Oe.



**Figure 4.20** (a) and (b) represent two branches of the evolution of the magnetization of the Ni and CoNi segments. The profiles marked in (a) correspond to the configuration measured in the MFM images obtained at that magnetic fields presented in (c). (d) Vortex domain size decreases with the positive or negative increasing field magnitude. Data extracted from images (a) and (b).

Two branches are shown in Figures 4.20a and 4.20b thus, a minor hysteresis loop is imaged. As it can be inferred, for the higher field values the multivortex configuration disappears and the configuration changes to a single vortex state with the core oriented with the field (black and red lines with their corresponding images at fixed values of the field, Figure 4.20a and 20b). This imaging mode allows us to quantify the critical fields for each configuration or reconstruct a hysteresis loop of a segment.

We observe that the multivortex configuration only exists for a narrow range of values, namely between 200 and 350 Oe (red and purple lines with its corresponding images in Figure 4.20). Although the information obtained by MFM is mainly superficial, these intermediate stages give us an idea of how the magnetization reversal takes place. In the second branch (Figure 4.20b), at 230 Oe, a couple of vortices of opposite chiralities nucleate in the CoNi segment. As the field continues sweeping, more vortices nucleate and move along the NW. Data obtained from Figure 4.20b proves that vortex domains tend to narrow when the NWs are subjected to either positive or negative increasing fields (Figure 4.21).



**Figure 4.21** Experimentally measured vortex domain size vs axial magnetic field.

In fact, when field is applied, the growth of one (or more) vortex domain is favoured at the expense of the rest, whose size decrease until they are annihilated. We need to keep in mind that CoNi segments have their magnetization easy axis tilted  $35^\circ$  from the NW axis, which makes the cores a bit slanted from the axis, and therefore, their outer magnetization have a little axial component. This fact, together with the magnetic charges of the Ni

segments, might energetically favour one particular vortex to extend while the rest decrease their size.

Another remarkable feature is that the magnetization reversal images (Figure 4.20a and b) are not fully symmetrical, since more intermediate configurations are found in the second branch than in the first one. However, in the first branch (Figure 4.20b), additional intermediate configurations might exist but presumably, some changes occur at a speed that our data acquisition timings do not make their imaging possible.

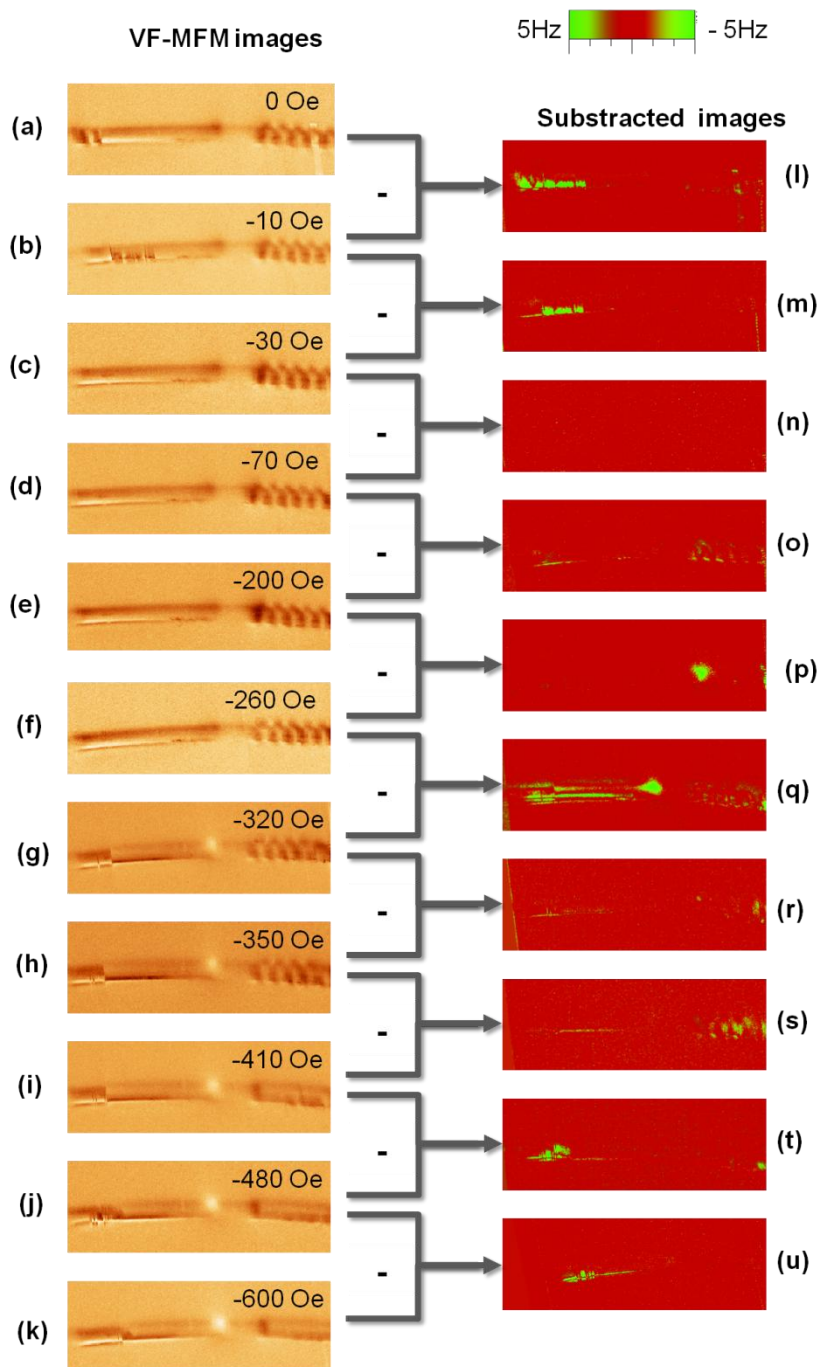
### **3.4.1. Static imaging under in-situ field.**

Detailed static VF-MFM images can provide insight into the magnetization reversal that cannot be detected through faster advanced VF-MFM measurements. In the images below a CoNi/Ni/CoNi segment is subjected to an axial field. Notice that the right part is the same piece of NW measured by non-standard MFM in Figure 4.20. Negative fields are applied to detect the configurations changes unveiled by Figure 4.20b. The field step is small, in order to detect the subtlest modifications.

At first glance, we can observe that the two CoNi segments behave differently (Figure 4.22 a-k). This might arise due to the fact that the two segments are not completely aligned with the applied magnetic field. Note that in Figure 4.22 l-u, subsequent images at decreasing fields have been subtracted to emphasize the differences between them.

This method allows us to very accurately determine the changes ongoing from one configuration to the next. Notice that in the segment on the right, the multivortex configuration remains when the field amplitude is increased. Most remarkably, from configuration Figure 4.22f to 4.22g, the axial component of the NW is switched, while no major changes occur in the multivortex configuration displayed by CoNi. The imaging shows direct evidence of the fact that polarity and chirality act independently in this complex magnetic system. Moreover, images in Figures 4.22l, 4.22o and 4.22q show evidence of the very subtle changes in the vortex domain size discussed in the main text.





**Figure 4.22** (a) - (k) present MFM images under in-situ axial applied fields. (l) – (u) are resulting subtracted images of one MFM configuration and the previous one in the sequence.

On another note, the CoNi segment on the left, hardly develops a multivortex structure (except at the first stages as shown in Figures 4.22l and 4.22m): when the field amplitude is increased, a single vortex state is achieved. Nevertheless, it reaches a double vortex structure which does not vanish under the fields we have available.

## 4. Conclusions

Using diameter modulation as a mechanism to control the magnetic configuration and magnetization reversal process is only useful when the Co-based nanowires possess axial magnetization.

Co-based nanowires usually present hcp texture. In this case, they develop vortex structures as a result of the anisotropy competition.

Tuning the composition of magnetic alloys constitutes a powerful and accessible way to control the development of one magnetic configuration or another. In the particular case of CoNi, their good lattice matching enables to the growth of good quality materials whose different magnetic features can be combined.

Multisegmented nanowires can be grown with high quality interfaces. The combination of Co and Ni has very successful results due to the similar size of their atoms. The lack of defects in the interfaces is positive from the point of view of the mechanical stability. Furthermore, for future studies of DW manipulation with currents or magnetoresistance measurements, good lattice matching is necessary to avoid oxidation at the interfaces.

It is possible to use Ni as a buffer layer to grow fcc textured Co. Generally, other materials can be used to control the crystallographic phase of the second layers in electrodeposition.

In CoNi/Ni multilayers the switching of the core is independent of the chirality of the vortices, in future works their polarity and chirality could be independently tailored.

The magnetic configuration of CoNi from the multilayer can be easily controlled with the application of relatively low magnetic fields.

The following articles have been sent for publication in relation with the work presented in this chapter:

- (1) Bran, C.; Berganza, E.; Palmero, E.M.; Fernández-Roldán, J.A.; P. del Real, R.; Aballe, L.; Foerster, M.; Asenjo, A.; Vázquez, M. Spin configuration of cylindrical bamboo-like magnetic nanowires. *J. Mater. Chem. C* **4**, 978–984 (2016).
- (2) Berganza, E.; Jaafar, M.; Bran, C.; Fernández-Roldán, J.A.; Chubykalo-Fesenko, O.; Vázquez, M.; Asenjo, A. Multisegmented Nanowires: A Step towards the Control of the Domain Wall Configuration. *Sci. Rep.* **7**, (2017).
- (3) Bran, C. Fernández-Roldán, J.A.; Palmero, E.M.; Berganza, E.; Guzman, J.; P. del Real, R.; Asenjo, A.; Fraile-Rodriguez, A.; Foerster, M.; Aballe, L.; Chubykalo-Fesenko, O.; Vázquez, M. Direct observation of transverse and vortex metastable magnetic domains in cylindrical nanowires. *Phys. Rev. B* **96**, (2017).

## 5. References:

1. Bran, C. *et al.* Spin configuration of cylindrical bamboo-like magnetic nanowires. *J. Mater. Chem. C* **4**, 978–984 (2016).
2. Berganza, E. *et al.* Multisegmented Nanowires: A Step towards the Control of the Domain Wall Configuration. *Sci. Rep.* **7**, (2017).
3. Ivanov, Y. P. *et al.* Magnetic structure of a single-crystal hcp electrodeposited cobalt nanowire. *EPL* **102**, (2013).
4. Ivanov, Y. P. *et al.* Single crystalline cylindrical nanowires-toward dense 3D arrays of magnetic vortices. *Sci. Rep.* **6**, (2016).
5. Vivas, L. G., Escrig, J., Trabada, D. G., Badini-Confalonieri, G. A. & Vázquez, M. Magnetic anisotropy in ordered textured Co nanowires. *Appl. Phys. Lett.* **100**, (2012).
6. Vivas, L. G., Yanes, R., Chubykalo-Fesenko, O. & Vazquez, M. Coercivity of ordered arrays of magnetic Co nanowires with controlled variable lengths. *Appl. Phys. Lett.* **98**, (2011).
7. Pirota, K. R. *et al.* Magnetic and structural properties of fcc/hcp bi-crystalline multilayer Co nanowire arrays prepared by controlled electroplating. *J. Appl. Phys.* **109**, (2011).
8. Cowburn, R. P. Spintronics: Change of direction. *Nat. Mater.* **6**, 255–256 (2007).
9. Jung, H. *et al.* Logic operations based on magnetic-vortex-state networks. *ACS Nano* **6**, 3712–3717 (2012).
10. Ivanov, Y. P., Iglesias-Freire, O., Pustovalov, E. V., Chubykalo-Fesenko, O. & Asenjo, A. Magnetic configurations of Co(111) nanostripes with competing shape and crystalline anisotropies. *Phys. Rev. B - Condens. Matter Mater. Phys.* **87**, (2013).
11. Jaafar, M. *et al.* Hysteresis loops of individual Co nanostripes measured by magnetic force microscopy. *Nanoscale Res. Lett.* **6**, 1–6 (2011).
12. Yan, M., Kákay, A., Gliga, S. & Hertel, R. Beating the Walker limit with massless domain walls in cylindrical nanowires. *Phys. Rev. Lett.* **104**, (2010).

13. Da Col, S. *et al.* Observation of Bloch-point domain walls in cylindrical magnetic nanowires. *Phys. Rev. B - Condens. Matter Mater. Phys.* **89**, (2014).
14. Ivanov, Y. P., Chuvilin, A., Lopatin, S. & Kosel, J. Modulated Magnetic Nanowires for Controlling Domain Wall Motion: Toward 3D Magnetic Memories. *ACS Nano* **10**, 5326–5332 (2016).
15. Bran, C. *et al.* Direct observation of transverse and vortex metastable magnetic domains in cylindrical nanowires. *Phys. Rev. B* **96**, (2017).
16. Bran, C. *et al.* Structural dependence of magnetic properties in Co-based nanowires: Experiments and micromagnetic simulations. *IEEE Transactions on Magnetics* **49**, 4491–4497 (2013).
17. Vivas, L. G. *et al.* Magnetic anisotropy in CoNi nanowire arrays: Analytical calculations and experiments. *Phys. Rev. B - Condens. Matter Mater. Phys.* **85**, (2012).
18. Talapatra, S. *et al.* Synthesis and characterization of cobalt-nickel alloy nanowires. in *Journal of Materials Science* **44**, 2271–2275 (2009).
19. Vega, V. *et al.* Tuning the magnetic anisotropy of CoNi nanowires: Comparison between single nanowires and nanowire arrays in hard-anodic aluminum oxide membranes. *Nanotechnology* **23**, (2012).
20. Kadowaki, S. & Takahashi, M. Magnetocrystalline Anisotropy of Nickel-Cobalt Alloys. *J. Phys. Soc. Japan* **38**, 1612–1619 (1975).
21. Prida, V. M. *et al.* Electroplating and magnetostructural characterization of multisegmented Co<sub>54</sub>Ni<sub>46</sub>/Co<sub>85</sub>Ni<sub>15</sub> nanowires from single electrochemical bath in anodic alumina templates. *Nanoscale Res. Lett.* **8**, 1–7 (2013).
22. García, J. *et al.* Template-assisted Co-Ni alloys and multisegmented nanowires with tuned magnetic anisotropy. *Phys. Status Solidi Appl. Mater. Sci.* **211**, 1041–1047 (2014).
23. Rosa, W. O., Vivas, L. G., Pirota, K. R., Asenjo, A. & Vázquez, M. Influence of aspect ratio and anisotropy distribution in ordered CoNi nanowire arrays. *J. Magn. Magn. Mater.* **324**, 3679–3682 (2012).
24. Mourachkine, A., Zazyev, O. V., Ducati, C. & Ansermet, J. Template Nanowires for Spintronics Applications: Nanomagnet Microwave Resonators Functioning in Zero Applied. (2008).

25. Maaz, K. *et al.* Effect of crystallographic texture on magnetic characteristics of cobalt nanowires. *Nanoscale Res. Lett.* **5**, 1111–1117 (2010).
26. Liu, Z. *et al.* Shape anisotropy and magnetization modulation in hexagonal cobalt nanowires. *Adv. Funct. Mater.* **18**, 1573–1578 (2008).
27. Reyes, D., Biziere, N., Warot-Fonrose, B., Wade, T. & Gatel, C. Magnetic Configurations in Co/Cu Multilayered Nanowires: Evidence of Structural and Magnetic Interplay. *Nano Lett.* **16**, 1230–1236 (2016).
28. Coey, J. *Magnetism and magnetic materials. Physics* **12**, (2010).





## **APENDIX B: Protocol for nanowire deposition onto substrates for their individual study**

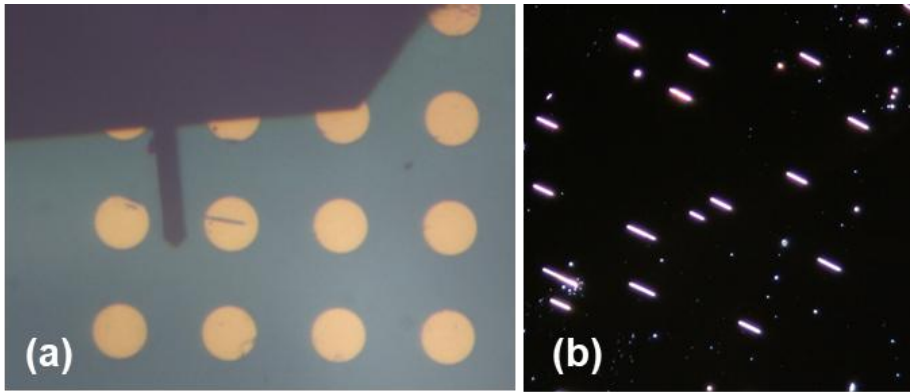
The characterization of individual NWs thorough MFM entails certain difficulties that had to be faced along this thesis. Different experiments led to new requirements in the preparation of the sample, which eventually took us to develop a general protocol for the preparation of the NWs onto substrate with the aim to optimize the measurement time and resources.

### **1. Growth of markers on substrates**

For the study of individual elements, the deposition of the nanowires onto substrates –generally silicon- is a key step. Depending on the type of experiments, a particular preparation of the substrate might be required. In section 3.2 of Chapter 4, for instance, the same nanowire is localized and imaged after removing the sample from the holder to subject it to high external magnetic fields. For different reasons, one might need to come back to image the same nanowire after changing certain conditions. Generally, the nanowires can be barely seen though the optical microscopes coupled to the AFM systems. It is therefore a good idea to use marked substrates available in the market (or home-made ones) where one can distinguish different areas. Photo lithographed home-made marked substrates have been used along this thesis, following the subsequently explained preparation procedure: i) a drop of the positive photo resist is spread though spin coating over the substrate with a speed of 5000 rpm (ii) the substrate is covered with a mask containing the chosen pattern and it is exposed to ultra-violet (UV) light which turns the exposed areas soluble. (iii) For one minute the substrates are deepened into the revelator and (iv) an oxygen plasma etching ensures good definition of the patterns. (v) Chromium –or any other metal- is sputtered and (vi) the remaining of the resist are eliminated through a three step RCA cleaning process.<sup>1</sup> The preparation of the substrates was carried out together with Á. Garcia, the person responsible for the clean room facility of the ICMM-CSIC.

Once the substrates are ready, a drop of ethanol containing magnetic nanowires is placed on them by spin coating, to avoid aggregation. It is highly advisable to use a big enough sample holder for this, where the substrate can be positioned off center to facilitate the alignment of the NWs with the

tangential acceleration direction. This step helps saving time during *in-situ* applied field measurement, where the field direction in the setup is fixed and nanowires need to be aligned with it. In Figure B.1a an example of marked substrates with NWs spread over it are shown. The image was performed with the optical microscope integrated in the AFM system, and the end of the chip and cantilever can be seen. The image shown in Figure B.1b was performed with an optical microscope working in the dark field mode. The dark field mode has been proven to be a very powerful tool to localize NWs onto the substrate, if one needs to measure or manipulate specific NWs. Its high sensitivity to small height changes in the sample provides much better defined images than the standard operation mode.



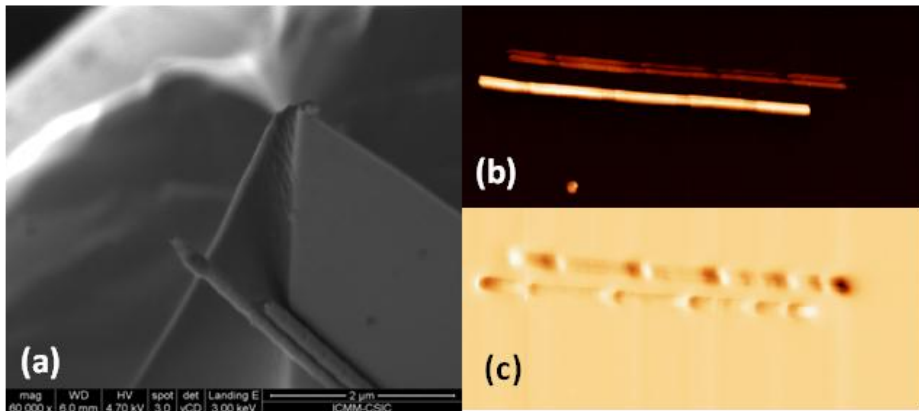
**Figure B.1** Optical microscope images (a) of a silicon substrate with Chromium markers to help us localize NWs for MFM measurements. (b) Nanowires spread onto a silicon substrate (dark field mode).

## 2. The double tip issue

Another inconvenience that has been found throughout this thesis is the high affinity between the tip magnetic coating and the nanowires. Despite the electrostatic force and the traces from the dissolution that help to maintain the NWs fixed to the substrate, the high stray field of the tips, together with the high magnetization of several types of nanowires, facilitates the detachment of the NWs from the substrate and posterior attachment to the tip.

The result of getting a nanowire attached to the MFM tip is shown in Figure B.2. As it can be seen in the SEM image, the nanowire and the apex of the tip are in this case separated a few microns, which gives rise to two well

separated nanowire complementary images –notice that the tip and nanowire are magnetized in opposite directions-. In other cases, though, NWs are fixed closer to the tip apex and the acquired MFM images can be misleading, as it might not be so obvious to the user that a double tip is present.



**Figure B.2** (a) SEM image of a MFM commercial tip with two hanging ferromagnetic nanowires. Resulting (b) topographic and (c) MFM image of one NW with the double tip.

To prevent the NWs detaching from the substrate, three solutions have been explored along this thesis to immobilize the NWs.

### 2.1. Covering the NWs with graphene.

In the first place, a silicon substrate with high density of nanowires needs to be prepared. Then, exfoliated graphene is transferred to the prepared sample (Figure B.3).<sup>2</sup> Through optical microscopy it can be verified that there are enough graphene flakes covering nanowires, and that those flakes are sufficiently large so that lifting them is unlikely. This method has been developed in collaboration with Dr. Pablo Ares and Prof. Julio Gomez-Herrero from the Universidad Autónoma de Madrid.

The main drawback of this method is the difficulty of preparation. Graphene flakes need to be exfoliated in such a way that we have a high density of as much monolayers (or very few layers) as possible and that are sufficiently large. Then, the flakes need to be transferred to our sample, which complicates the things even more. In return, it is a cheap method that can be used set an electrode to a particular NW for the exploration of the electric

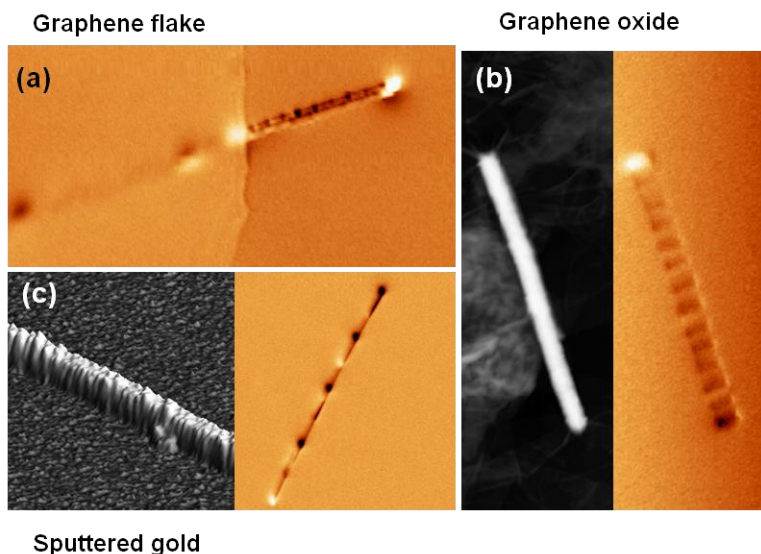
properties of the specimens,<sup>3</sup> in addition to fixing the nanowires to the substrate.

## 2.2. Covering the NWs with GO

Following the same philosophy, a sample with high density of NWs can be covered with graphene oxide sheets. This makes the preparation of the sample much easier, since GO can commercially be acquired in a solution and a tiny drop of it is enough to cover part of the substrate with very thin (monolayer) sheets. Figure B.3b demonstrates how the presence of GO is obvious in the morphological image, although it does not screen nor alter the magnetic contrast. In this case, using a SiO<sub>2</sub> substrate is advisable, because GO can very well be distinguished on it looking through an optical microscope.

Despite being a quick method, its main drawback is the random deposition of the flakes and the lack of control over which nanowires which are covered. At the same time, GO is an insulator and therefore “hides” the electrical properties of the nanowires.

## 2.3. Sputtering a few nm metallic layer



**Figure B.3** (a) Nanowire covered with a few layers of graphene. (b) Topographic & MFM images of a nanowire covered with a few GO monomolecular sheets & corresponding MFM image. (c) 3D morphological image of a nanowire with 30nm of sputtered gold & its corresponding MFM image

A third solution is proposed to overcome the previous difficulties, which consists of sputtering around 30nm of a metallic layer, which in our case was done with gold. The gold quantity can be selected according to the NW diameter. It needs to be considered that the more gold quantity, the bigger attachment to the surface, but at the same time, magnetic resolution becomes poorer as we measure further from the nanowire (See Figure B.3c)

This represents a controllable solution where all nanowires are covered at once, but in some cases, solution (2) might be better, specially, when spatial resolution is critical.

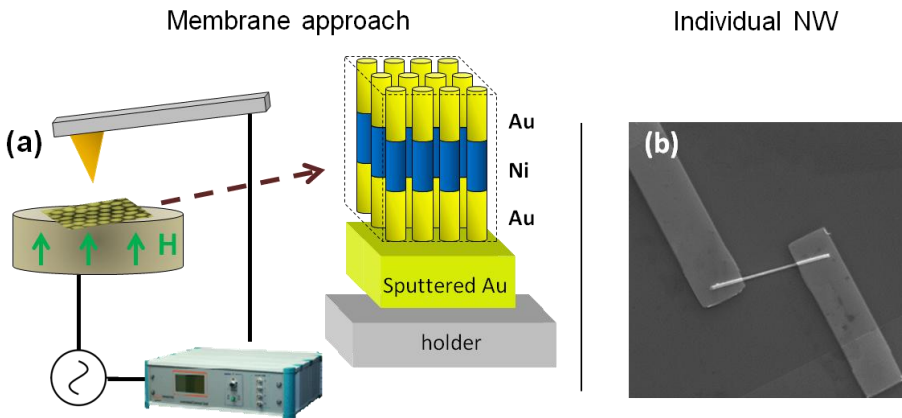
## References

1. RCA cleaning. Available at: <https://www.inrf.uci.edu/wordpress/wp-content/uploads/sop-wet-silicon-rca-1.pdf>.
2. Castellanos-Gomez, A. *et al.* Deterministic transfer of two-dimensional materials by all-dry viscoelastic stamping. *2D Mater.* **1**, (2014).
3. Ares, P. *et al.* Exfoliated graphite flakes as soft-electrodes for precisely contacting nanoobjects. *2D Mater.* **2**, (2015).

## APENDIX C: Preparation of nanowires for magnetoresistance measurements

The control of the domain wall propagation via spin-polarized currents is the ultimate goal of data storage technologies based on encoding information in domain walls.<sup>1</sup> For this reason, a few groups have devoted efforts to the study of magnetotransport properties of cylindrical nanowires.<sup>2,3</sup>

This appendix is focused on the two methods have been explored for the realization of electrical measurements on magnetic nanowires. In the first approach, nanowires embedded in membranes are utilized.<sup>4</sup> As illustrated in Figure C1a, multisegmented nanowires are grown with gold layers at both endings. In the bottom part of the alumina, the sputtered gold used as an electrode for the electrodeposition with serve as an electrode for electric measurements too and can be contacted to a power supply. The second electrode is a conductive tip, which closes the circuit as it gets into contact with the nanowire.



**Figure C.1** (a) Sketch of circuit configuration and the nanowires in membrane mounted on the sample holder of an AFM system with a coil to apply OOP magnetic field. (c) Single nanowire on a isolating substrate with individual contacts. Taken from [ref5].

The second approach, consists of spreading the NWs onto an isolating substrate and growing individual microscopic contacts to one of them.<sup>6</sup>

## 1. Membrane approach

To perform electrical measurements in nanowires embedded in alumina membranes, after electrodeposition the top part of the alumina needs to be polished until the nanowires rise above the membrane. This whole preparation process was carried out by the group of Dr. Prida in the University of Oviedo.

To look for the right choice of the tip has been a laborious work, four conducting tips were tried (details in table C.1) and only one of them worked correctly. The main difficulty of this sample is the combination of two materials with very different mechanical properties. The few nanometers gold layer is rather fragile. Furthermore, due to the hydrophilic nature of gold, it is advisable to clean it using oxygen plasma before measuring. On the other hand, the alumina is mechanically robust but rather aggressive with the tip coating.

company	Name	Nominal k (N/m)	Tip	Coating
Budget Sensors	Multi75E-G	3	Si	Cr/Pt
Rocky mountain	25Pt300B	18	Pt	None
Rocky mountain	25Pt400B	8	Pt	None
Rocky mountain	12Pt300B	0.8	Pt	None

**Table C.1** Conductive tips used in the attempt of contacting NWS.

As a first approach, a Cr/Pt coated standard AFM tip (3N/m) from Budget Sensors was used to measure the topography. When a suitable area of nanowires is found, the tip approaches the center of a particular nanowire, performing a force-distance curve (FZ). At the same time, a bias voltage sweep is performed to study the electrical response of the NW. However, due to the abrasive nature of the alumina, the gold coating suffers and the tip loses its conduction properties. Since we failed to achieve good mechanical contact, the tip and cantilever had to be changed.



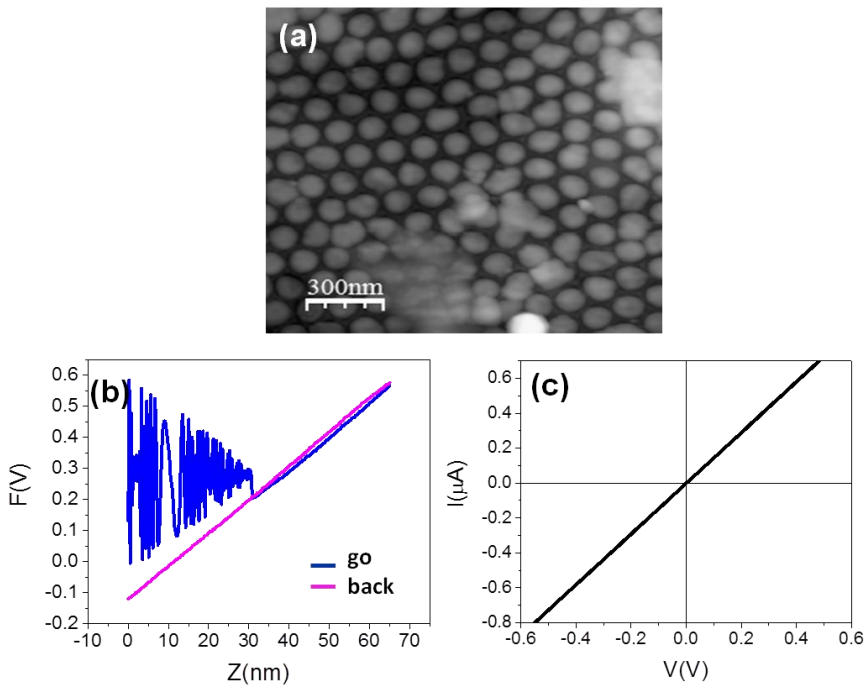
As a next step a fully platinum tip from Rocky Mountain was tried, to avoid coating degradation. A higher force constant tip was selected (40N/m) to improve the mechanical contact. However, after mapping different areas of the sample, we realized that the tip was destroying the nanowires just by scanning, even with very small oscillating amplitude values.

A new kind of tip of Rocky Mountain of 8N/m constant was tried. This tip resulted to be the only successful tip to perform topographic images as well as several IV curves in different nanowires. A softer tip of the similar properties (0.8N/m) was also tried, but although topographic images were good enough, no IV curves were obtained. Therefore, a good compromise in terms of applied force was obtained with the 8N/m tip. The inverse of the slope of the IV curve (Figure C2.c) is the overall resistance value  $R_{tot} = 75 \times 10^4 \Omega$ , which includes the NW resistance, contact resistance, tip resistance, etc.

$$R_{tot} = R_{tip} + 2R_{Au} + R_{Ni} + R_{contact}$$

Notice that although it is four magnitude orders higher than the calculated resistance for a Niqel NW (76.39  $\Omega$ ) due to the high contact resistances, the shape of the curve is that of an ohmic contact.

This part remains as an open line of this thesis, but the path has been opened to perform measurements with OOP applied field. Additionally, if the top gold layer is short enough (below  $\sim 125\text{nm}$ ), MFM contrast could be also measured, to characterize the response of the individual nanowires to OOP field and current.

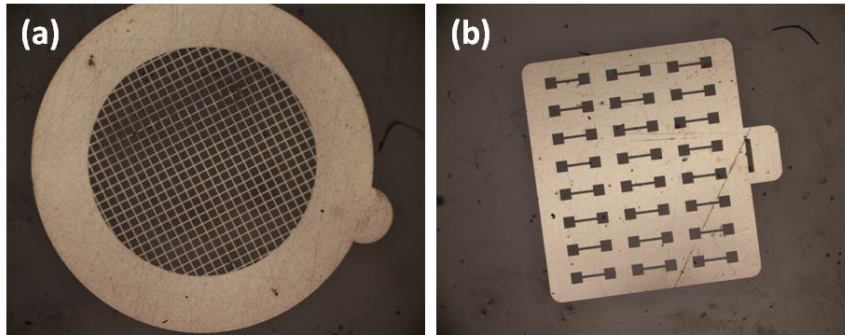


**Figure C.2** (a) Topographic images of the nanowires coming out from the membrane. (b) FZ curve to contact a nanowire with the tip. (c) IV curve performed with 8 N/m tip from Rocky Mountain.

## 2. Individual nanowire approach

Many groups have addressed the task of contacting individual nanowires to perform magnetoresistance measurements. Most of the contacting processes that the authors follow, involve very laborious work in clean room facilities with very expensive lithography equipment.

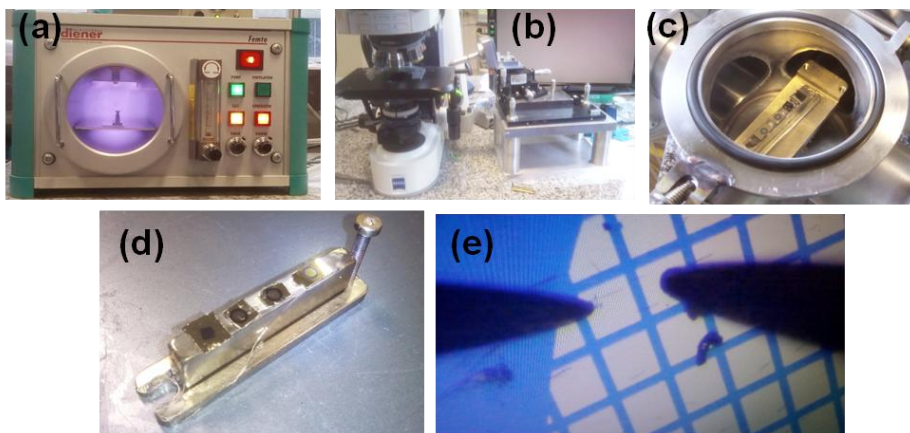
In this work, developed in the laboratories of Universidad Autónoma de Madrid in collaboration with the group of Prof. J. Gómez-Herrero, a cheap method for nanowire contacting is presented, which can be carried out in any standard laboratory. It consists of evaporating an electrode, using a mask (Figure C.3) with a repeated pattern that is placed over the sample with micromanipulator.



**Figure C.3** Two types of masks used for contacting NWs. The gaps are 10 µm big in (a) and 3 µm big in (b).

### 2.1. Mask lithography method

First, nanowires are prepared onto a  $\text{Si}_2\text{O}$  substrate following the protocol that has been described in the Appendix B. Having the nanowires spread on a marked substrate permits to characterize them via AFM or MFM to choose an appropriate nanowire for the study (i.e. a nanowire with a domain wall or any other desired feature).

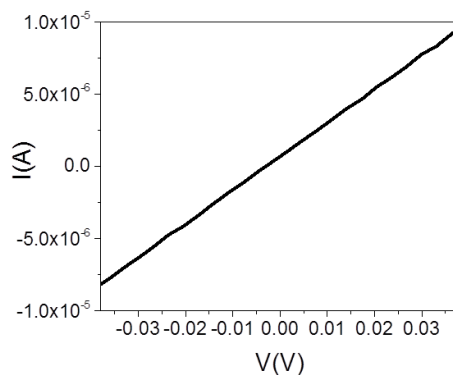


**Figure C.4** (a) Sample in the chamber subjected to hydrogen plasma. (b) Optical microscope with the micromanipulator in the right. (c) Vacuum chamber with the magnet and the samples mounted on it. (d) Magnet with samples after evaporation. (e) Sample with electrodes being measured on the probe station to check conductivity.

To make a good electrical contact, removing the native oxide of the NWs is a key step. This can be done subjecting the nanowire to hydrogen plasma for a few minutes (Figure C3a), although after many attempts, it was concluded that *in-situ* plasma was necessary to prevent the oxidation of the NW surface. Therefore, an argon plasma bottle was coupled to the chamber and the sample was subjected to ignited plasma for 10 minutes.

The sample substrates are mounted on a NdFeB magnet (Figure C.3d) to fix ferromagnetic masks. The masks are thus immobilized once they are in the right position. They are placed randomly onto the substrates and using a micromanipulator (Figure C.3b) and an optical microscope, they are dragged into the right position. Subsequently, the magnet with the samples is carefully transferred to the vacuum chamber, where (i) the nanowires are subjected to argon plasma to get rid of the oxide, (ii) a chromium or titanium layer of about 5nm is evaporated onto the sample in order to optimize the adhesion of the electrode to the substrate and finally (iii) a gold layer of 80nm is grown. (pressure  $10^{-6}$ , power source 12V, deposition rate 1A7s Au, 3A/s Cr).

When the gold electrodes are ready, the sample is taken to a probe station to verify if there is electrical contact between the nanowire and the grown electrodes (Figure C.3e).



**Figure C.5** Electric response of the contacted Ni NW to applied voltage, measured in the probe station.

In conclusion, a device has been built consisting of a Ni nanowire with two electric contacts, which serves as a probe of concept that verifies the applicability of the mask lithography method to contact magnetic nanowires.

## References

1. Parkin, S. S. P., Hayashi, M. & Thomas, L. Magnetic domain-wall racetrack memory. *Science* **320**, 190–194 (2008).
2. Ivanov, Y. P., Chuvilin, A., Lopatin, S., Mohammed, H. & Kosel, J. Direct Observation of Current-Induced Motion of a 3D Vortex Domain Wall in Cylindrical Nanowires. *ACS Appl. Mater. Interfaces* **9**, 16741–16744 (2017).
3. Böhnert, T., Vega, V., Michel, A. K., Prida, V. M. & Nielsch, K. Magneto-thermopower and magnetoresistance of single Co-Ni alloy nanowires. *Appl. Phys. Lett.* **103**, (2013).
4. Chiriac, H., Dragos, O. G., Grigoras, M., Ababei, G. & Lupu, N. Magnetotransport phenomena in [NiFe/Cu] magnetic multilayered nanowires. in *IEEE Transactions on Magnetics* **45**, 4077–4080 (2009).
5. No Title. Available at: <http://www.infim.ro/projects/insect-odorant-binding-proteins-conductive-polymer-nanofibers-based-biosensor-diagnose-crop>.
6. Mohammed, H., Vidal, E. V., Ivanov, Y. P. & Kosel, J. Magnetotransport Measurements of Domain Wall Propagation in Individual Multisegmented Cylindrical Nanowires. *IEEE Trans. Magn.* **52**, (2016).

# **CHAPTER 5**

**Magnetic soft nanoparticles:**

**From vortices to  
skyrmions**

By scaling down one, two or three dimensions of nanoobjects one can play with the aspect ratio and give rise to magnetic configurations of very different nature. From thin films (2d materials), going through nanowires (1D materials) we get to magnetic nanoparticles, considered as zero dimensional nanoobjects, which are the subject of study of the present chapter.

In the smallest possible magnetic systems, there is literally no room for multiple domain creation. In such cases, as a result of the interplay between the different energy terms, the absence of domains gives rise to compelling spin textures.

In this regard, systems with topological defects have attracted much attention due to their rich physics that serve as extensible models for condense matter systems beyond the scope of magnetism. A topological whirl is a region of singular field distribution, which mathematically represents a soliton solution of a field described by a partial differential equation. Vortices, which have been introduced in Chapter 1, can be considered as Bloch skyrmions (of winding number  $\frac{1}{2}$ , instead of 1).

In this part, sub-100 nm soft nanodots have been studied, where magnetic hedgehog skyrmions have been detected despite the absence of Dzyaloshinskii-Moriya interaction (DMI) or perpendicular magnetocrystalline anisotropy (PMA). At least one of them is considered a necessary ingredient for their creation. These results are compared to conventional vortices, obtained in similar nanodots with a bigger radius. An additional study of their stability has been conducted, both theoretically (assisted by micromagnetic simulations and analytical calculations carried out by Prof. K. Gusliyenko, from the Ikerbasque Research Foundation) and experimentally.<sup>1</sup>

All samples were fabricated by Dr. M. Goiriena-Goikoetxea and Dr. A. García-Arribas in the University of the Basque Country for an ongoing collaboration.



## 1. Magnetic nanoparticles

The study of nanometric size magnetic particles has been an active topic of research over the last years.<sup>2</sup> Their broad spectrum of industrial applications leads to groups of very different backgrounds to interact in the search of the optimal properties for each particular application. In-vivo applications<sup>3,4</sup> require stable particles in neutral pH plus non-toxic composition. In biomedicine, superparamagnetic nanoparticles<sup>5,6</sup> are generally needed (no remanence in absence of applied field) at room temperature to avoid dangerous consequences coming from particle aggregation inside the body. In data storage technologies<sup>7</sup> conversely, stable magnetic configurations are mandatory to guarantee non-volatility of the data under thermal fluctuations.

The characterization of individual NPs constitutes a challenge due to the resolution limitation of imaging techniques, together with the low magnetic signals emerging from such small NPs, typically iron oxides studied for magnetic hyperthermia. Stretching the limits of the existing tools entails the development of more sophisticated measuring strategies.<sup>8,9,10,11</sup>

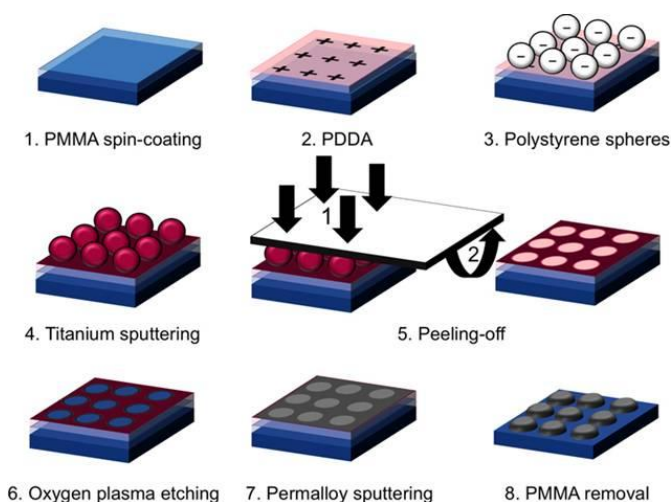
Likewise, the growth of nanometric homogeneous particles is generally addressed by chemical synthesis methods.<sup>12,13</sup> Amongst other advantages, the chemical route offers big versatility in the output in terms of size, shape and surface coatings and allows optimizing them for specific functionalities.<sup>14</sup> On the other hand, conventional lithography based techniques generally still lack of high yield capacity, which complicates its implantation for mass production. Given this drawback, some groups have implemented physical top down methods<sup>15</sup> as an alternative approach for NP fabrication,<sup>16,1</sup> combining higher yield lithography based techniques with common material deposition techniques, such as sputtering or evaporation. The use of porous alumina membranes as templates,<sup>17,18</sup> nanosphere lithography<sup>19</sup> or hole mask colloidal lithography (HCL)<sup>20</sup> enables the growth of homogeneous curved nanostructures.

As explained in the first chapter of this thesis, soft magnetic nanodisks have been widely investigated since the first experimental evidence of the spin-vortex<sup>21</sup> was obtained in 1999. Pioneer works were performed in

disks of nanometric thickness, but most of the times their diameter was still in the micron scale length. However, due to the successful

improvement of the ahead mentioned lithography based techniques, Goiriena et al. recently published a work on the high yield fabrication of small permalloy nanodots,<sup>20</sup> which opened the path to the study of these nanostructures through various imaging techniques, facing the challenge of the resolution limits being very close. The study of small sized nanodots represents not only a big challenge from the instrumental viewpoint, but it has also resulted to provide unexpected magnetic behavior with compelling consequences. All previous works so far point at the formation of vortex or single domain magnetic configurations in soft nanodots with diameters below 100 nm,<sup>22,23,1</sup> while measurements presented in the following part are indicative of the creation of topologically complex spin textures.

## 2. Fabrication through Hole-mask Colloidal Lithography Morphological characterization



**Figure 5.1** Steps for sample fabrications via Hole Mask Colloidal Lithography. Taken from [ref.20]

The samples were fabricated through Hole-mask colloidal lithography (HCL).<sup>20</sup> This method involves three main steps: first, a short-range-ordered polystyrene (PS) nanosphere array is formed onto a poly methyl

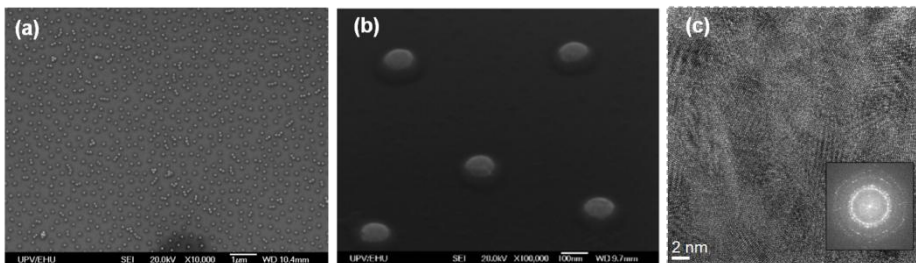
methacrylate (PMMA) polymeric layer. Subsequently, titanium is sputtered onto the system before the spheres are peeled-off and the exposed PMMA etched in oxygen plasma, leaving an array of holes as a template for the nanodot growth. Finally, permalloy is sputtered with a DC magnetron sputtering to fill the pores and grow the nanodots, while the PMMA is removed with acetone, remaining only the nanodots onto the silicon substrate (See Figure 5.1).

The chapter is focused on the study of 35 nm radius nanodots (sample Py1), although two sample of different sizes (Py2 and Py3) were additionally utilized for comparison. Table 5.1 gathers the radius (R) and thickness (T) of the three samples.

Sample	Py1	Py2	Py3
Radius (nm)	36	30	70
Thickness (nm)	35.5	31.3	50

**Table 5.1** Parameters of the 3 samples measured along this chapter.

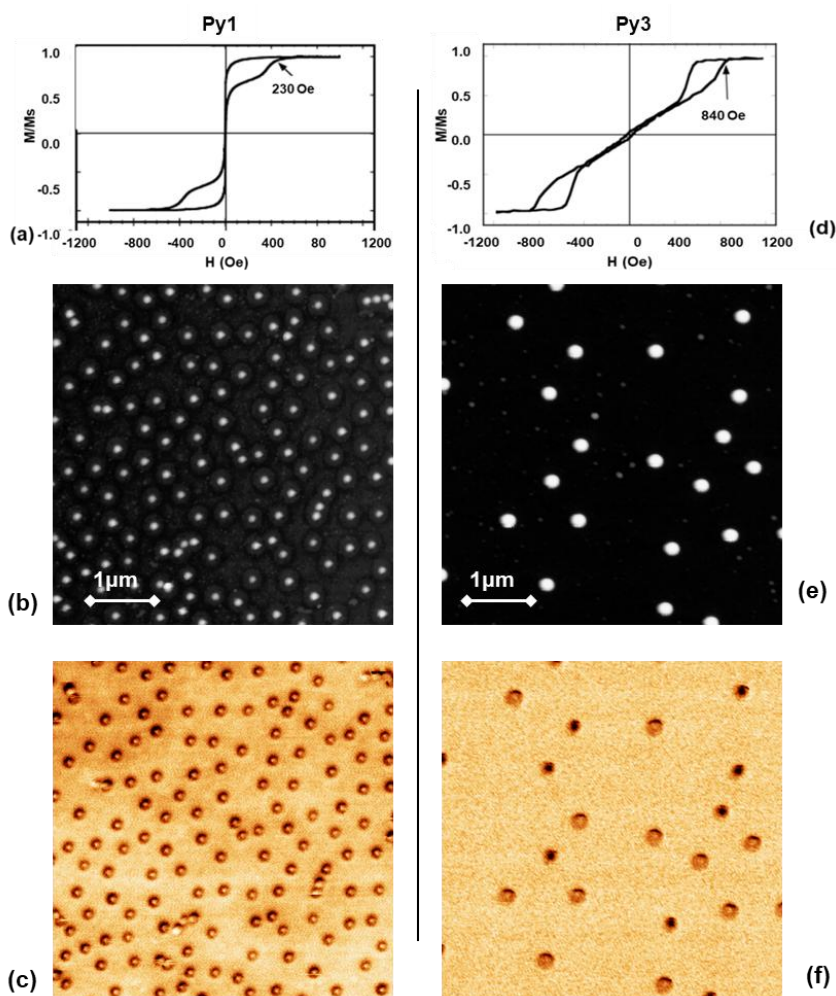
Generally, the nanodots studied are distributed onto a silicon substrate far enough from neighboring nanodots in such a way that they can be considered non-interacting with each other (see Figures 5.2a and b). Their shape and size were assessed by Scanning Electron Microscopy (SEM) and High Resolution Transmission Electron Microscopy (HR-TEM) which confirmed the polycrystalline nature and therefore, the absence of magnetocrystalline anisotropy (Figure 5.2c) in the Py nanodots.



**Figure 5.2** Scanning Electron Microscope (SEM) top view image of (a) sample Py1 and (b) sample Py3. (c) TEM image zoom of the cross section of typical hemispherical shaped nanodots of the sample Py1 and its corresponding Fast Fourier Transform in the inset.

### 3. Study of the magnetic configuration of big and small nanodots

As a first approach, a sample with small diameter (Py1) was compared to the sample with biggest diameter (Py3). Looking at their hysteresis loops (Figure 5.3a and b), it can be concluded that bigger nanodots show a typical vortex hysteresis loop, while smaller nanodots display a loop which despite being compatible with the vortex configuration (due to the lobes near saturating fields), they differ a bit in the overall shape.



**Figure 5.3** Hysteresis loops of (a) Py1 and (d) Py3 samples. Topographic image of (b) sample Py1 and (e) sample Py3, showing the distribution of the permalloy nanoparticles on the silicon substrate. (c) and (f) display the corresponding Magnetic Force Microscopy images.

In view of these results, MFM imaging was performed on samples Py1 and Py3 to study their magnetic configuration. Several measurements were repeated, changing the magnetic state of the sample by applying ex-situ saturating fields (18000 Oe).

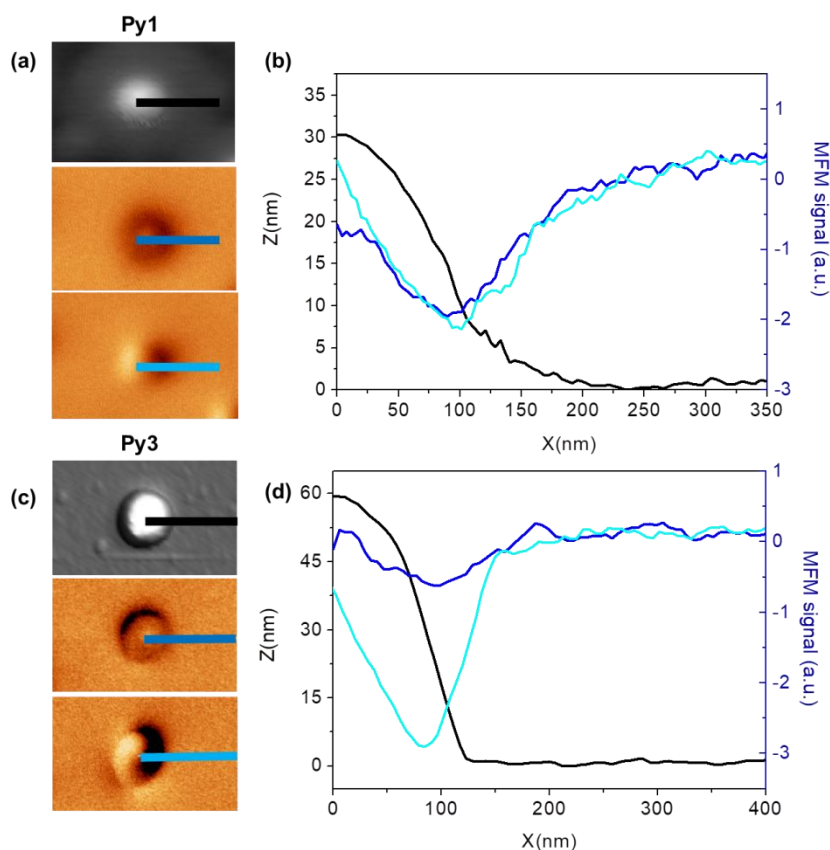
To image sample Py1, different tips were used, until it was concluded that the magnetic configuration was independent of the tip used to image (evidence of this fact is shown later), conversely to sample Py3, where the use of a lower moment tip was required to avoid artifacts coming from the commercial tip stray field influence, as explained in section 3.1 of Chapter 2. The MFM images shown in Figure 5.3 were performed after the sample was demagnetized.

Interestingly, both sample configurations (see Figure 5.3c and f) resemble to vortices since a core is distinguished from the surrounding area. As mentioned in Chapter 1, vortices present in-plane closed-flux magnetization with a divergence at the centre, where the magnetization can be either positive or negative and their chirality can be clock or anticlock-wise.<sup>24,25,8</sup>

To analyse in depth the differences between both samples, the MFM contrast in two different magnetic configurations is plotted. However, we can clearly see that in remnant state the MFM signal corresponding to the bigger nanodots (Py3) is not as intense as that of sample Py1 (Figure 5.4a and b).

Whereas sample Py3 displays a faint contour, characteristic of *in-plane* magnetization (whose intensity is much lower than that of the dipolar contrast), sample Py1 presents a contrast compatible with higher out-of-plane component of the magnetization.

So far, we can conclude that bigger nanodots (Py3) behave like classical vortices, despite presenting large cores,<sup>1</sup> while the MFM contrast observed in smaller nanodots (Py1) seems to be more compatible with skyrmion configurations, with core and contour having opposite out-of-plane magnetization direction.

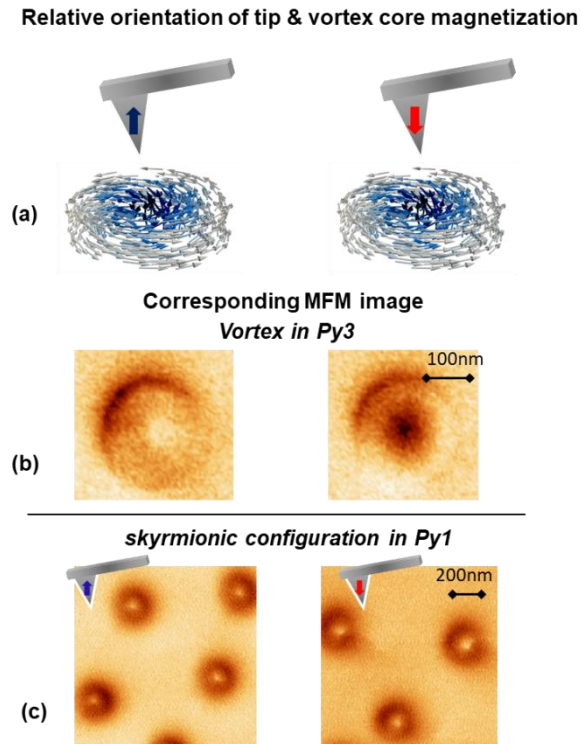


**Figure 5.4** Topographic and MFM images in remnant (light blue) and nearly saturated states (dark blue) of (a) sample Py1 and (c) sample Py3. Their corresponding profiles are depicted in (b) and (d).

On the other hand, while image 5.3f displays vortices of random polarities (light and dark cores), in Figure 5.3c, all cores are white, despite having demagnetized the sample. To address this question, perpendicular saturating fields were applied to the two types of nanodots.

We recall that dark (or bright) core contrast corresponds to attractive (or repulsive) interaction i.e. to parallel (or antiparallel) configuration to the tip polarization. Thus, the core contrast will reverse by switching either the magnetization of the tip or the polarity of the core. As expected, the vortices from Py3 sample present a regular behavior: once their polarity is fixed, the contrast changes depending on the tip polarity. However, in sample Py1 the contrast at the center of the nanoparticles is always positive (corresponding

to an antiparallel tip- core configuration, see figure 5.5c) regardless of the MFM probe polarization.



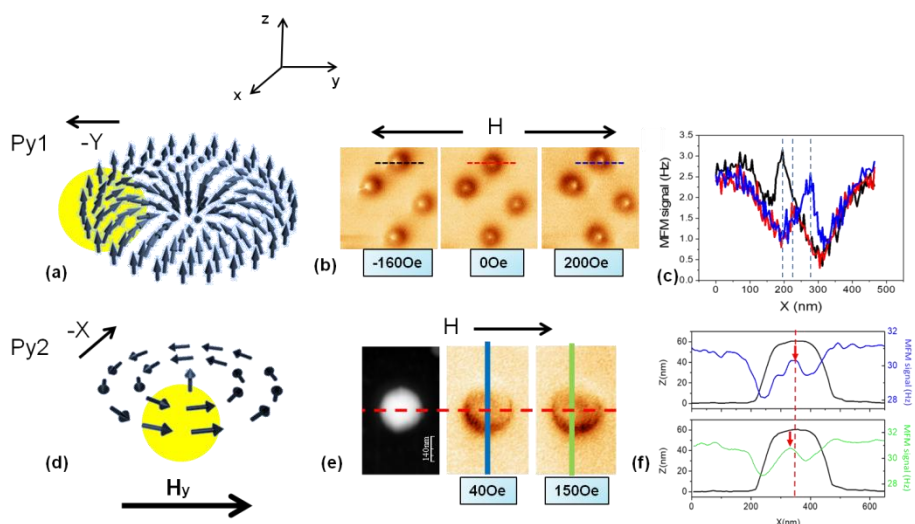
**Figure 5.5** (a) Two possible configurations of the MFM tip giving rise to a different MFM contrast for a vortex with the same polarity. (b) MFM images of Py3 nanodots, where the opposite contrast in the core is only due to an opposite magnetization configuration of the MFM tip. (c) MFM images of nanodots performed with different tip polarities where the magnetic contrast remains the same (Py1).

#### 4. Response to magnetic in-plane field

In view of the non-standard data obtained in the small nanodots, Variable Field (VF)-MFM<sup>27</sup> measurements were carried out. We have to keep in mind that the fingerprint of the vortex spin texture is the perpendicular displacement of its core with respect to an IP applied magnetic field, until the moments completely align with the in-plane field.

For Bloch skyrmions, as for vortices, the core displacement when IP magnetic field is applied depends solely on the skyrmion chirality sign ( $m_\phi$ ). In the case

of Néel skyrmions conversely, the radial component direction sign ( $m_\rho$ ) determines the displacement. See Figure 5.6a and d, where the region that expands when  $H_y$  field is applied has been marked in yellow for each case.



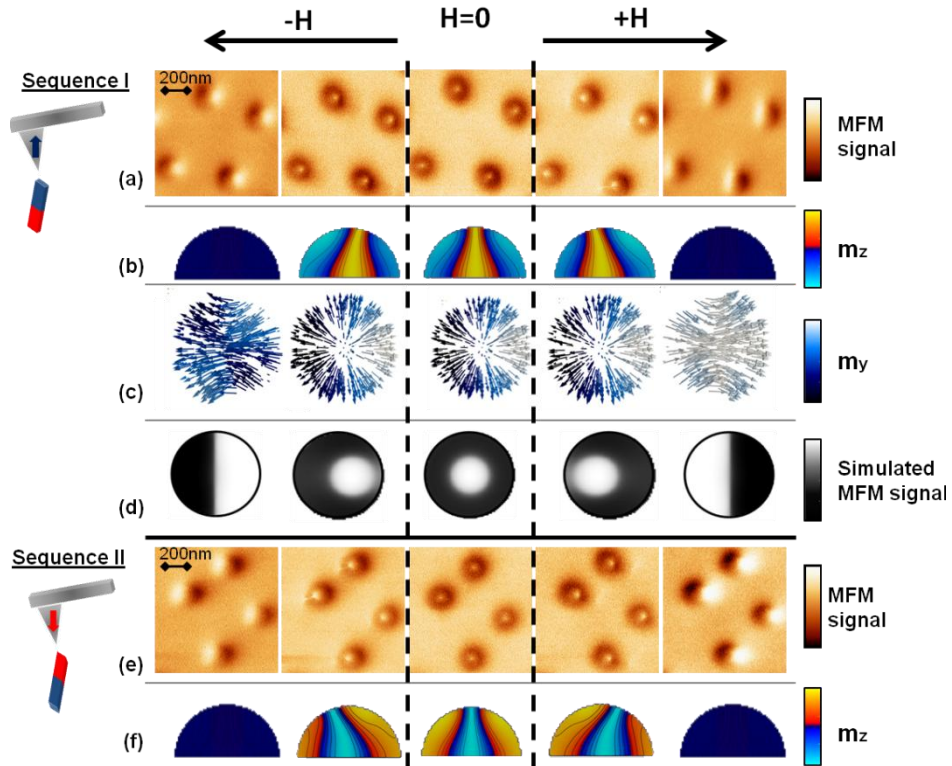
**Figure 5.6** (a) Core displacement under in plane applied field in Néel skyrmions and (d) in vortex configuration. The region marked in yellow expands because the spins are aligned with the applied field. Adapted from [ref29] (b) and (e) are images of hedgehog skyrmions and vortices under applied magnetic fields. (c) and (f) Corresponding profiles drawn on the upper nanodot shows the displacement of the core under in-situ applied fields.

Results show that in the sub-100 nm nanodots (Py1) the displacement of the core is either parallel or antiparallel to the in-plane magnetic field, which is indicative of the absence of IP closed-flux magnetization configuration. To evidence this displacement, profiles of the MFM data have been drawn in Figure 5.6c. This confirms the hypothesis that the dot magnetization configuration in Py1 is not a vortex, but rather a hedgehog skyrmion configuration with an essential radial IP magnetization component and a OOP magnetization component rotating from the core to the dot edges by means of radial curling of the spins.

For bigger radius particles (Py3) the demagnetization process changes dramatically. As shown in Figure 5.6e, when field is applied the cores move perpendicular to it, as it is indeed expected from vortices. The profiles from Figure 5.6f evidence the displacement of the core in the perpendicular direction.



Further measurements and modeling of sub-100 nm nanodots (Figure 5.7) give us a deeper insight into its magnetization reversal process.



**Figure 5.7** (a) and (e) show schematically the defined state of the tip polarity prior to sequence I and II respectively. MFM images of Py1 in (a) and (e) show the evolution of the core of the skyrmion moving antiparallel (parallel) to the external applied field. Simulated hedgehog skyrmions of positive and negative polarities (b) & (f) reproduce the movement of the core in sequence I and II. In (c) the transverse configuration of the hemisphere base displays a radial arrangement of the in plane magnetization in hedgehog skyrmion of positive polarity. A simulated MFM image from sequence I is presented in (d).

Considering a unit cylindrical magnetization vector  $\mathbf{m}$  ( $m_\rho$ ,  $m_\phi$ ,  $m_z$ ) with the  $z$  axis directed perpendicularly to the film surface, if an in-plane bias field is directed along  $O_y$  axis ( $H_y > 0$ ), such as in Figure 5.7a and d, the skyrmion core moves along the  $O_y$  axis. Thus, the Néel skyrmion core displacement  $Y$  fulfills the rule:  $\text{sign}(Y) = -\text{sign}(m_\rho)$  i.e., contrary to the vortex, in the hedgehog skyrmions the radial configuration and the core magnetization are not independent. The upwards or downwards direction of the core magnetization determines the radial direction, namely from inside-out or

from outside-in respectively. Thus, in the first case (Figure 5.7a) the structure moves antiparallel to the field, owing to the radial configuration pointing outwards. In sequence II (Figure 5.7e) the skyrmion core moves parallel to the field since the radial magnetization points inwards.

In a hemispherical dot ( $z > 0$ ) or a truncated hemisphere ( $z > z_c > 0$ ), the radial magnetization component and the skyrmion core polarity  $p = \text{sign}(m_z(0))$  are not independent. The core polarity sign determines the radial magnetization direction, namely from inside-out or from outside-in, respectively.

It is important to notice that the magnetic state of the tip has been defined prior to the measurements (Figures 5.7a and 5.7e). In sequence I ( $p > 0$ ) the core displaces antiparallel to the field, owing to the radial magnetization configuration pointing outwards (Figure 5.7c). In sequence II ( $p < 0$ ) the skyrmion core displaces parallel to the field as it is indeed observed in the experiment, since the radial magnetization points inwards.<sup>30</sup>

The magnetization direction of the tip makes the skyrmion move in one direction or the opposite, which evidences that the stray field of the tip plays a crucial role on the definition of the magnetic configuration of the nanodots. In fact, positive or negative core skyrmion can be induced by applying a perpendicular field in the appropriate sense. Therefore, the fact that an OOP local field determines the development of a positive or negative core skyrmion configuration explains why the images obtained in the MFM measurements (i.e., white core and dark contour) remain the same regardless of the magnetization direction of the tip.

Simulated MFM images shown in Figure 5.7d reproduce nicely the experimental data. As an approximation, permalloy hemispherical nanoparticles (Py1) were modelled via micromagnetic simulations with the Object Oriented Micromagnetic Simulation code.<sup>31</sup> The nanoparticles were discretized with a  $1 \times 1 \times 1 \text{ nm}^3$  mesh and the magnetic parameters used for permalloy were  $A = 11 \text{ pJ/m}$ ,  $\mu_0 M_s = 1 \text{ T}$  and zero uniaxial magnetic anisotropy. Initial conditions close to that of the Néel skyrmion were used as initial magnetic configuration, letting them evolve to the minimum energy state. Simulations in Figure 5.7b and Figure 5.7f prove that a hedgehog skyrmion configuration is, at least, metastable in hemispheres of 70 nm in

diameter. They demonstrate the stability of both positive (and negative) polarity hedgehog skyrmions, with the radial component of the magnetization pointing out (and in), in good agreement with the observations.

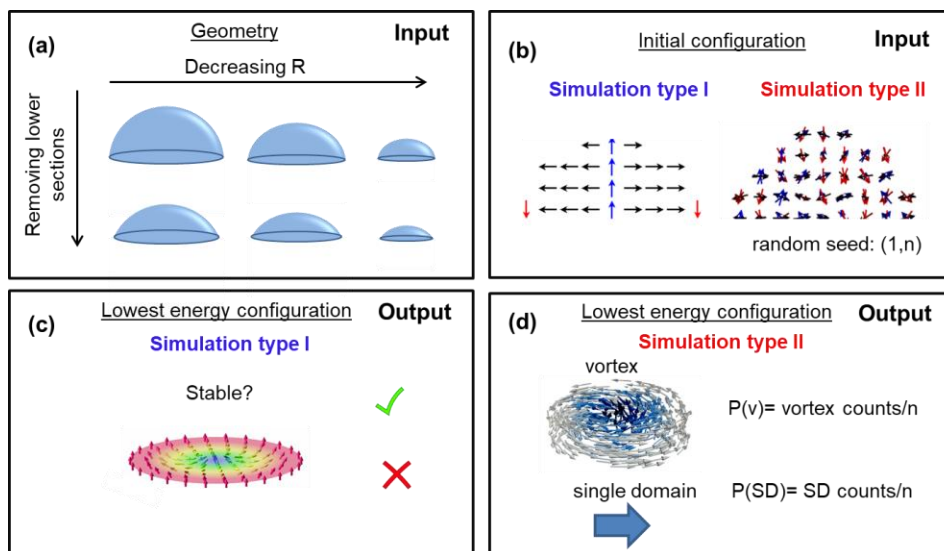
In micromagnetic simulations, with the Oxs\_MinDriver to impose the energy minimization criteria, the skyrmion was subjected to a field sequence to reproduce the experiments. If no additional conditions are determined, the skyrmion configuration happens to be highly metastable and it vanishes in presence of the smallest IP or OOP field perturbation. In this sense, a radial anisotropy was imposed to the outer shell of the nanodot to simulate the surface anisotropy and contribute to the stabilization of the configuration. As expected, the annihilation fields are very dependent on the chosen surface anisotropy value. A reasonable agreement between experiments and simulations was found when the anisotropy was set to  $2.5 \times 10^5 \text{ J/m}^3$ .

On another note, micromagnetic simulations unveil that the core diameter is wide at the base and it narrows approaching the nanodot surface. Additionally, when it is subjected to external field, the magnetic moments of the base respond later than the ones closer to the dot upper surface. Notice that the out-of-plane ( $m_z$ ) magnetization component is represented in a color scale and that a transversal dot cross-section is shown to emphasize the movement of the core. Images in Figure 5.6c display the base plane of the nanodot with radial configuration ( $m_y$  depicted in a blue color scale), which is present when the skyrmion has not yet been annihilated.

## 5. Phase diagram of skyrmions

The presence of a skyrmion in a system without DMI interaction sparks new questions about the stability of the Néel skyrmions. Additionally, the fact that they were detected in small nanodots (Py1) but not in bigger ones (Py3) lead us to the study of the geometrical boundaries for skyrmion stabilization. Micromagnetic simulations were conducted in hemispherical nanodots in absence of external fields. Their radius was varied between  $15 \text{ nm} < R < 70 \text{ nm}$ . For each radius value, the simulation was repeated removing lower circular sections to the hemisphere (schematically explained in Figure 5.8a), in order to study the behavior of flat nanodots. As explained in chapter 2, micromagnetic simulations solve the LLG equation with some initial

conditions. The simulation is deterministic for each set of initial conditions. The stabilization of a skyrmion in simulations was only possible when initial conditions close to those of a Néel skyrmion were chosen. Therefore, the first approach (simulation type I) is to impose initial magnetization close to a skyrmion to all the geometries and verify for which of them the skyrmion remains as a stable state using the energy minimization criteria (Figure 5.8c).

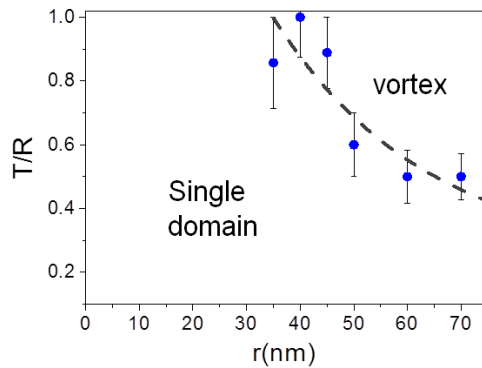


**Figure 5.8** Diagram of the procedure followed to plot a phase diagram. (a) Hemispheres of different radius and aspect ratio are chosen for each simulation. (b) Two types of simulations are conducted, which differ in the chosen initial magnetic configuration. (c) From simulation type I we determine whether the hedgehog skyrmion is stable for each geometry. (d) In simulation type II, we can conclude whether the geometrical parameter lead to vortex or single domain configuration, through statistical considerations.

This systematic study provides simulation points which can be plotted in a graph. A dashed line has been added to help the eye. The aspect ratio  $L/R$  is plotted versus the hemisphere radius  $R$ .

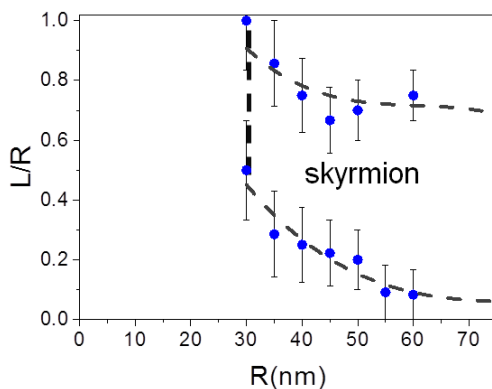
Three boundary curves have been obtained, as shown in Figure 5.9, delimiting the geometrical parameters in which skyrmions are energetically stable. No skyrmion was found in hemispheres of radius below 30nm. This might be a consequence of the dominating exchange anisotropy in the small diameter regime. The lower boundary arises owing to the decrease of the shape anisotropy, since the curvature and the confinement seem to play a

role in the stabilization of the skyrmion. The upper boundary conversely, can be a consequence of the minimization of the magnetostatic energy. As the diameter of the hemisphere increases, the necessary aspect ratio to stabilize the skyrmion presents a decreasing tendency.



**Figure 5.9** Plot of simulation data that delimits the area of the graph where skyrmions are stabilized.

A second systematic study (Simulation type II) was carried out varying the parameters of the hemisphere as in the previous study (Figure 5.8c). This time, a random initial configuration was imposed to each particular hemisphere with different  $R$  and  $L/R$ . This process was repeated several times for each case changing the random seed. After several simulations with different seeds the magnetic configuration with highest probability was selected. Since close to the boundary the probability to obtain each configuration tends to  $P=0.5$ , a probability beyond  $P \geq 0.6$  was considered enough to attribute a magnetic configuration to a specific geometry. As expected, only two types of magnetic textures were obtained: vortex and in-plane single domain. The data is plotted and a single curve was obtained, as in Figure 5.9, which delimits the two areas where each configuration is more likely to appear. This trend can be ascribed to a change in the regime; particularly in dots of small radius the exchange energy dominates, whereas in bigger dots vortices form to minimize the magnetostatic energy by avoiding charge formation.



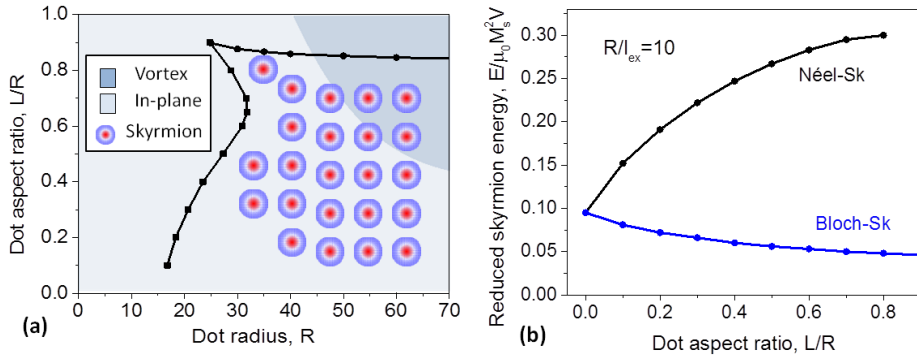
**Figure 5.10** Phase diagram showing the boundary curve between single domain and vortex configurations.

Analytical calculations, carried out to shed light on the experimental result, also predict the existence of a hedgehog skyrmion in Py nanoparticles with no perpendicular anisotropy or DMI (see Figure 5.11a). Yet, only vortices or single domain states have been reported so far in these soft magnetic structures in the literature.<sup>1</sup>

Calculations, entirely performed by Professor Kostyantyn Gusliyenko on circular nanodisks, show that Néel skyrmions indeed exist in permalloy dots as high-energy metastable states, *i.e.*, with higher energy than Bloch skyrmion (or vortex) states. In Figure 11b, the reduced skyrmion energy is plotted versus the dot aspect ratio, particularized for the case  $R/l_{ex}=10$ .  $l_{ex}=\sqrt{2A/\mu_0 M_s^2}$  is the material exchange length,  $A$  the exchange parameter and  $M_s$  accounts for the saturation magnetization.

Néel skyrmions exist in some regions in the phase diagram (regions delimited by the black dots and lines in Figure 5.11a) and become inaccessible for large dot thicknesses  $L$ , or small dot radius  $R$ , due to their very high energies. Owing to the increasing magnetostatic energy when the ratio  $L/R$  increases, the upper boundary in Figure 5.11a presents a downwards trend. On the other hand, the exchange energy increases with the dot radius  $R$  decreasing at fixed  $L/R$ , making the Néel skyrmion unstable at small  $R$  (left boundary in Figure 5.11a marked with black squares). Results obtained through micromagnetic simulations on hemispherical dots have been added to the graph in Figure 5.11a, showing relatively good agreement, in spite of the

lower boundary of Figure 5.11a, that has not been found through analytical calculations.

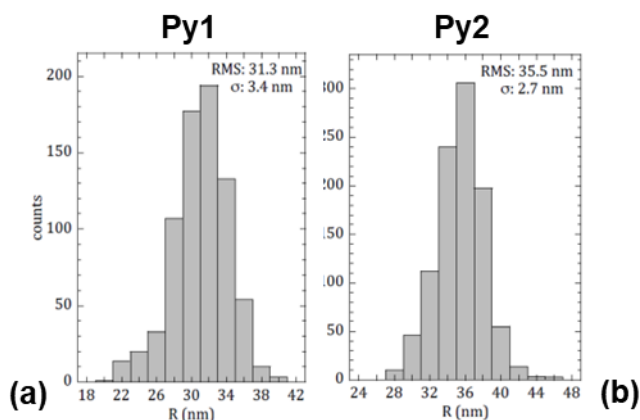


**Figure 5.11** (a) Phase diagram indicating the region where the skyrmion exists in a permalloy nanodot. The black boundaries have been analytically calculated in plane circular dots. The light blue and the grey regions denote the ground states corresponding to in-plane and vortex configurations, respectively. The red-blue dots mark the points where (meta) stable skyrmion configurations were found by micromagnetic simulations in hemispherical dots. (b) Energies of Néel and Bloch (vortex) skyrmions as a function of the dot aspect ratio calculated analytically.

### 5.1. Further investigation on the effect of the size

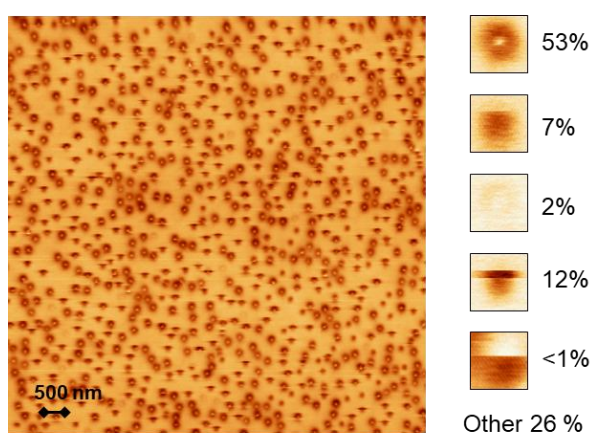
A sample with smaller nanodot diameter was fabricated (Py2) with the objective of conducting an experimental study on nanodots with diameters closer to the radius boundary predicted theoretically (Figure 5.11a). One should keep in mind that micromagnetic simulations results assert that magnetic skyrmions are not energetically favorable configurations in hemispheres of radius below 30nm.

Sample Py2 was therefore fabricated through HCL starting with smaller polystyrene spheres. Notice that the size distribution of sample Py2 ( $\sigma=3.4\text{nm}$ ) shown in Figure 5.12b is bigger than the distribution of sample Py1 ( $\sigma=2.7\text{nm}$ ). This fact can give us a wider range of magnetic configurations -compared to Sample Py1- as shown in Figure 5.13 corresponding to the MFM images performed with nanosensors commercial probes.



**Figure 5.12** Radius distribution histogram of (a) sample Py1 and (b) sample Py2.

We remind that in equivalent measurements (Figure 5.3c) a unique configuration (skyrmion) was present. In this case, skyrmions represent the vast majority of the configurations. The statistics shown in Figure 5.13 have been performed over a sample of 756 nanodots. 53% of skyrmions might seem a low rate, but we need to keep in mind that 26% name as “others” do also account for skyrmions which are not completely stable during the measurements. Together, skyrmions represent practically 80 % of the configurations. The rest of the configurations shown in Figure 5.13 are rather scarce, particularly the ones identified as single domain in-plane configurations, which constitute less than 1%.



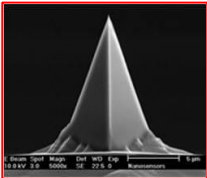
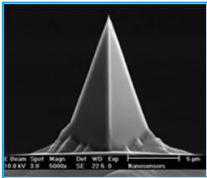
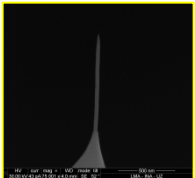
**Figure 5.13** MFM image of sample Py2 performed with a commercial Nanosensors (high moment) tip.



Interestingly, these single domain configurations, which due to the tip stray field display modifications during measurement<sup>35</sup> seem to be softer than skyrmions.

As we have previously concluded, the MFM tip plays a crucial role when it comes to, for example, define a positive or negative polarity skyrmion. For this reason, the stabilization of the skyrmion configuration via tip stray field is further investigated. Different types of MFM tips have been fabricated though sputtering (type 2) and FEBID (type 3) to achieve good control over the tips stray fields. In the first place, the non-commercial lowest interacting tip -obtained through FEBID- was utilized for MFM imaging. This type of tips, already introduced in Chapter 2, consist of a very narrow Fe nanorod with low stray field, very close to the sensitivity limit of the microscope.

In table 5.2, a summary of the non-conventional MFM probes used along these experiments is presented. The growth of Fe nanorods by Focused Electron Beam Induced Deposition (FEBID) on standard AFM tips allow obtaining diameters below 35nm and very sharp endings (7nm) to improve the resolution.

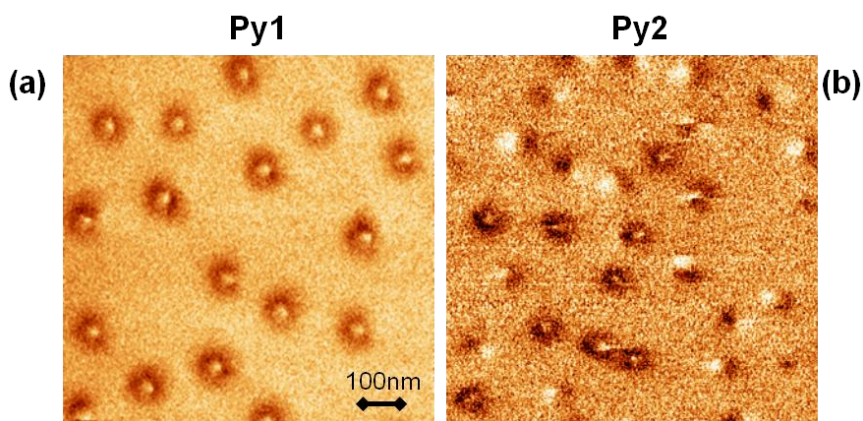
Tip category	1	2	3
SEM Image			
Type	Nanosensors commercial	Sputtering cobalt coated	Fe nanorod
Dimensions	50nm coating	From ~20 to 35nm coating	Diameter: from ~7 to 50nm Length: ~1000nm

**Table 5.2** Features of the tips utilized for the VF-MFM experiments summarized in Figure 18.

Moreover, the cylindrical geometry and the high aspect ratio of the Fe nanorods maximize the OOP vs IP ratio, and allow us to produce very low interacting probes to avoid alteration of domain structures in soft magnetic materials as explained in Chapter 2. All probes consisting of ferromagnetic

nanorods were grown by Javier Pablo-Navarro from the University of Zaragoza, as a result of an ongoing collaboration with the group of Prof. J.M. de Teresa from the ICMA-CSIC and Instituto de Nanociencia de Aragón.

Back to nanodots, new measurements were performed in samples Py1 and Py2 (Figure 5.14) with a tip which does not alter the magnetic configuration of the sample. Figure 5.14a shows 100% of skyrmion configurations rate when Py1 is imaged with low interacting tip. Further images were performed to enrich the statistic and no variation was found. This reinforces the theoretical statement that the Néel skyrmion is a possible configuration even in the absence of external stimuli, or in the best experimental conditions, under very low tip interaction. Magnetic image of Sample Py2 (see Figure 5.14b) presents nonetheless a different trend. Black-white dipolar contrasts are indicative of in-plane configurations. Notice that since the sample is demagnetized (similar to sample Py1), the dipoles show different orientations. After various images taken in different sample areas, we can claim that skyrmions constitute around 30% of the configurations, while 70% of single domain configurations are present.



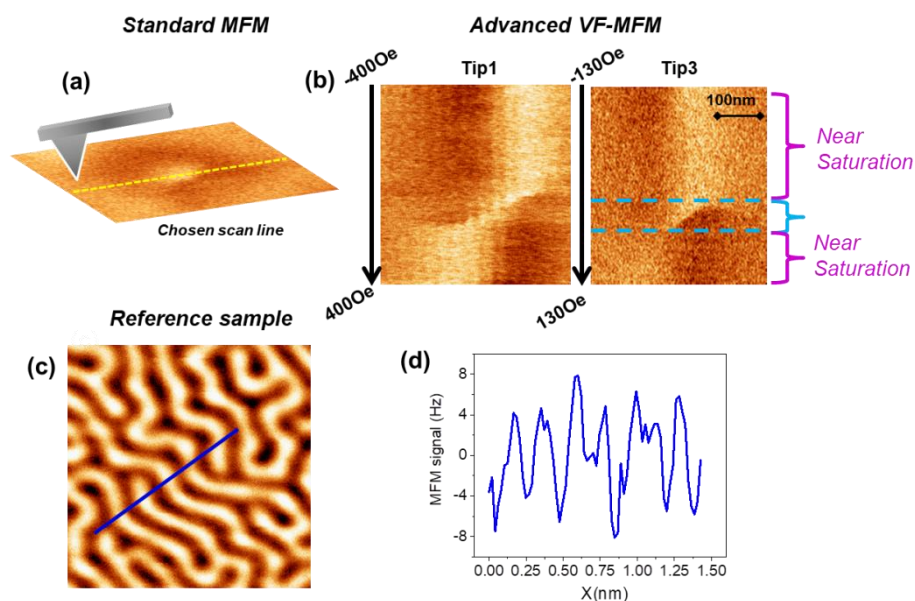
**Figure 5.14** (a) 100% Skyrmion configurations in Sample Py1 and (b) many magnetic dipoles present in Sample Py2. Both imaged were acquired with lowest interacting tip obtained.

Although this research line remains open for deeper experimental studies, we have successfully demonstrated that there is indeed a lower radius boundary for the stabilization of skyrmions.

In micromagnetic simulations, the skyrmion states are highly metastable and are destroyed by small in-plane fields. Experimentally, we have verified that they exist over larger interval of IP applied field values which points towards an additional stabilization by the field coming from the MFM tip.<sup>37</sup> Further experiments were carried out to assess the influence of the tip localized magnetic field on the skyrmion stability. With this purpose, several low moment MFM tips were designed for comparison (their specific features are gathered in Table 5.2). To obtain tips with intermediate stray fields, Co was sputtered on AFM tips choosing the desired thickness.

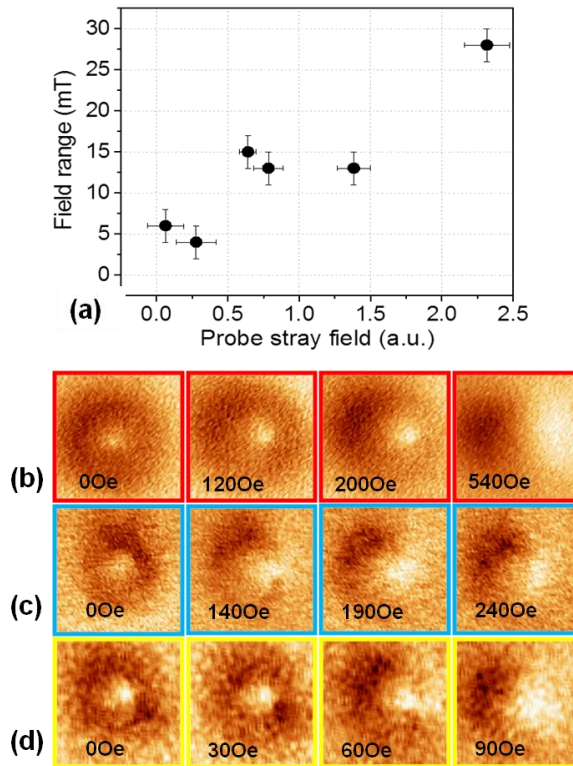
Making use of series of VF-MFM based methods, the critical fields of the skyrmions have been determined. In Figure 5.15a, the skyrmion existence field ranges —corresponding fields between nucleation and complete annihilation- are depicted as a function of the stray field of the probes. Prior to the performance of advanced VF-MFM modes (introduced in Chapter 2), a standard MFM image is obtained with the desired tip. This way, the skyrmion core of a particular nanodot can be located. Next, the scan is stopped in the slow direction, and the diameter of the dot is repeatedly scanned (see yellow line in Figure 5.15a). A field sweep is enabled in the corresponding range and the magnetic image is recorded. The resulting image (Figure 5.15b) allows discriminating areas where the nanodot is saturated (marked with a pink line in the left) and the area where the skyrmion exists (inside the blue square). This method also enables the visualization of the skyrmion core movement, from nucleation to annihilation. The error of the measurements, coming from various sources, is estimated to be 20 Oe.

To establish the relationship between the local field and the stabilization of the skyrmion is necessary to evaluate the tip stray field. It can be experimentally calibrated<sup>40</sup> through electron holography measurements and a subsequent complex data analysis. However, in this section a simple and practical method to determine the stray field of the tips is presented. A CoPt thin film with well-defined out-of-plane domains is imaged with each tip at their corresponding working distance (see an example in Figure 5.15c).



**Figure 5.15** (a) Standard MFM image of the nanodot Py1 to localize the skyrmion core. (b) Advanced VF-MFM measurement. The yellow line in (a) is repeatedly scanned, while the field is varied. The saturated areas at the top and bottom of the image have been marked with a pink line. In the central area the skyrmion exists (marked with a blue square). (c) Image of the reference sample with well-defined OOP domains of homogeneous stray field intensity. (d) Profile from (c) used to extract the maximum magnetic signal value obtainable for each tip.

Profiles of each image are plotted (as shown in Figure 5.15d) to extract the maximum MFM signal (frequency shift) for each tip. Even though a direct stray field value is not obtained, the comparison of signals from different tips is enough to evaluate the relative out-of-plane stray field components. Figures 5.16b-d display representative standard MFM of skyrmions under *in-situ* applied fields, performed with probes of different stray field values. Notice that the color code of the squares is in accordance with that shown in Table 5.2. Interestingly, the skyrmion annihilation field is almost 5 times larger when a commercial probe is used (tip 1, Figure 5.16b) in comparison with the values obtained for the thinnest nanorod probe (tip 3, Figure 5.16d). Thus, larger OOP stray fields lead to the stabilization of the skyrmion, turning it into a magnetically harder configuration. As in previous works where the local field of the tip is used to manipulate the magnetic charges,<sup>38,39</sup> in this work the tip stray field serves as a tool to control the stability of the skyrmion configuration.



**Figure 5.16** (a) Correlation between out-of-plane stray field and stability of the skyrmions. The circles represent the experimental data. The dashed lines help as a guide to the eye to remark the growing (decreasing) tendency. Field sequences performed with different tips, showing decreasing saturating fields from (b)-(d). Image size 250x250nm.

The critical fields show a clear dependence on the stray field arising from the MFM probe (Figure 5.16a).

The application of a local out-of-plane stray field, can act as a modulator to tune the stability of the skyrmion, confined in a soft nanodot. Generally speaking, the stabilization of hedgehog skyrmions in a material with neither DMI interaction nor magnetic anisotropy invites to lead efforts to span the range of magnetic systems where topologically non trivial spin textures can be found.

## 6. Conclusions

Permalloy nanodots of 140 nm diameter present vortex spin textures, with extra-large cores, as it was theoretically predicted. This configuration is expected in intermediate regions between OOP single domain configuration and vortex states, in the phase diagram of soft magnetic nanodiscs.

VF-MFM probes to be a reliable tool for the determination of vortex chiralities, based on the detection of the positive or negative perpendicular displacement direction of the vortex core.

Permalloy nanodots of sub-100 nm diameter can host topologically nontrivial spin textures. We detected for the first time hedgehog (Néel) skyrmions in soft magnetic Py nanoparticles. This is a non-expected magnetization configuration in the nanoparticles without DMI and more remarkably, in absence of any magnetic anisotropy.

The existence of Hedgehog skyrmions as possible states in Py hemispheres has been demonstrated through micromagnetic simulations and the conditions that the geometrical parameters need to fulfill to ensure their existence have been determined. A new magnetic configuration phase diagram including the skyrmion existence area has been plotted accordingly.

Skyrmions are further stabilized with local OOP magnetic stray fields. We have demonstrated that by utilizing tips with different stray fields, the critical values of the skyrmions change significantly.

Remarkably, for nanodots of 70 nm diameter, skyrmions are present in 100% of the images when they are detected with a very low interacting tip. Instead, for smaller nanodots (with bigger size dispersion), in-plane single domain magnetic configurations are detected, when a very thin MFM probe is utilized. This probes that the studied nanodots sizes lie very close to the boundary between different magnetic configurations.

The existence of the Néel skyrmions in nanodots without magnetic anisotropy and negligible DMI opens new perspectives for the exploration of

topologically non-trivial spin textures in magnetic systems that have not been yet considered.

The high saturation magnetization, low anisotropy and damping constant of the Py nanodots, together with well-defined magnetic resonance spectra, open a path to their applications in microwave devices based on the fast magnetization dynamics, otherwise hampered by the high damping constant of systems with DMI.

The following articles have been sent for publication in relation with the work presented in this chapter:

- (1) Goiriena-Goikoetxea, M; Gusliencko, K.; Rouco, M.; Orue, I.; Berganza, E.; Jaafar, M.; Asenjo, A.; Fernandez-Gubieda, M.L.; Fernández Barquín, L.; García-Arribas, A. Magnetization reversal in circular vortex dots of small radius. *Nanoscale* **9**, (2017).
- (2) Berganza, E.; Jaafar, M.; Goiriena-Goikoetxea, M.; Pablo-Navarro, J.; García-Arribas A.; Gusliencko, K.; Magén, C.; de Teresa, J.M.; Chubykalo-Fesenko, O.; Asenjo, A. Hedgehog skyrmion observation in sub-100nm permalloy nanodots. *Nat.Comm.* (under review)



## 7. References

1. Goiriena-Goikoetxea, M. *et al.* Magnetization reversal in circular vortex dots of small radius. *Nanoscale* (2017). doi:10.1039/C7NR02389H
2. Tartaj, P., Del Puerto Morales, M., Veintemillas-Verdaguer, S., González-Carreño, T. & Serna, C. J. The preparation of magnetic nanoparticles for applications in biomedicine. *J. Phys. D. Appl. Phys.* **36**, R182–R197 ST–The preparation of magnetic nanopa (2003).
3. Weizenecker, J., Gleich, B., Rahmer, J., Dahnke, H. & Borgert, J. Three-dimensional real-time in vivo magnetic particle imaging. *Phys. Med. Biol.* **54**, (2009).
4. Pankhurst, Q. A., Thanh, N. K. T., Jones, S. K. & Dobson, J. Progress in applications of magnetic nanoparticles in biomedicine. *J. Phys. D. Appl. Phys.* **42**, (2009).
5. Yu, M. K. *et al.* Drug-loaded superparamagnetic iron oxide nanoparticles for combined cancer imaging and therapy in vivo. *Angew. Chemie - Int. Ed.* **47**, 5362–5365 (2008).
6. Mahmoudi, M., Sant, S., Wang, B., Laurent, S. & Sen, T. Superparamagnetic iron oxide nanoparticles (SPIONs): Development, surface modification and applications in chemotherapy. *Advanced Drug Delivery Reviews* **63**, 24–46 (2011).
7. Thompson, D. A. & Best, J. S. The future of magnetic data storage technology. *IBM J. Res. Dev.* **44**, 311–322 (2000).
8. Wachowiak, a *et al.* Direct observation of internal spin structure of magnetic vortex cores. *Science* **298**, 577–80 (2002).
9. Pinilla-Cienfuegos, E., Mañas-Valero, S., Forment-Aliaga, A. & Coronado, E. Switching the Magnetic Vortex Core in a Single Nanoparticle. *ACS Nano* **10**, 1764–1770 (2016).
10. Moya, C., Iglesias-Freire, Ó., Batlle, X., Labarta, A. & Asenjo, A. Superparamagnetic versus blocked states in aggregates of Fe<sub>3-x</sub>O<sub>4</sub> nanoparticles studied by MFM. *Nanoscale* **7**, 17764–17770 (2015).
11. Guo, F., Belova, L. M. & McMichael, R. D. Spectroscopy and imaging of edge modes in permalloy nanodisks. *Phys. Rev. Lett.* **110**, (2013).
12. TARTAJ, P., Morales, M. del P. M., Veintemillas-Verdaguer, S., González-Carreño, T. & Serna, C. J. Progress in the preparation of magnetic nanoparticles for applications in biomedicine. *J. Phys. D. Appl. Phys.* **42**, 224002 (2009).
13. Laurent, S. *et al.* Magnetic iron oxide nanoparticles: Synthesis, stabilization, vectorization, physicochemical characterizations and biological applications. *Chem. Rev.* **108**, 2064–2110 (2008).
14. Huh, Y.-M. *et al.* Hybrid nanoparticles for magnetic resonance imaging of target-specific viral gene delivery. *Adv. Mater.* **19**, 3109–3112 (2007).
15. Kruijs, F. E., Fissan, H. & Peled, A. Synthesis of nanoparticles in the gas phase for

- electronic, optical and magnetic applications—a review. *J. Aerosol Sci.* **29**, 511–535 (1998).
16. Vitol, E. a, Novosad, V. & Rozhkova, E. a. Microfabricated magnetic structures for future medicine: from sensors to cell actuators. *Nanomedicine (Lond)*. **7**, 1611–24 (2012).
  17. Sousa, C. T. *et al.* Nanoporous alumina as templates for multifunctional applications. *Applied Physics Reviews* **1**, (2014).
  18. Gawronski, P., Merazzo, K. J., Chubykalo-Fesenko, O., Del Real, R. P. & Vázquez, M. Micromagnetism of permalloy antidot arrays prepared from alumina templates. *Nanotechnology* **25**, (2014).
  19. Colson, P., Henrist, C. & Cloots, R. Nanosphere lithography: A powerful method for the controlled manufacturing of nanomaterials. *Journal of Nanomaterials* **2013**, (2013).
  20. Goiriena-Goikoetxea, M., García-Arribas, A., Rouco, M., Svalov, A. V. & Barandiaran, J. M. High-yield fabrication of 60 nm Permalloy nanodiscs in well-defined magnetic vortex state for biomedical applications. *Nanotechnology* **27**, (2016).
  21. Cowburn, R. P., Koltsov, D. K., Adeyeye, A. O., Welland, M. E. & Tricker, D. M. Single-domain circular nanomagnets. *Phys. Rev. Lett.* **83**, 1042–1045 (1999).
  22. Guslienko, K. Y. & Novosad, V. Vortex state stability in soft magnetic cylindrical nanodots. *J. Appl. Phys.* **96**, 4451–4455 (2004).
  23. K. Yu. Guslienko. Magnetic Vortex State Stability, Reversal and Dynamics in Restricted Geometries. *J. Nanosci. Nanotechnol.* **8**, 2745–2760 (2008).
  24. Shinjo, T., Okuno, T., Hassdorf, R., Shigeto, K. & Ono, T. Magnetic vortex core observation in circular dots of permalloy. *Science (80-. )*. **289**, 930–932 (2000).
  25. Wong, J., Greene, P., Dumas, R. K. & Liu, K. Probing magnetic configurations in Co/Cu multilayered nanowires. *Appl. Phys. Lett.* **94**, (2009).
  26. Choe, S. B. *et al.* Vortex Core-Driven Magnetization Dynamics. *Science (80-. )*. **304**, 420–422 (2004).
  27. Jaafar, M. *et al.* Variable-field magnetic force microscopy. *Ultramicroscopy* **109**, 693–699 (2009).
  28. Pollard, S. D. *et al.* Observation of stable Néel skyrmions in cobalt/palladium multilayers with Lorentz transmission electron microscopy. *Nat. Commun.* **8**, (2017).
  29. Kezsmarki, I. *et al.* Neel-type skyrmion lattice with confined orientation in the polar magnetic semiconductor GaV4S8. *Nat. Mater.* **14**, 1116–1122 (2015).
  30. Siracusano, G. *et al.* Magnetic Radial Vortex Stabilization and Efficient Manipulation Driven by the Dzyaloshinskii-Moriya Interaction and Spin-Transfer Torque. *Phys. Rev. Lett.* **117**, (2016).

31. Donahue, M. J. & Porter, D. G. *OOMMF User's Guide, Version 1.0 Interagency Report NISTIR 6376. October* (2002).
32. Metlov, K. L. Equilibrium large vortex state in ferromagnetic disks. *J. Appl. Phys.* **113**, (2013).
33. Jaafar, M. *et al.* Control of the chirality and polarity of magnetic vortices in triangular nanodots. *Phys. Rev. B - Condens. Matter Mater. Phys.* **81**, (2010).
34. Schneider, M., Hoffmann, H. & Zweck, J. Lorentz microscopy of circular ferromagnetic permalloy nanodisks. *Appl. Phys. Lett.* **77**, 2909–2911 (2000).
35. Precner, M., Fedor, J., Šoltýs, J. & Cambel, V. Dual-tip magnetic force microscopy with suppressed influence on magnetically soft samples. *Nanotechnology* **26**, (2015).
36. Iglesias-Freire, Ó., Jaafar, M., Berganza, E. & Asenjo, A. Customized MFM probes with high lateral resolution. *Beilstein J. Nanotechnol.* **7**, 1068–1074 (2016).
37. Wang, C., Xiao, D., Chen, X., Zhou, Y. & Liu, Y. Manipulating and trapping skyrmions by magnetic field gradients. *New J. Phys.* **19**, (2017).
38. Gartside, J. C., Burn, D. M., Cohen, L. F. & Branford, W. R. A novel method for the injection and manipulation of magnetic charge states in nanostructures. *Sci. Rep.* **6**, (2016).
39. Wang, Y. L. *et al.* Rewritable artificial magnetic charge ice. *Science (80-. )*. **352**, 962–966 (2016).
40. Panchal, V. *et al.* Calibration of multi-layered probes with low/high magnetic moments. *Sci. Rep.* **7**, (2017).



## General conclusions

The main conclusions derived from this thesis are:

I- The tip constitutes the central element of the Magnetic Force Microscopy technique. The right choice of the cantilever mechanical properties and the functionalization of the tip with different magnetic elements have been explored to solve different problematics. In particular, the development of MFM probes to measure specimens of biological interest in liquid media has been achieved. The use of sputtering coated low force constant levers is conclusive for the improvement of the signal to noise ratio.

II- Different mechanisms to control the domain wall pinning in uniaxially magnetized cylindrical nanowires have been investigated. Geometrical modifications and the introduction of layers of non-magnetic materials change the energy landscape and create pinning sites. The inclusion of copper segments, separating iron-cobalt layers growing in length produces a ratched-like effect that yields step-by-step unidirectional magnetization reversal.

III-  $\text{Co}_x\text{Ni}_{1-x}$  based homogeneous and multilayer nanowires have been studied. The versatility of the magnetic anisotropy of the Co-based alloys make them attractive to obtain tailored magnetic properties and configurations. Using magnetic force microscopy, we were able to unveil the different non-standard domain structures that arise as a consequence of small compositional variations in the alloy.

IV- Based on the acquired experience in the nanowire characterization using magnetic force microscopy, a protocol has been developed to make it easier to align all nanowires, localize them and prevent their attachment to the tip. Furthermore, a second procedure has been reported to grow electrical contacts to the nanowire in standard laboratories without nanolithography facilities.

V- The study of the magnetization reversal mechanism of soft sub-100nm nanodots, together with some anomalous features in remanent MFM images –all cores pointing in the same direction in the demagnetized

state and the intense dark contour-, led to the conclusion that the nanodots present hedgehog skyrmion configurations. This conclusion has major implications, since the system does not possess Dzyaloshinski-Moriya interaction (DMI) nor perpendicular anisotropy (PMA), considered so far necessary ingredients to host skyrmions.

## Conclusiones generales

Las conclusiones principales de esta tesis son:

I- La sonda es el elemento central del microscopio. Se ha estudiado (i) la elección de palancas con distintas propiedades magnéticas y (ii) la funcionalización de la punta de AFM mediante la incorporación de distintos elementos magnéticos. Cabe resaltar el desarrollo de puntas de MFM para medidas de muestras de interés biológico en medio líquido. El uso de sondas con palancas de bajo momento, -recubiertas mediante sputtering- ha sido clave para la mejora de la relación señal-ruido en este tipo de medidas.

II- Se han investigado distintos mecanismos para el control de puntos de anclaje de paredes de dominio en nanohilos con imanación uniáxica. La introducción de cambios en la geometría de los hilos, así como la intercalación de segmentos no magnéticos, produce cambios en balance de energías, dando lugar a la creación de puntos de anclaje. La introducción de los segmentos de cobre para separar segmentos de hierro-cobalto de longitud creciente genera un efecto de “trinquete” que conduce a una propagación unidireccional y escalonada de la pared de dominio.

III- Se han estudiado individualmente nanohilos basados en la aleación  $\text{Co}_x\text{Ni}_{1-x}$ , además de nanohilos multisegmentados basados en este material. La versatilidad de esta aleación permite el diseño de las propiedades y configuraciones magnéticas de los nanohilos a la carta. Empleando la microscopía de fuerzas, hemos interpretado estructuras de dominios no estándares que aparecen como consecuencia de variaciones composicionales en la aleación o a lo largo del nanohilo.

IV- En base a la experiencia adquirida durante la caracterización de nanohilos utilizando el microscopio de fuerzas magnéticas, se ha desarrollado un protocolo de preparación de los nanohilos sobre los sustratos para garantizar su alineamiento, facilitar su localización y prevenir su adhesión a las puntas de MFM. Además, se ha descrito un segundo protocolo sencillo, para el crecimiento de contactos eléctricos para los nanohilos en laboratorios sin instalaciones de nanolitografía, para futuros estudios de magnetotransporte.

V- El estudio del mecanismo de inversión de la imanación en nanodiscos magnéticamente blandos de diámetro inferior a 100nm, junto con características anómalas detectadas en imágenes de MFM – todos los núcleos apuntando en la misma dirección en el estado desimanado o la alta intensidad del contraste del contorno- llevan a la conclusión de que los discos presentan configuración de tipo skyrmion. Este resultado tiene implicaciones relevantes, dado que estamos frente a un sistema que no presenta interacción Dzyaloshinski-Moriya (DMI) ni anisotropía perpendicular, consideradas hasta el momento ingredientes necesarios para albergar skyrmions en nanoestructuras.



## List of Publications

Along this thesis 10 manuscripts have been send for publication to peer-reviewed international journals:

Iglesias-Freire, Ó; Bran, C.; Berganza, E.; Mínguez Bacho, I.; Magén, C.; Vázquez, M. ; Asenjo, A. Spin configuration in isolated FeCoCu nanowires modulated in diameter. *Nanotechnology* **26**, (2015).

Bran, C.; Berganza, E.; Palmero, E.M.; Fernández-Roldán, J.A.; P. del Real, R.; Aballe, L.; Foerster, M.; Asenjo, A.; Vázquez, M. Spin configuration of cylindrical bamboo-like magnetic nanowires. *J. Mater. Chem. C* **4**, 978–984 (2016).

Berganza, E.; Bran, C.; Jaafar, M.; Vazquez, M.; Asenjo, A. Domain wall pinning in FeCoCu bamboo-like nanowires. *Sci. Rep.* **6**, (2016).

Iglesias-Freire, Ó.; Jaafar, M.; Berganza, E.; Asenjo, A. Customized MFM probes with high lateral resolution. *Beilstein J. Nanotechnol.* **7**, 1068–1074 (2016).

Rodríguez, L. A.; Bran, C.; Reyes, D.; Berganza, E.; Vázquez, M.; Gatel, C.; Snoeck, E.; Asenjo, A. Quantitative Nanoscale Magnetic Study of Isolated Diameter-Modulated FeCoCu Nanowires. *ACS Nano* **10**, 9669–9678 (2016).

Berganza, E.; Jaafar, M.; Bran, C.; Fernández-Roldán, J.A.; Chubykalo-Fesenko, O.; Vázquez, M.; Asenjo, A. Multisegmented Nanowires: A Step towards the Control of the Domain Wall Configuration. *Sci. Rep.* **7**, (2017).

Bran, C. Fernández-Roldán, J.A.; Palmero, E.M.; Berganza, E.; Guzman, J.; P. del Real, R.; Asenjo, A.; Fraile-Rodríguez, A.; Foerster, M.; Aballe, L.; Chubykalo-Fesenko, O.; Vázquez, M. Direct observation of transverse and vortex metastable magnetic domains in cylindrical nanowires. *Phys. Rev. B* **96**, (2017).

Goiriena-Goikoetxea, M; Guslienko, K.; Rouco, M.; Orue, I.; Berganza, E.; Jaafar, M.; Asenjo, A.; Fernandez-Gubieda, M.L.; Fernández Barquín, L.; García-Arribas, A. Magnetization reversal in circular vortex dots of small radius. *Nanoscale* **9**, (2017).

Berganza, E.; Jaafar, M.; Goiriena-Goikoetxea, M.; Pablo-Navarro, J.; García-Arribas A.; Gusliencko, K.; Magén, C.; de Teresa, J.M.; Chubykalo-Fesenko, O.; Asenjo, A. Hedgehog skyrmion observation in sub-100nm permalloy nanodots. *Submitted*.

Bran, C.; Berganza, E.; Fernandez-Roldan, J.A.; Palmero, E.; Meier, J.; Calle, E.; Jaafar, M.; Forster, M.; Aballe, L.; Fraile Rodriguez, A.; P. del Real, R.; Asenjo, A.; Chubykalo-Fesenko O.; Vazquez, M.  
A ratchet-like effect in magnetic cylindrical nanowires. *Submitted*.